THE VISCOELASTIC EFFECTS ON THE EVOLUTION OF A THREE-DIMENSIONAL MICROBUBBLE

by

EOIN N. O'BRIEN

A thesis submitted to

The University of Birmingham

for the degree of

DOCTOR OF PHILOSOPHY

School of Mathematics

College of Engineering and Physical Sciences

The University of Birmingham

July 2023

UNIVERSITY OF
BIRMINGHAM

University of Birmingham Research Archive

e-theses repository

This unpublished thesis/dissertation is copyright of the author and/or third parties. The intellectual property rights of the author or third parties in respect of this work are as defined by The Copyright Designs and Patents Act 1988 or as modified by any successor legislation.

Any use made of information contained in this thesis/dissertation must be in accordance with that legislation and must be properly acknowledged. Further distribution or reproduction in any format is prohibited without the permission of the copyright holder.

Abstract

Bubbles often appear in non-Newtonian liquids from nature, engineering, to biomedical applications, but their study has been under researched compared to their Newtonian counterpart. Here we extend the axisymmetric modelling of Lind and Phillips (Lind and Phillips [2010a,b, 2013]) to three-dimensional modelling. The approach is based on the boundary integral method coupled with Maxwell's constitutive equation and Jeffrey's constitutive equation. The flow is assumed to have moderate to high Reynolds number and thus is irrotational in the bulk domain. The viscoelastic effects are incorporated approximately in the normal stress balance at the bubble surface. The numerical model has excellent agreement with the corresponding Rayleigh-Plesset equation for spherical bubbles in a non-Newtonian liquid. Computations are carried out for a bubble near a corner at various angles. The numerical results agree very well with the experiments for bubbles in a Newtonian fluid in a corner. For a Maxwell fluid/Jeffrey fluid, as the Deborah number, De, increases/viscosity ratio, β decreases, the amplitude and period of the bubble oscillation increase, the bubble migration to the corner enhances, and the bubble jet is broader, flatter and inclined more to the further boundary. This implies an improvement to surface cleaning of all surrounding boundaries for ultrasonic cavitation cleaning and results in greater administration of noninvasive therapy and drug delivery.

ACKNOWLEDGEMENTS

I would like to express my sincerest gratitude to my supervisors, Dr Qianxi Wang and Dr Warren R. Smith, for their support and guidance over the course of my PhD, and for the wisdom and knowledge they have bestowed upon me.

I would also like to thank Prof. Tim Phillips from Cardiff University for his unrivalled expertise in non-Newtonian bubble mechanics and for his guidance, support and suggestions on my research on three-dimensional bubble mechanics.

I would like to express a deep appreciation to my colleagues on the University of Birmingham bubble team, Dr Mehdi Mahmud, Dr Callan Corbett, and You Yu, for their commitment and contribution to my research, and to all my fellow researchers in the department who inspire me to become a better mathematician.

Finally, I would like to dedicate this thesis to my mother and father, my family, and my friends for their unconditional love and support in everything I do, without whom, none of this would be possible.

LIST OF PUBLICATIONS

E N O'Brien, M H Mahmud, W R Smith, Q Wang, T N Phillips, 2023. The evolution of a three-dimensional microbubble at a corner in a Maxwell fluid. *Physics of Fluids*, 35(10)

Mathematics knows no races or geographic boundaries; for mathematics, the cultural world is one country.
- David Hilbert

CONTENTS

1 Introduction **1**

1.1 Application background 2

1.2 Research review 4

1.2.1 Newtonian fluids 5

1.2.2 Non-Newtonian fluids 9

1.3 Thesis overview 12

2 Mathematical & Physical Model **15**

2.1 Potential flow model 15

2.1.1 Green's second identity 15

2.1.2 Kinematic and dynamic boundary conditions 19

2.2 Spherical bubble theory for validation 21

2.2.1 Rayleigh-Plesset equation 21

2.2.2 Potential calculation 22

2.3 Nondimensionalisation 24

2.4 Initial conditions 25

2.5 Viscoelastic modelling 27

2.5.1 Newtonian model 27

2.5.2 Maxwell's model 29

2.5.3 Jeffrey's model 31

3 Numerical Model **34**

3.1 Interpolation of the surface 35
3.2 Normal vector, mean curvature, tangential velocity, and bubble centroid calculations 39
3.3 Lagrangian integration with time 43
3.4 Calculation of Kelvin impulse 44
3.4.1 Kelvin impulse near a flat rigid boundary 46
3.4.2 Kelvin impulse near a corner 48
3.5 Calculation of bubble volume and bubble centroid 49
3.6 Elastic mesh technique 51

4 Numerical Simulations Of The Maxwell Model 55

4.1 Infinite fluid 56
4.1.1 Validation of radius history with Rayleigh-Plesset equation . . 56
4.1.2 Validation of potential calculation with spherical bubble theory 57
4.1.3 Convergence test 59
4.1.4 Results for an infinite fluid 60
4.2 Bubble near a flat rigid boundary 62
4.2.1 Results on radius history, bubble migration, Kelvin impulse and jet shape 62
4.2.2 Increased stand-off distance 65
4.2.3 Effect of stand-off distance 68
4.3 Bubble near a rigid corner 68
4.3.1 Comparison with experimental data 69
4.3.2 Evolution of a bubble near a corner in a Maxwell fluid 70
4.3.3 Bubble near a right-angled corner 73
4.3.4 Results on jet shape and angle at collapse 76
4.3.5 Decreased corner angle 76
4.3.6 Effects of domain size on the bubble in a Maxwell fluid 80
4.3.7 Convergence with Deborah number 81

4.3.8 Convergence with Reynolds number 82
4.4 Conclusion 84

5 Numerical Simulations Of The Jeffrey Model 87

5.1 Infinite fluid 88
5.1.1 Radius history validation with Rayleigh-Plesset equation . . . 88
5.1.2 Results for an infinite fluid 89
5.2 Bubble near a flat rigid boundary 91
5.2.1 Results on radius history, bubble migration, Kelvin impulse and jet shape 92
5.2.2 Increased stand-off distance 94
5.2.3 Effect of stand-off distance 97
5.3 Bubble near a rigid corner 97
5.3.1 Evolution of a bubble near a corner in a Jeffrey fluid 98
5.3.2 Agreement with previous cases 98
5.3.3 Results on jet shape and angle at collapse 102
5.3.4 Increased corner angle 103
5.3.5 Effects on domain size of a bubble in a Jeffrey fluid 107
5.3.6 Convergence with Deborah number 108
5.3.7 Convergence with Reynolds number 110
5.4 Conclusion 111

6 Conclusion and Discussion 113

6.1 Summary 113
6.2 Conclusions 114
6.3 Future work 116
6.3.1 Upper-convected Maxwell model 116
6.3.2 Oldroyd-B model 118
6.3.3 Surfactants and shear stress 119

A Bubble in a Maxwell Fluid **132**

A.1 Bubble in a Maxwell fluid 132

B Bubble in a Jeffrey Fluid **136**

B.1 Bubble in a infinite Jeffrey fluid 136

C MATLAB code for non-Newtonian Rayleigh-Plesset Equation **139**

LIST OF FIGURES

1.1 A turbine highlighting the significant erosion caused by the continuous formation of cavitation clouds, bubble jetting and shock wave creation (Fomitchev-Zamilov [2012]). 3

1.2 An image of the original bubble experiment conducted by T. B. Benjamin first discovering the non-spherical behaviour of a bubble near a rigid boundary (Benjamin and Ellis [1966]). 6

1.3 The evolution of a spherical experimental bubble in a 0.5% polyacrylamide viscoelastic fluid with the resulting pressure shock wave being separately measured (Brujan [2019]). 12

3.1 A schematic representation of increasing mesh levels to approximate the surface of a bubble, with the top left representing a level 3 mesh, and the bottom right representing a level 20 mesh. As shown, the increased mesh level better approximates the surface of a sphere but it more computationally demanding. 35

3.2 A schematic depicting the unit normal and its surrounding nodes at a given node point (Mahmud [2017]). The normal at a node can be approximated using the surrounding normals of the mesh elements. . 39

3.3 A schematic representation of the method of images for a bubble near a rigid boundary. The wall is simulated by introducing a image bubble symmetrically below the wall. 46

3.4 A schematic representation of the method of images for a bubble at a corner of angle $\alpha = \pi/2$. Four different image bubbles are introduced to simulate the interaction with the two rigid boundaries. In doing so, the BIM must be solved four times at each time-step. 47

3.5 A schematic representation of the tetrahedrons created from an internal point in the bubble, $\boldsymbol{r_0}$, and three surface nodes, $i-1$, i, and $i+1$. By creating a tetrahedron from every mesh element, the total volume of the bubble can then be approximated. 49

3.6 A two-dimensional representation of how the addition of triangle $0, k, k+1$ and the subtraction of triangle $0, i, i+1$ gives an approximation of the area $i, i+1, k, k+1$. A similar idea is applied to three dimensions. 51

4.1 The comparison of the radius history of a spherical bubble in a Maxwell fluid with $De = 2.0$, between the non-Newtonian Rayleigh-Plesset equation (2.3.6) and the BIM code. The parameters of the bubble and the surrounding liquid are $\zeta = 1.667$, $\sigma = 0.073 Nm^{-1}$, $P_0 = 101.3 kPa$, $P_v = 0.023 P_0$ and $\rho = 999 kgm^{-3}$. 56

4.2 The comparison of ϕ_{nn} for a spherical bubble in a Maxwell fluid with $De = 2.0$, between spherical bubble theory (2.2.17) and the BIM code with the remaining parameters being the same as in Figure 4.1. . . . 57

4.3 The jet profiles and location of a bubble initiated with 5412 nodes and 5724 nodes for angles, $\alpha = \pi/2$ and $\pi/4$ with the remaining parameters being the same as in Figure 4.1. 58

4.4 The influence of the Deborah number on the radius history a bubble in an infinite Maxwell fluid with $De = 0.0$, 0.2, 2.0, and 20.0. The remaining parameters of the fluid are the same as in Figure 4.1. . . . 58

4.5 The influence of the Deborah number, De, on the average velocity of a bubble in an infinite Maxwell fluid. The parameters of the surrounding liquid are the same as in Figure 4.1. 59

4.6 The influence of the Deborah number, De, on the radius history of a bubble near a wall with stand-off distance, $\gamma = 1.0$ in a Maxwell fluid. The parameters of the surrounding liquid are the same as in Figure 4.1. 60

4.7 The influence of the Deborah number, De, on the Kelvin impulse of a bubble near a wall with stand-off distance $\gamma = 1.0$ in a Maxwell fluid. The parameters of the surrounding liquid are the same as in Figure 4.1. 62

4.8 The influence of the Deborah number, De, on the jet shape of a bubble near a wall with stand-off distance $\gamma = 1.0$ in a Maxwell fluid. The parameters of the surrounding liquid are the same as in Figure 4.1. 63

4.9 The influence of the Deborah number, De, on the migration of a bubble near a wall in a Maxwell fluid. The stand-off distance is given by $\gamma = 1.0$ and the location of the wall would correspond to the line $\xi_N = -1.0$. The parameters of the surrounding liquid are the same as in Figure 4.1. 64

4.10 The influence of the Deborah number, De, on the radius history of a bubble near a wall with stand-off distance $\gamma = 1.25$ in a Maxwell fluid. The parameters of the surrounding liquid are the same as in Figure 4.1. 64

4.11 The influence of the Deborah number, De, on the Kelvin impulse of a bubble near a wall with stand-off distance $\gamma = 1.25$ in a Maxwell fluid. The parameters of the surrounding liquid are the same as in Figure 4.1. 65

4.12 The influence of the Deborah number, De, on the jet shape of a bubble near a wall with stand-off distance $\gamma = 1.25$ in a Maxwell fluid. The parameters of the surrounding liquid are the same as in Figure 4.1. . 66

4.13 The influence of De on the migration of a bubble near a wall in a Maxwell fluid. The stand-off distance is given by $\gamma = 1.25$ and the location of the wall would correspond to the line $\xi_N = -1.25$. The parameters of the surrounding liquid are the same as Figure 4.1. . . . 67

4.14 The influence of stand-off distance on the radius of a bubble near a flat rigid boundary in a Maxwell fluid. The remaining parameters are the same as for Figure 4.1. 68

4.15 Comparison for the evolution of a bubble in a corner of angle, $\alpha = \pi/2$ between the BIM code and experimental data in a Newtonian fluid, with parameters $R_m^* = 0.85mm$, $\gamma_F = 2.17$, $\gamma_N = 1.08$, $\varepsilon = 100$, and $\kappa = 1.4$, where $Re = 8.4 \times 10^3$, $We = 8.7 \times 10^{-3}$, and $\delta = 0.009$. . . . 69

4.16 Comparison for the evolution of a bubble in a corner of angle, $\alpha = \pi/4$ between the BIM code and experimental data in a Newtonian fluid, with parameters $R_m^* = 13.5mm$, $\gamma_N = 1.03$, $\gamma_F = 1.03$, $\varepsilon = 100$, and $\kappa = 1.4$, where $Re = 1.3 \times 10^5$, $We = 1886$, and $\delta = 0.036$. 71

4.17 The evolution of a three-dimensional bubble near a right-angled corner in a Maxwell fluid of Deborah number $De = 2.0$ with stand-off distances, $\gamma_N = 1.0$ and $\gamma_F = 1.5$ towards the near and far wall, respectively. All remaining parameters are the same as in Figure 4.1. 71

4.18 The evolution of a three-dimensional bubble near a corner of angle $\alpha = \pi/4$ in a Maxwell fluid of Deborah number $De = 2.0$ with stand-off distances, $\gamma_N = 1.0$ and $\gamma_F = 1.5$ towards the near and far wall, respectively. All remaining parameters are the same as in Figure 4.1. 71

4.19 The influence of the Deborah number, De, on the radius history of a bubble near a corner of angle $\alpha = \pi/2$ with stand-off distances $\gamma_N = 1.0$ and $\gamma_F = 1.5$ in a Maxwell fluid. The parameters of the surrounding liquid are the same as in Figure 4.1. 72

4.20 The influence of the Deborah number, De, on the Kelvin impulse towards the near wall of a bubble near a corner of angle, $\alpha = \pi/2$ in a Maxwell fluid. The parameters of the surrounding fluid are the same as in Figure 4.1. 72

4.21 The influence of the Deborah number, De, on the Kelvin impulse towards the far wall of a bubble near a corner of angle, $\alpha = \pi/2$ in a Maxwell fluid. The parameters of the surrounding fluid are the same as in Figure 4.1. 73

4.22 The influence of the Deborah number, De, on the migration towards the near wall of a bubble near a corner of angle $\alpha = \pi/2$ in a Maxwell fluid. The stand-off distance is given by $\gamma_N = 1.0$ and the location of the wall would correspond to the line $\xi_N = -1.0$. The parameters of the surrounding liquid are the same as in Figure 4.1. 74

4.23 The influence of the Deborah number, De, on the migration towards the far wall of a bubble near a corner of angle, $\alpha = \pi/2$ in a Maxwell fluid. The stand-off distance is given by $\gamma_F = 1.5$ and the location of the wall would correspond to the line $\xi_F = -1.5$. The parameters of the surrounding liquid are the same as in Figure 4.1. 75

4.24 The influence of the Deborah number, De, on the jet profile of a bubble initiated in a corner of angle, $\alpha = \pi/2$. The remaining parameters are the same as in Figure 4.1. 76

4.25 The influence of the Deborah number, De, on the radius history of a bubble near a corner of angle, $\alpha = \pi/4$ with stand-off distances $\gamma_N = 1.0$ and $\gamma_F = 1.5$ in a Maxwell fluid. The parameters of the surrounding liquid are the same as in Figure 4.1. 77

4.26 The influence of the Deborah number, De, on the Kelvin impulse towards the near wall of a bubble near a corner of angle, $\alpha = \pi/4$ in a Maxwell fluid. The parameters of the surrounding fluid are the same as in Figure 4.1. 77

4.27 The influence of the Deborah number, De, on the Kelvin impulse towards the far wall of a bubble near a corner of angle, $\alpha = \pi/4$ in a Maxwell fluid. The parameters of the surrounding fluid are the same as in Figure 4.1. 78

4.28 The influence of the Deborah number, De, on the migration towards the near wall of a bubble near a corner of angle, $\alpha = \pi/4$ in a Maxwell fluid. The stand-off distance is given by $\gamma_N = 1.0$ and the location of the wall would correspond to the line $\xi_N = -1.0$.The parameters of the surrounding liquid are the same as in Figure 4.1. 79

4.29 The influence of the Deborah number, De, on the migration towards the far wall of a bubble near a corner of angle, $\alpha = \pi/4$ in a Maxwell fluid. The stand-off distance is given by $\gamma_F = 1.5$ and the location of the wall would correspond to the line $\xi_F = -1.5$. The parameters of the surrounding liquid are the same as in Figure 4.1. 79

4.30 The influence of the Deborah number, De, on the jet profile of a bubble initiated in a corner of angle, $\alpha = \pi/4$. The remaining parameters are the same as in Figure 4.1. 80

4.31 The influence of the domain size on the radius history of a bubble in a corner of various angles, α. The remaining parameters of the fluid are the same as in Figure 4.1. 81

4.32 The large scale influence of the Deborah number on the jet profile of a bubble initiated in a corner of angle, $\alpha = \pi/2$. The remaining parameters are the same as in Figure 4.1. 82

4.33 The large scale influence of the Deborah number, De, on the radius history of a bubble initiated in a corner of angle, $\alpha = \pi/2$. The remaining parameters are the same as in Figure 4.1. 83

4.34 The influence of the Deborah number, De, on the jet profile of a bubble in a corner of angle, $\alpha = \pi/2$ with $Re = 450$. The remaining parameters are the same as in Figure 4.1. 83

4.35 The influence of the Deborah number, De, on the radius of a bubble in a corner of angle, $\alpha = \pi/2$ with $Re = 450$. The remaining parameters are the same as in Figure 4.1. 84

5.1 The comparison of the radius history of a spherical bubble in a Jeffrey fluid with $\beta = 0.4$, between the non-Newtonian Rayleigh-Plesset equation (2.3.6) and the BIM code. The parameters of the surrounding liquid are the same as in Figure 4.1. 88

5.2 The influence of the viscosity ratio, β, on the radius history of a spherical bubble in an infinite Jeffrey fluid over the first oscillation. The parameters of the surrounding liquid are $\zeta = 1.667$, $\delta = 0$, $\sigma = 0.073 Nm^{-1}$, $P_0 = 101.3 kPa$, $P_v = 0.023 P_0$ and $\rho = 999 kgm^{-3}$. . . 89

5.3 The influence of the viscosity ratio, β, on the maximum velocity of a spherical bubble in an infinite Jeffrey fluid over the first oscillation. The remaining parameters are the same as in Figure 5.2. 90

5.4 The influence of the viscosity ratio, β, on the radius history of a bubble near a wall with stand-off distance $\gamma = 1.0$ in a Jeffrey fluid. The parameters of the surrounding liquid are the same as in Figure 5.2. 91

5.5 The influence of the viscosity ratio, β, on the Kelvin impulse of a bubble near a wall with stand-off distance $\gamma = 1.0$ in a Jeffrey fluid. The parameters of the surrounding liquid are the same as in Figure 5.2. 91

5.6 The influence of the viscosity ratio, β, on the migration of a bubble near a wall in a Jeffrey fluid. The stand-off distance is given by $\gamma_N = 1.0$ and the location of the wall would correspond to the line $\xi_N = -1.0$. The parameters of the surrounding liquid are the same as in Figure 5.2. 92

5.7 The influence of the viscosity ratio, β, on the jet shape of a bubble near a wall with stand-off distance $\gamma = 1.0$ in a Jeffrey fluid. The parameters of the surrounding liquid are the same as in Figure 5.2. . 93

5.8 The influence of the viscosity ratio, β, on the radius history of a bubble near a wall with stand-off distance $\gamma = 1.25$ in a Jeffrey fluid. The parameters of the surrounding liquid are the same as in Figure 5.2. 94

5.9 The influence of the viscosity ratio, β, on the Kelvin impulse of a bubble near a wall with stand-off distance $\gamma = 1.25$ in a Jeffrey fluid. The parameters of the surrounding liquid are the same as in Figure 5.2. 94

5.10 The influence of the viscosity ratio, β, on the migration of a bubble near a wall with in a Jeffrey fluid. The stand-off distance is given by $\gamma_N = 1.25$ and the location of the wall would correspond to the line $\xi_N = -1.25$. The parameters of the surrounding liquid are the same as in Figure 5.2. 95

5.11 The influence of the viscosity ratio, β, on the jet shape of a bubble near a wall with stand-off distance $\gamma = 1.25$ in a Jeffrey fluid. The parameters of the surrounding liquid are the same as in Figure 5.2. . 96

5.12 The influence of stand-off distance on the radius of a bubble near a flat rigid boundary in a Jeffrey fluid. The remaining parameters are the same as for Figure 5.2. 97
5.13 The evolution of a three-dimensional bubble near a corner of angle $\alpha = \pi/4$ in a Jeffrey fluid with viscosity ratio $\beta = 0.4$. The remaining parameters are the same as in Figure 5.2. 98
5.14 The influence of the viscosity ratio, β, on the radius history of a bubble near a corner with stand-off distances $\gamma_N = 1.0$ and $\gamma_F = 1.5$ in a Jeffrey fluid. The parameters of the surrounding liquid are the same as in Figure 5.2. 99
5.15 The influence of the viscosity ratio, β, on the Kelvin impulse towards the near wall of a bubble near a corner of angle, $\alpha = \pi/4$, with stand-off distances $\gamma_N = 1.0$ and $\gamma_F = 1.5$ in a Jeffrey fluid. The parameters of the surrounding liquid are the same as in Figure 5.2. 99
5.16 The influence of the viscosity ratio, β, on the Kelvin impulse towards the far wall of a bubble near a corner of angle, $\alpha = \pi/4$, with stand-off distances $\gamma_N = 1.0$ and $\gamma_F = 1.5$ in a Jeffrey fluid. The parameters of the surrounding liquid are the same as in Figure 5.2. 100
5.17 The influence of the viscosity ratio, β, on the migration towards the near wall of a bubble near a corner of angle, $\alpha = \pi/4$ in a Jeffrey fluid. The stand-off distance is given by $\gamma_N = 1.0$ and the location of the wall would correspond to the line $\xi_F = -1.0$. The parameters of the surrounding liquid are the same as in Figure 5.2. 101
5.18 The influence of the viscosity ratio, β, on the migration towards the far wall of a bubble near a corner of angle, $\alpha = \pi/4$ in a Jeffrey fluid. The stand-off distance is given by $\gamma_F = 1.5$ and the location of the wall would correspond to the line $\xi_F = -1.5$. The parameters of the surrounding liquid are the same as in Figure 5.2. 101

5.19 The influence of the viscosity ratio, β, on the jet shape of a bubble near a corner of angle, $\alpha = \pi/4$ with stand-off distances $\gamma_N = 1.0$ and $\gamma_F = 1.5$ in a Jeffrey fluid. The parameters of the surrounding liquid are the same as in Figure 5.2. 102

5.20 The influence of the viscosity ratio, β, on the radius history of a bubble near a corner of angle, $\alpha = \pi/2$ with stand-off distances $\gamma_N = 1.0$ and $\gamma_F = 1.5$ in a Jeffrey fluid. The parameters of the surrounding liquid are the same as in Figure 5.2. 103

5.21 The influence of the viscosity ratio, β, on the Kelvin impulse towards the near wall of a bubble near a corner of angle, $\alpha = \pi/2$ with stand-off distances $\gamma_N = 1.0$ and $\gamma_F = 1.5$ in a Jeffrey fluid. The parameters of the surrounding liquid are the same as in Figure 5.2. 104

5.22 The influence of the viscosity ratio, β, on the Kelvin impulse towards the far of a bubble near a corner of angle, $\alpha = \pi/2$ with stand-off distances $\gamma_N = 1.0$ and $\gamma_F = 1.5$ in a Jeffrey fluid. The parameters of the surrounding liquid are the same as in Figure 5.2. 104

5.23 The influence of the viscosity ratio, β, on the migration towards the near wall of a bubble near a corner of angle, $\alpha = \pi/2$, in a Jeffrey fluid. The stand-off distance is given by $\gamma_N = 1.0$ and the location of the wall would correspond to the line $\xi_N = -1.0$. The parameters of the surrounding liquid are the same as in Figure 5.2. 105

5.24 The influence of the viscosity ratio, β, on the migration towards the far wall of a bubble near a corner of angle, $\alpha = \pi/2$, in a Jeffrey fluid. The stand-off distance is given by $\gamma_F = 1.5$ and the location of the wall would correspond to the line $\xi_F = -1.5$. The parameters of the surrounding liquid are the same as in Figure 5.2. 105

5.25 The influence of the viscosity ratio, β, on the jet shape of a bubble near a corner of angle, $\alpha = \pi/2$ in a Jeffrey fluid. The parameters of the surrounding liquid are the same as in Figure 5.2. 106

5.26 The influence of the domain size on the radius history of a bubble in a corner of various angles, α. The remaining parameters of the fluid are the same as in Figure 5.2. 107

5.27 The large scale influence of the Deborah number on the jet profile of a bubble initiated in a Jeffrey fluid near a corner of angle $\alpha = \pi/4$. The remaining parameters are the same as in Figure 5.2. 108

5.28 The large scale influence of the Deborah number on the radius of a bubble initiated in a Jeffrey fluid near a corner of angle $\alpha = \pi/4$. The remaining parameters are the same as in Figure 5.2. 109

5.29 The large scale influence of the Reynolds number on the jet profile of a bubble initiated in a Jeffrey fluid near a corner of angle $\alpha = \pi/4$ with $Re = 450$ and initial radius, $R^* = 4.5 \times 10^{-5} m$. The remaining parameters are the same as in Figure 5.2. 109

5.30 The large scale influence of the Reynolds number on the radius of a bubble initiated in a Jeffrey fluid near a corner of angle $\alpha = \pi/4$ with $Re = 450$ and initial radius, $R^* = 4.5 \times 10^{-5} m$. The remaining parameters are the same as in Figure 5.2. 110

A.1 The comparison of ϕ_{nn} for a spherical bubble in a Maxwell fluid with $De = 0.0$, between spherical bubble theory (2.2.17) and the BIM code with the remaining parameters being the same as in Figure 4.1. . . . 132

A.2 The comparison of ϕ_{nn} for spherical bubble in a Maxwell fluid with $De = 0.2$, between a spherical bubble theory (2.2.17) and the BIM code with the remaining parameters being the same as in Figure 4.1. 133

A.3 The comparison of ϕ_{nn} for a spherical bubble in a Maxwell fluid with $De = 20.0$, between spherical bubble theory (2.2.17) and the BIM code with the remaining parameters being the same as in Figure 4.1. 133

A.4 The comparison of the radius history of a spherical bubble in a Maxwell fluid with $De = 0.0$, between the non-Newtonian Rayleigh-Plesset equation (2.3.6) and the BIM code with the remaining parameters being the same as in Figure 4.1. 134

A.5 The comparison of the radius history of a spherical bubble in a Maxwell fluid with $De = 0.2$, between the non-Newtonian Rayleigh-Plesset equation (2.3.6) and the BIM code with the remaining parameters being the same as in Figure 4.1. 134

A.6 The comparison of the radius history of a spherical bubble in a Maxwell fluid with $De = 20.0$, between the non-Newtonian Rayleigh-Plesset equation (2.3.6) and the BIM code with the remaining parameters being the same as in Figure 4.1. 135

B.1 The comparison of the radius history of a spherical bubble in a Jeffrey fluid with $\beta = 0.2$, between the non-Newtonian Rayleigh-Plesset equation (2.3.6) and the BIM code. The parameters of the surrounding liquid are the same as Figure 5.1. 136

B.2 The comparison of the radius history of a spherical bubble in a Jeffrey fluid with $\beta = 0.6$, between the non-Newtonian Rayleigh-Plesset equation (2.3.6) and the BIM code. The parameters of the surrounding liquid are the same as Figure 5.1. 137

B.3 The comparison of the radius history of a spherical bubble in a Jeffrey fluid with $\beta = 0.2$, between the non-Newtonian Rayleigh-Plesset equation (2.3.6) and the BIM code. The parameters of the surrounding liquid are the same as Figure 5.1. 137

LIST OF SYMBOLS

S_B	Bubble surface	Ω	Fluid domain
S_R	Rigid boundary surfaces	$\boldsymbol{u}$	Velocity vector
ϕ	Velocity potential	$\partial\phi/\partial n$	Normal velocity
$\boldsymbol{n}$	Normal vector	$\partial\Omega$	Calculation domain
V	Bubble volume	c	Solid angle
σ	Surface tension	P_B	Internal pressure
P_L	Liquid Pressure	P_0	Far-field pressure
T_{nn}	Deviatoric stress	g	Gravity
ρ	Density	γ	Stand-off distance
$\boldsymbol{I}$	Kelvin Impulse	R	Radius
α	Corner angle	t	Time
N	Number of mesh vertices	M	Number of mesh elements
κ	Curvature	$\boldsymbol{u}_T$	Tangential velocity
Δt	Varied time-step	$\Delta\phi$	Time-step coefficient
ζ	Ratio of specific heats	C	Viscous correction
We	Weber number	Re	Reynolds number
ϵ	Pressure difference	δ	Buoyancy
λ_1	Relaxation time	De	Deborah number
μ_s	Solvent viscosity	μ_p	Polymeric viscosity
μ	Total viscosity	β	Viscosity ratio

CHAPTER 1

INTRODUCTION

One of the observations of the phenomenon of cavitation is the creation of vapour and gas bubbles in low pressure fluid fields. Cavitation has been readily observed for over a century when excessive erosion to ship propellers were noticed (Rayleigh [1917]). The continuous rotation of the propeller results in constant pressure changes and cavitation formation, with the constant pressure changes in turn resulting in jet formation and shock waves. Figure 1.1 shows the damage that can be caused to a turbine due to the surrounding cavitation cloud.

When the pressure in a fluid substantially decreases, cavities start developing and expanding until an equilibrium is reached between the internal and external pressures of the cavitation bubble and surrounding fluid. Expansion inertia continues the expansion of the bubble until the pressure inside the bubble is lower than the surrounding fluid and collapse begins. The sudden collapse of the bubble causes jet formation, shock waves, and high amounts of pressure which damages all surrounding boundaries. The shock waves produced at collapse of the cavitation bubbles slowly erode the blades of the ships turbines. The jet formation and consequential impact also contributes to the ongoing erosion (Philipp and Lauterborn [1998]).

It is readily established that the creation of a cavitation cloud is one of the leading causes of damage to pumps, turbines, and propellers on ships (Buckland et al. [2013], Reisman et al. [1998]). Once eroded, the efficiency of the turbine or

propeller is drastically reduced. Hence, understanding the mechanisms for cavitation formation, jetting, and shock wave production are of paramount importance.

The violent collapse of bubbles has also been shown to be responsible for increased damage following an underwater explosions (Holt [1977], Klaseboer et al. [2005]). The rapid pulsations of underwater bubbles can displace large amounts of water and produce secondary shock waves which impact all surrounding boundaries. Hence, understanding the evolution of these bubbles is of paramount importance in preventing the erosion and reduced inefficiency of water turbines, or optimising damage in such a way that is beneficial. As we will see later, this is most important when considering ultrasonic cleaning.

1.1 Application background

Bubble mechanics has direct applications in a wide variety of areas. The destructive power of cavitation on many industrial machinery such as pumps, turbines, and propellers means that great focus is placed on bubbles near rigid boundaries with analysis focusing on the pressure and jetting (Blake and Gibson [1987], Lauterborn and Kurz [2010]). In these studies, the phenomenon of Bjerknes attraction was discovered, showing that the inclusion of a rigid boundary near the bubble results in non-spherical behaviour and jetting. Jetting greatly increases the surface velocity of the bubble and in turn results in higher levels of pressure in the fluid domain (Wang et al. [2020]).

However, under certain conditions, the collapse of cavitation bubbles can be very beneficial to the surrounding boundaries. One such application is ultrasonic cleaning. Ultrasonic cleaning is known to be one of the most effective tools for the cleaning of electrical and medical machinery on a microscopic scale, where the pressure and shock wave created by the collapsing bubble cleans the surrounding surfaces (Song et al. [2004a], Ohl et al. [2006a], Lauterborn and Kurz [2010]). This



Figure 1.1: A turbine highlighting the significant erosion caused by the continuous formation of cavitation clouds, bubble jetting and shock wave creation (Fomitchev-Zamilov [2012]).

is particularly effective for complex geometries which are difficult to navigate and for delicate machinery which can not be classically cleaned with a brittle tool, This technique is becoming a very beneficial procedure in dentistry for such reasons (Bulat [1974], Song et al. [2004b]). If the cavitation is controlled precisely, the bubble can undergo shape mode oscillations and large bubble migration. The shock waves emitted by these oscillation shape modes, the subsequent migration of the bubble, and jetting have been shown to efficiently remove contamination from surrounding boundaries (Chahine et al. [2016]). One such tool for controlling the evolution and migration of a cavitation bubble, is the subjection of a high energy acoustic wave.

With the inclusion of an acoustic wave, cavitation bubbles become applicable to a wider range of medical applications. One such application is known as extracorporeal shock wave lithotripsy (Fong et al. [2008]), for the treatment of kidney stones (Pishchalnikov et al. [2003]). Here, cavitation bubbles absorb a significant amount of energy from the incoming acoustic wave resulting in violent oscillations, collapse, jetting. The subsequent shock waves which are produced then aid in destroying the surfaces of the kidney stones. Coated microbubbles are also used for nondestructive

medical imaging (van der Meer et al. [2007]), where bubble clouds are injected into the bloodstream and can travel to all bodily organs due to their small radius. The scattering of ultrasonic waves on the surrounding blood and tissues and the contrast between the two has generated interest in this method for medical imaging. However, medical procedures using cavitation bubbles and ultrasonic waves still have certain obstacles. Such complications include bubble-bubble and bubble-wall interactions causing vascular injuries such as kidney edemas, haemorrhages, and haematomas (Lugli and Zerbetto [2007], Sreedhar et al. [2017]). Therefore, analysing the effect of such interactions requires much care and attention.

One application at the forefront of modern day bubble dynamics is noninvasive therapy and drug delivery (Coussios and Roy [2008]). Microbubbles containing the desired drug are placed inside the body and allowed to travel to the targeted area (Carson et al. [2011], Kaul [2004], Kooiman et al. [2009]). The violent collapse of the bubble due to ultrasound releases the contained drug and causes perforation of the surrounding cell membranes, which is known as sonoporation (Ohl et al. [2006b,a]). The non-Newtonian properties of the fluid are important due to the rheological properties of the blood and other bodily fluids (Brujan et al. [2008], Chmiel and Walitza [1980]). For example, blood is made up of cells of plasma where the total plasma volume is roughly 55% of the total blood volume. However, this method still faces many problems, for example the heating of localised tissue (Kennedy [2005], Leslie and Kennedy [2007], ter Haar and Coussios [2007]), and the influence of polymer additives on cavitation and tissue damage (Roberts et al. [2006]) is not yet fully understood.

1.2 Research review

To effectively implement microbubbles, it is important to fully understand the interaction between a bubble and the surrounding rigid boundaries in various Newtonian

and non-Newtonian fluids. Historically, the majority of research has been conducted on the computationally easier Newtonian fluids which we will discuss first.

1.2.1 Newtonian fluids

An important parameter to analyse the rheological properties of a fluid is it's viscosity, μ. The viscosity of a fluid relates the local stress in a moving fluid to the rate of deformation, and can be physically represented by the 'thickness' of a fluid. When a fluid is strained, it's rate of deformation is inversely proportional to viscosity. A fluid is said to be ***Newtonian*** if the viscosity of the fluid does not change with the rate of deformation, that is, there is a linear relationship between the shear rate and the shear stress. When the deviatoric stress is identically zero, the fluid is said to be inviscid. Classically, the shear rate of a fluid is determined by placing the fluid between two horizontal parallel plates with the bottom plate being stationary and the top plate being moved horizontally at some constant speed, U. Assuming a no-slip boundary condition, the shear stress acting parallel to the plates results in a decrease in the velocity of the fluid closer to the bottom plate. The velocity profile of the fluid then provides a description of the rate of shear. The most common Newtonian fluids are water and air, the former being the fluid for which the majority of bubble mechanics have been studied.

As previously mentioned, one of the first theoretical studies of cavitation was performed by Lord Rayleigh to discover the reasoning behind propeller damage on ships (Rayleigh [1917]). The research considered a spherical bubble in an infinite body of fluid in the absence of surface tension and viscosity. Rayleigh concluded that the collapse of cavitation bubbles leads to high levels of pressure which results in significant surface damage and was the underlying principle behind propeller erosion. However, the bubbles were thought to remain spherical, and the concept of jetting was not discovered for quite some time. The non-spherical properties of cavitation were not truly considered for another 50 years when experimental research

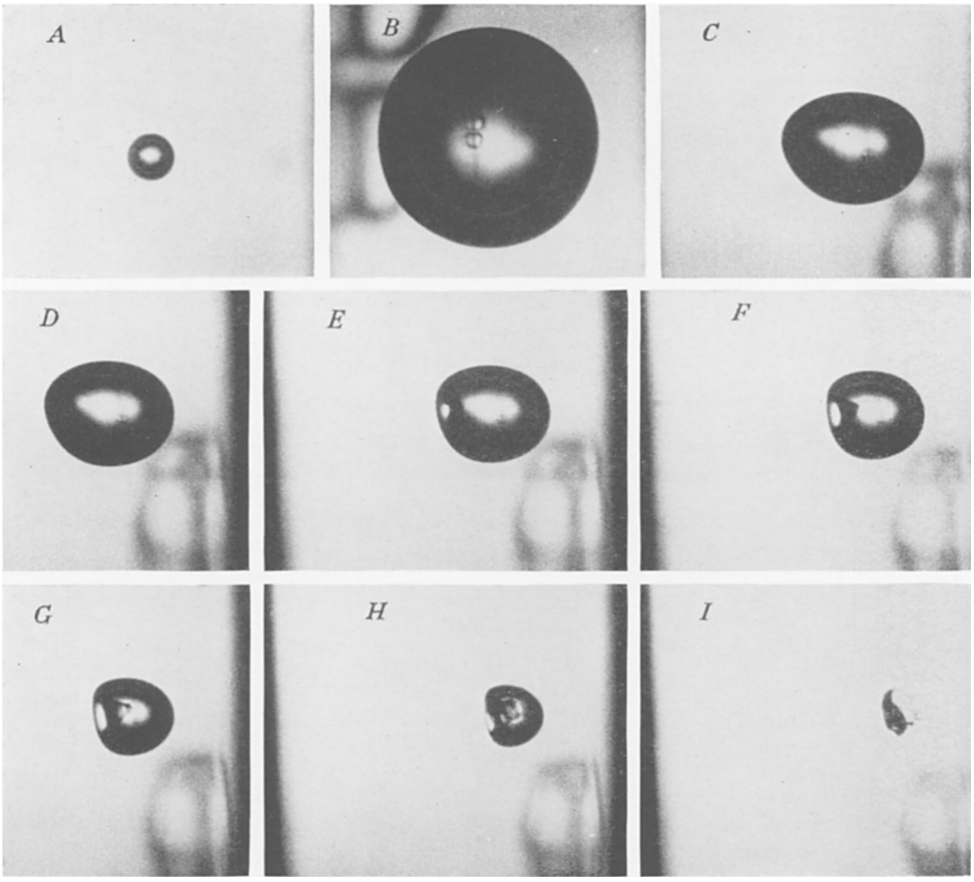


Figure 1.2: An image of the original bubble experiment conducted by T. B. Benjamin first discovering the non-spherical behaviour of a bubble near a rigid boundary (Benjamin and Ellis [1966]).

was conducted on the formation of jets near a solid boundary and the subsequent change to a toroidal bubble (Benjamin and Ellis [1966]). Images of this original bubble experiment can be found in Figure 1.2. This phenomenon has since been widely experimentally studied with numerous numerical techniques being developed to simulate the non-spherical evolution of a cavitation bubble.

Cavitation experiments provide wide insight into the non-spherical behaviours of cavitation bubbles in different geometric situations. Since T. B. Benjamin, many such experiments have been conducted. For example, the work on experimental bubbles near a rigid wall was extended to provide quantitative confirmation of numerical studies, with emphasis on measuring jet velocities and introducing the concept of laser induced cavitation (Lauterborn and Bolle [1975]) and further expanded to anal-

yse the pressure contours and velocity vectors in the surrounding fluid (Brujan et al. [2002]). More sophisticated experiments have been developed to show the evolution of a bubble in more complex geometries, such as a free surface (Zhang et al. [2013]), near a corner (Brujan et al. [2018]), or rising in a tube (Wu and Gharib [2002]). Many techniques have been developed to experimentally implement these various types of bubbles, such as TNT charges being used to generate underwater explosion bubbles (Hung and Hwangfu [2010]). Cavitation bubbles have been generated using sparks (Ohl et al. [2015]), or high intensity focused laser beam (Brujan et al. [2018], Lindau and Lauterborn [2003]). With the improvement of cavitation experiments, the development of numerical methods to simulate bubble evolution also improved.

Numerous three-dimensional, computational models have been developed to evaluate the evolution of a cavitation bubble in a Newtonian fluid, situated in different geometries, such as near a rigid inclined wall (Wang [1998]). As with the experimental investigations, the numerical simulations shown the jetting formation due to the surrounding boundary. Furthermore, buoyancy plays a key role on the evolution of the bubble with bubble migration being particularly influenced. When the bubble rises due to buoyancy, cusps can form on the bottom of the bubble due to Bjerknes force and the uplift on the rest of the bubble from the fluid. However, buoyancy becomes dominant for large Reynolds number flows, where the Reynolds number is a measure of inertia forces compared to viscous forces. So for such simulations, the viscous and viscoelastic effects are negligible. As such, there is no damping effects or energy dissipation throughout the fluid. Furthermore, the influence of surface tension also become negligible as the corresponding Weber number for the bubble, a dimensionless measure of the important of inertia compared to surface tension, is high. Throughout this current work, we assume the buoyancy effects are negligible so that the viscous and viscoelastic effects dominate.

Computational simulations have also been conducted for a bubble near a free surface (Supponen et al. [2015], Li et al. [2012a]), or in a narrow gap (Gonzalez-

Avila et al. [2020]). Such boundaries result in jetting of the bubble surface and the creation of a toroidal bubble (Liu et al. [2016]), a phenomenon also created as a result of a bubble being subjected to an acoustic wave (Wang and Manmi [2014], Manmi and Wang [2017]). The inclusion of acoustic waves results in jetting without the need for a rigid boundary. The intensity of the jetting and the jet velocities depends on the frequency and the pressure amplitude of the acoustic wave with a maximum energy transfer occurring at natural resonance (Wang [2017]). In these simulations, the bubble is of microscopic size meaning the viscous effects become dominant and the energy absorbed from the acoustic wave is dissipated throughout the fluid.

Furthermore, extensive research has been done both computationally and experimentally on the more complicated geometry of a corner (Wang et al. [2020], Cui et al. [2020]). It is readily established that the inclusion of a boundary results in jet formation provided the stand-off distance is small enough. The stand-off distance plays a crucial part on the intensity of the wall effects and directly changes the magnitude of the bubble migration, jet velocity, Kelvin impulse and jetting angle amongst other things. However, with the inclusion of a second boundary, jetting angles and bubble migration become harder to predict.

One such computational model used to simulate the three-dimensional evolution of a bubble near a boundary is the boundary integral method (Blake et al. [1999]). The boundary integral method (BIM), built upon potential flow theory, uses Green's second identity to evaluate the potential on the bubble surface and surrounding boundaries. This method is grid free in the flow domain and requires only that the potential is calculated at each node on the mesh. The boundary integral method reduces the spatial dimension of the model through discretisation. In doing so, the size of all linear systems are decreased resulting in a lower CPU time and memory requirement (Lee et al. [2007]).

There are many advantages to using the boundary integral method. Not only

does the method require lower CPU time, with the inclusion of initial and boundary conditions, the solutions to the integral equations are unique with less data being required to get efficient results. Furthermore, the mesh generation is simpler than other three-dimensional numerical methods. Since the BIM only requires finding the solution of the boundary integral equations on the surface nodes, it is an easy method to implement the simpler non-Newtonian constituitive equations which only appear through the normal stress tensor at the boundary.

However, there are some disadvantages to using the boundary integral method. Since the method requires the calculation of the velocity potential on the bubble surface, the flow is assumed to be irrotational and so rotational flows can not be simulated. Furthermore, as there is no flow domain, fluid velocities and pressure fields are very rarely analysed. When considering aspects of the flow domain, other numerical methods such as OpenFOAM or finite element method can be used instead. Compressible effects are mostly always consider negligible and so the resulting shock waves from collapse are very rarely simulated apart from very simple axisymmetric models. Finally, the matrices derived in the BIM are asymmetric and very computationally expensive to solve, meaning that the majority of 'run time' is taken by solving these equations.

1.2.2 Non-Newtonian fluids

As stated, the majority of bubble dynamics research has focused on a bubble situated in a Newtonian fluid. However, the applications of cavitation rarely require a Newtonian liquid and instead require liquids with suspended internal polymers such as most bodily fluids or surfactants used in ultrasonic cleaning. Recent cavitation research has focused on the effects of viscoelastic properties of the fluid on bubble evolution.

A ***non-Newtonian*** fluid is one who's stress is non-linearly proportional to it's shear rate. Such examples are fluids which are either shear-thickening whose

viscosity increases with the rate of shear strain, such as cornstarch mixed with water, or are shear-thinning whose viscosity decreases with the rate of shear strain, such as blood or paint. Typical non-Newtonian fluids have either partial or full polymer contribution. ***Viscoelastic*** fluids are fluids which both have a viscosity and elasticity associated with it. Such fluids have a level of strain energy internally stored and therefore perform partial elastic recovery once the deforming stress is removed. The time for the fluid to return to it's pre-deformed state is known as the 'relaxation time' of the fluid. An instantaneous relaxation time applies to an ideal Newtonian fluid such as water, whereas an infinitely large relaxation time corresponds to a perfect Hookean solid.

The behaviour of viscoelastic fluids is characterised by performing experiments in the laboratory using a rheometer. Examples of simple flows that are studied include simple shear flow, extensional flow and oscillatory shear flow. The latter is used to determine the relaxation times of the fluid, a key measure of the viscoelastic nature of the fluid. There are two classes of fluids that often display Maxwell-like behaviour in the normal measuring range ($10^{-2} - 10^{2}$ Hz) with the expected shapes of the curves for the storage and loss moduli and a single relaxation time. These are associative thickener-type polymers (e.g. hydrophobic ethoxylated urethane (HEUR)) (Annable et al. [1994]) and worm-like surfactant micellar systems (e.g. aqueous surfactant solutions containing thread-like micelles) (Fischer and Rehage [1997], Ali and Makhloufi [1997], Cates [1996]). Fluids in the latter class are sometimes called 'living polymers' because if they break under large stresses, they can reconstitute under conditions of rest or low stress.

The bubble behaviours in non-Newtonian fluids are widely encountered in various domains such as decompression sickness, volcanic eruption, glass manufacture, materials, petrochemicals, metallurgy and different dispersed systems (Frank et al. [2013]). It has been shown that the addition of a small amount of water-soluble polymer to a liquid can reduce the chance of cavitation occurring (Ellis [1967]). Certain

additions of polymers have been reported to affect cavitation damage (Shima et al. [1985], Tsujino et al. [1986]), and noise (Tsujino [1987]). The collapse of a cavitation bubble in such fluids can lead to an immense amount of damage to its surrounding boundaries.

Extensive research has been done both numerically and experimentally on the non-spherical evolution of an axisymmetric bubble in a non-Newtonian fluid. The boundary element method has been implemented along with Maxwell's constitutive equation to study the effects of a viscoelastic fluid on a rising bubble (Lind and Phillips [2010a]), with research also being conducted experimentally (Wagner et al. [1999]). Furthermore, results have been established on a bubble near a free surface (Lind and Phillips [2013]), and equally spaced bubbles rising in a viscoelastic fluid (Liu et al. [2013], Pillapakkam et al. [2007], Fraggedakis et al. [2016]) and experimentally on shock wave emissions (Brujan [2019]). A figure depicting the evolution of an experimental bubble in a viscoelastic fluid is shown in Figure 1.3. The experiments and numerical simulations highlighted the negative wake created by the rising bubbles and a large tail-like cusp. However, as the simulations involve rising bubbles, the radius of the bubbles is large to include buoyancy effects, meaning viscous and viscoelastic effects are not as dominant. Furthermore, the three-dimensional effects of the surrounding boundaries are not considered as most numerical and experimental results only consider axisymmetric cases.

Spherical bubble dynamics have also be analysed (Lind and Phillips [2010b]), with a theoretical Rayleigh-Plesset equation for a viscoelastic fluid, which models the evolution of a bubbles radius, being readily established (Gaudron et al. [2015]). For spherical bubbles, it has been shown that a critical value exists for the product of the Reynolds number and the Deborah number, for which complete bubble collapse instead of oscillatory behaviour occurs. However, little research has been performed on a three-dimensional bubble in a viscoelastic fluid.

Simple linear viscoelastic models can only provide meaningful predictions in the

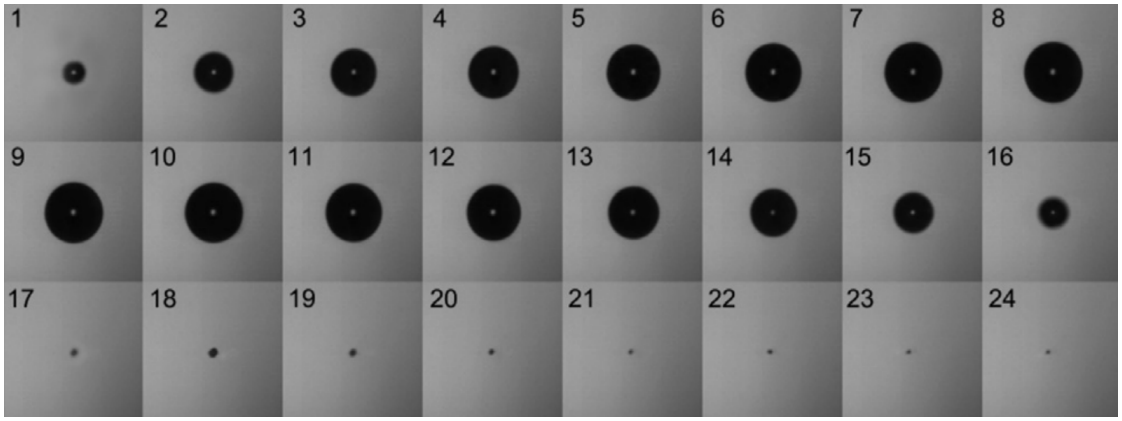


Figure 1.3: The evolution of a spherical experimental bubble in a 0.5% polyacrylamide viscoelastic fluid with the resulting pressure shock wave being separately measured (Brujan [2019]).

limit of small fluid deformations. In general, for a viscoelastic model to satisfy a Bernoulli style equation, that is, an irrotational flow field, we need the extra stress tensor, $\boldsymbol{T}$, used to model the viscoelastic properties of the fluid, to satisfy $\nabla \cdot \boldsymbol{T} = \nabla \psi$ where ψ is some scalar function, $\nabla \cdot$ is the divergence, and ∇ is the grad function. However, under the assumptions described above, the admissibility condition can be satisfied in an approximate sense for moderate to large Reynolds numbers since $\nabla \cdot \boldsymbol{T}$ becomes small compared to inertial terms in the momentum equation in the bulk of the flow (Lind and Phillips [2010b]). Therefore, for simple linear models such as the linear Maxwell model and the Jeffrey model, such a scalar function, ψ, can be found to satisfy a Bernoulli style equation. However, more general models, such as the material Maxwell model, can be employed that provide a more accurate description of viscoelastic effects and also satisfy frame invariance. The restriction to moderate and high Reynolds number flows limits the method to modelling dilute polymer solutions.

1.3 Thesis overview

In this thesis, potential flow theory is implemented using a three-dimensional boundary integral method (BIM) to simulate the evolution of microbubbles near rigid

boundaries in various viscoelastic fluids. The present work is organised into 6 main chapters:

In Chapter 1, we introduced the concept of a cavitation bubble, it's appearance in natural phenomenon, and it's applications in modern day science and engineering. An overview of the development of bubble dynamics with a brief history of both Newtonian and non-Newtonian models are discussed along with a description of viscoelastic fluids and their influence on bubble evolution. Finally, an overview of the boundary integral method is presented.

In Chapter 2, the basic underlying mathematical concepts and physical modelling of a bubble near rigid boundaries are introduced. Under specific fluid conditions, Green's second identity and Green's functions are given to simulate a bubble in infinite fluids, near a flat rigid boundary, and near a corner of various angles. A dynamic boundary condition is derived from Bernoulli's equation to provide a solution for the velocity potential with a kinematic boundary condition providing a description of the bubble surface. The readily established three-dimensional Newtonian viscous model is discussed and the viscoelastic properties of the fluid are introduced via various constitutive equations which appear only through the normal component of the stress tensor under the assumption that the flow has moderate to high Reynolds number. A parametric study is accomplished based on the relaxation time and polymeric viscous contribution of the fluid via nondimensionalisation.

Chapter 3 develops the numerical method to simulate the physical model introduced in Chapter 2. A surface mesh is considered to implement the boundary integral method and a moving least squares method provides a solution for the mean local curvature and tangential velocity. Using Lagrangian integration and fourth order Runge-Kutte method, the bubble surface, velocity potential, and normal component of the stress tensor are updated at each time-step. Finally, a description of the mesh smoothing techniques are provided, with the two main techniques being the elastic mesh technique and the hybrid mesh technique which focuses on reducing

the mesh density through elasticity on the surface of the bubble allowing for a more stable jet formation.

In Chapter 4, the physical and numerical model is implemented with the boundary integral method to simulate a microbubble in various Maxwell fluids. A bubble is first introduced in an infinite Maxwell fluid with various Deborah numbers to analyse the effect of the relaxation time of the fluid on the bubbles radius history and velocity over the first two cycles of oscillation. The Green's function is then obtained to simulate the same viscoelastic fluids with a bubble near both a flat rigid boundary and a corner of various angles. In doing so, the effects of the relaxation time on the Kelvin impulse, bubble migration, bubble size, jet profiles, and jetting angles are given. Further discussion is then given on the influence of the domain size and stand-off distances between the bubble and the rigid boundaries. Finally, the large scale effects of both the Deborah number and Reynolds number are shown.

In a similar manner to Chapter 4, Chapter 5 provides analysis on the evolution of a bubble in various Jeffrey fluids in different geometric settings. A bubble is first situated in infinite Jeffrey fluids with differing viscosity ratios where the polymeric and solvent contributions of the fluid are changed. In doing so, the influence on the bubble radius histories and surface velocity are discussed. Once again, the Green's function is implemented to model the bubble near both a flat rigid boundary and a corner of various angles. Results are then presented on the Kelvin impulse, bubble migration, jetting angle, jet profile, and bubble size. The large scale effects of the Deborah number and Reynolds number are discussed.

Finally, Chapter 6 provides a summary of the thesis, the conclusions drawn, and the possible future developments of bubbles in non-Newtonian fluids.

CHAPTER 2

MATHEMATICAL & PHYSICAL MODEL

In this chapter, we describe the physical and mathematical model for 3D bubble dynamics in a non-Newtonian liquid, based on potential flow theory. This consists of the boundary integral equation for the velocity potential, the kinematic and dynamic boundary conditions, as well as the initial conditions. We discuss two models for non-Newtonian liquids, the Maxwell and Jeffrey models, and their constitutive equations.

2.1 Potential flow model

2.1.1 Green's second identity

Consider a non-spherical bubble with surface, S_B, and volume, V, situated in an incompressible fluid of domain Ω. Assume also that the fluid motion is irrotational with all relative velocities being significantly smaller than the corresponding speed of sound in the fluid. We can assume that viscous and viscoelastic effects are negligible and that the flow is inertia dominated in the bulk, since we are concerned with moderate to high Reynolds number flow and high speed bubble expansion and collapse. However, since we are required to satisfy the physical stress boundary conditions, we can consider a thin boundary layer near the surface of the bubble for which these effects become apparent, i.e where the flow is no longer inertia dominated. The

ability to accurately model viscous and viscoelastic irrotational flows arises from the small amount of vorticity generated at the bubble's free surface. However, the shear stress-free free surface generates little vorticity and so flow within the boundary layer is only slightly perturbed from irrotational (Batchelor [1967]). Therefore, within a reasonable level of approximation, the bulk of the fluid can be measured to be inviscid and irrotational. The thickness of the viscoelastic boundary layer at the surface is determined by the Reynolds number of the fluid and given by $\mathcal{O}(R_0/\sqrt{Re})$ for some initial radius R_0 (Batchelor [1967], Boulton-Stone and Blake [1993]).

Hence, assuming that the viscous and viscoelastic effects appear only through the normal stress balance at the bubble surface and that the flow is entirely irrotational provides an accurate description of the physical problem (Lind and Phillips [2013]). The viscoelastic effects can then be modelled using Maxwell's or Jeffrey's constitutive equation which gives the simplest description but still provides significant elastic effects. As such, the linearity of the model provides no additional stress contribution in the bulk of the fluid. Hence, as with the viscous models previously investigated, the viscoelastic effects only appear via the normal stress balance condition. The analysis of a viscoelastic fluid provided here is kept entirely general and is applicable to any irrotational flow (Lind and Phillips [2010b]).

Assuming that the flow is irrotational, that is, $\boldsymbol{w}^* = \nabla^* \times \boldsymbol{u}^* = 0$, we can write the velocity, $\boldsymbol{u}^*$, in terms of a velocity potential ϕ^*, where $\boldsymbol{u}^* = \nabla^* \phi^*$. Therefore, via the continuity equation, Laplace's equation in the fluid is given by

$$\nabla^{*2} \phi^* = 0. \tag{2.1.1}$$

The boundary integral method can be implemented with Green's second identity providing a solution for the velocity potential, ϕ^*, and it's normal derivative, $\partial\phi^*/\partial n$, on the bubble surface and surrounding boundaries respectively. This is achieved by representing it as a surface integral over the bubble surface. Green's second identity,

which is valid provided ϕ^* and $G(\boldsymbol{r}^*, \boldsymbol{q}^*)$ are both twice continuously differentiable on V, is given by

$$\int_V (G(\boldsymbol{r}^*, \boldsymbol{q}^*)\nabla^{*2}\phi^*(\boldsymbol{q}^*) - \phi^*(\boldsymbol{q}^*)\nabla^{*2}G(\boldsymbol{r}^*, \boldsymbol{q}))^* dV \\ = \int_{\partial\Omega} \Big(\frac{\partial\phi^*(\boldsymbol{q}^*)}{\partial \boldsymbol{n}} G(\boldsymbol{r}, \boldsymbol{q}^*) - \phi^*(\boldsymbol{q}^*)\frac{\partial G(\boldsymbol{r}^*, \boldsymbol{q}^*)}{\partial \boldsymbol{n}}\Big) dS(\boldsymbol{q}^*). \tag{2.1.2}$$

where $\boldsymbol{r}^*$ is a field point, $\boldsymbol{q}^*$ is a source point, $\boldsymbol{n} = (n_x, n_y, n_z)$ is the outward facing normal at the surface, and $\partial\Omega = S_B \cup S_R$ represents every boundary in the domain, Ω, with S_R being the surfaces of all rigid boundaries. The normal derivative, $\partial/\partial n$ is defined as $\boldsymbol{n}\cdot\nabla$. Here, $G(\boldsymbol{r}^*, \boldsymbol{q}^*)$ is the Green's function for a semi-infinite domain which is divided by two rigid boundaries of angle $\alpha = \pi/l$, which provides a solution to Laplace's equation. This is given by,

$$G(\boldsymbol{r}^*, \boldsymbol{q}^*) = \frac{1}{|\boldsymbol{r}^* - \boldsymbol{q}^*|} + \sum_{i=1}^{2l-1} \frac{1}{|\boldsymbol{r}^* - \boldsymbol{q}_i^*|} \tag{2.1.3}$$

for some $l \in \mathbb{N}$, where $\boldsymbol{q}_i^*$ are the image points of $\boldsymbol{q}^*$. We now apply the Green's function (2.1.3) to Green's second identity (2.1.2). Imagine a field point, $\boldsymbol{r}^*$, located in the domain Ω consisting of the bubble surface, the flow field and the surface of the boundary along with the surface of a sphere, S_ϵ, with centre $\boldsymbol{r}^*$ and radius given by $|\boldsymbol{r}^* - \boldsymbol{q}^*| = \epsilon$. We have the boundary condition

$$\nabla^2 G = 0 \text{ for } \boldsymbol{r} \in \Omega \setminus \Omega_\epsilon. \tag{2.1.4}$$

Therefore, the Green's function for Laplace's equation can be expressed as

$$G(\boldsymbol{r}^*, \boldsymbol{q}^*) = \frac{1}{|\boldsymbol{r}^* - \boldsymbol{q}^*|} = \frac{1}{\epsilon}. \tag{2.1.5}$$

Therefore,

$$\boldsymbol{n}\cdot\nabla^* G = -\frac{\boldsymbol{q}^*-\boldsymbol{r}^*}{|\boldsymbol{q}^*-\boldsymbol{r}^*|}\cdot\frac{\boldsymbol{q}^*-\boldsymbol{r}^*}{|\boldsymbol{q}^*-\boldsymbol{r}^*|^3} = \frac{-1}{|\boldsymbol{q}^*-\boldsymbol{r}^*|^2} = \frac{-1}{\epsilon^2}. \tag{2.1.6}$$

The surface integral in Green's second identity now becomes

$$\begin{aligned}\int_{S\cup S_\epsilon}(\phi^*_{\boldsymbol{n}}G-\phi^*G_{\boldsymbol{n}})dS &- \int_{S_\epsilon}(\phi^*_{\boldsymbol{n}}G-\phi^*G_{\boldsymbol{n}})dS \\ &= \int_{S\cup S_\epsilon}(G\nabla^*\phi^*-\phi^*\nabla^*G)\cdot\boldsymbol{n}dS - \int_{S_\epsilon}(\phi^*_{\boldsymbol{n}}G-\phi^*G_{\boldsymbol{n}})dS, \\ &= \int_{\Omega\setminus\Omega_\epsilon}\nabla^*\cdot(G\nabla^*\phi^*-\phi^*\nabla^*G)dV + \left(\frac{\phi^*}{\epsilon^2}-\frac{\phi^*_{\boldsymbol{n}}}{\epsilon}\right)\int_{S_\epsilon}dS.\end{aligned} \tag{2.1.7}$$

Observe that,

$$\int_{\Omega\setminus\Omega_\epsilon}\nabla^*\cdot(\nabla^*\phi^*G-\phi^*\nabla^*G)dV = \int_{\Omega\setminus\Omega_\epsilon}(G\nabla^{2*}\phi^*-\nabla^*\phi^*\nabla^*G)dV = 0, \tag{2.1.8}$$

via the boundary condition. Hence,

$$\int_S\Big(\frac{\partial\phi^*}{\partial\boldsymbol{n}}G-\phi^*\frac{\partial G}{\partial\boldsymbol{n}}\Big)dS = \left(\frac{\phi^*}{\epsilon^2}-\frac{\phi^*_{\boldsymbol{n}}}{\epsilon}\right)\int_{S_\epsilon}dS = \frac{\phi^*}{\epsilon^2}\int_{S_\epsilon}dS - \frac{\phi^*_{\boldsymbol{n}}}{\epsilon}\int_{S_\epsilon}dS. \tag{2.1.9}$$

Taking the limit as $\epsilon\to\infty$ to consider just the point itself, we obtain

$$\lim_{\epsilon\to 0}\left(\frac{\phi^*}{\epsilon^2}\int_{S_\epsilon}dS - \frac{\phi^*_{\boldsymbol{n}}}{\epsilon}\int_{S_\epsilon}dS\right) = \phi^* c(\boldsymbol{r}), \tag{2.1.10}$$

since

$$\int_{S_\epsilon}dS = O(\epsilon^2), \tag{2.1.11}$$

where $c(\boldsymbol{r})$ is the solid angle. When $\boldsymbol{r}\in\Omega\setminus S_B$, S_ϵ represents a sphere around the point $\boldsymbol{r}$ with radius ϵ. Therefore, the solid angle for such a point is given by

$$c(\boldsymbol{r}) = \int_{S_\epsilon}\frac{dS}{\epsilon^2} = \frac{4\pi\epsilon^2}{\epsilon^2} = 4\pi. \tag{2.1.12}$$

When $\boldsymbol{r} \in S_B$, S_ϵ now represents a semi-sphere around the point $\boldsymbol{r}$ with radius ϵ. Therefore, the solid angle for such a point is given by

$$c(\boldsymbol{r}) = \int_{S_\epsilon} \frac{dS}{\epsilon^2} = \frac{2\pi\epsilon^2}{\epsilon^2} = 2\pi. \tag{2.1.13}$$

Hence, we arrive at the required form of Green' second identity,

$$c(\boldsymbol{r}^*, t^*)\phi^*(\boldsymbol{r}^*, t^*) = \int_{\partial\Omega} \Big(\frac{\partial \phi^*(\boldsymbol{q}^*, t^*)}{\partial n} G(\boldsymbol{r}^*, \boldsymbol{q}^*) - \phi^*(\boldsymbol{q}^*, t^*) \frac{\partial G(\boldsymbol{r}^*, \boldsymbol{q}^*)}{\partial n} \Big) dS, \tag{2.1.14}$$

where $c(\boldsymbol{r}^*, t^*)$ is the solid angle given by

$$c(\boldsymbol{r}^*, t^*) = \begin{cases} 4\pi, & \text{if } \boldsymbol{r}^* \in \Omega/\partial\Omega, \\ 2\pi, & \text{if } \boldsymbol{r}^* \in \partial\Omega. \end{cases} \tag{2.1.15}$$

2.1.2 Kinematic and dynamic boundary conditions

The kinematic boundary condition requires that a particle on the bubble surface remains on the bubble surface for all time and is given by

$$\boldsymbol{u}^*\big|_S = \frac{D\boldsymbol{r}_p^*}{Dt^*} = \nabla^*\phi^*\big|_S, \tag{2.1.16}$$

where $\mathbf{r}_p^*$ is some arbitrary particle on the surface of the bubble. The dynamic boundary condition on the bubble surface is given by

$$(\boldsymbol{\sigma}^L - \boldsymbol{\sigma}^B) \cdot \boldsymbol{n} = 2\sigma\kappa^*, \tag{2.1.17}$$

where $\boldsymbol{\sigma}_L$ and $\boldsymbol{\sigma}_B$ represent the normal stress in the liquid and bubble respectively, σ is the surface tension of the bubble, and κ^* is the mean local curvature. By the

definition of normal stress,

$$\sigma_{nn}^{L} = -P_L^* + T_{nn}^*, \tag{2.1.18}$$

$$\sigma_{nn}^{B} \approx -P_B, \tag{2.1.19}$$

since $\mu_B \ll \mu_L$, where P_B is the internal pressure inside the bubble acting on the surface, P_L^* is the pressure in the liquid, and T_{nn}^* represents the normal component of the deviatoric stress tensor. Hence,

$$P_L^* = P_B - 2\sigma\kappa^* + T_{nn}^*. \tag{2.1.20}$$

To derive an expression for the pressure inside the bubble, P_B, we assume the bubble contains a uniform and non-condensable gas (Best and Kucera [1992]). A constant internal vapour pressure can be assumed by an equal evaporation during expansion stage and condensation during collapse (Lee et al. [2007]). The pressure inside the bubble for an adiabatic gas is frequently given by

$$P_B = P_v + P_g = P_v + P_{g0}\Big(\frac{V_0}{V}\Big)^{\xi}, \tag{2.1.21}$$

where P_{g0} is the initial partial pressure of the gas, P_v is the constant vapour pressure, V and V_0 are the current and initial volume of the bubble respectively, and ξ is the heat capacity ratio.

Hence, using the expressions for P_L^*, Bernoulli's equation for potential flow is given by

$$\frac{D\phi^*}{Dt^*} = \frac{1}{2}|\nabla^*\phi^*|^2 - \frac{1}{\rho}\Big(P_v + P_{g0}\Big(\frac{V_0}{V}\Big)^{\xi} - 2\sigma\kappa^* + T_{nn}^*\Big) + \frac{P_0}{\rho} - gz^*, \tag{2.1.22}$$

where ρ is the density of the surrounding fluid, P_0 is the far-field ambient fluid pressure, and g is the constant acceleration due to gravity.

2.2 Spherical bubble theory for validation

2.2.1 Rayleigh-Plesset equation

In this section, we derive the Rayleigh-Plesset equation for spherical bubbles. This is used to validate the potential flow theory when developing the three-dimensional boundary integral method. Consider a spherical bubble of radius $R^*(t^*)$, in a infinite domain of liquid whose ambient far-field pressure is given by P_0. Assume that the liquid density, ρ and the total dynamic viscosity, μ_L are constant. The radial position from the centre of the bubble is given as r^*, and the pressure and radial outward velocity are denoted $p^*(r^*, t^*)$ and $u^*(r^*, t^*)$ respectively. To conserve mass, we must have

$$u^*(r^*, t^*) = \frac{F(t^*)}{r^{*2}}, \tag{2.2.1}$$

where $F(t^*)$ is related to $R^*(t^*)$ via the kinematic boundary condition. Since

$$u^*(R^*, t^*) = \frac{dR^*}{dt^*}, \tag{2.2.2}$$

on the bubble surface, we have that,

$$F(t^*) = R^{*2}\frac{dR^*}{dt^*}. \tag{2.2.3}$$

Note that, the Navier-Stokes equation in the r^* direction is given by,

$$\frac{-1}{\rho}\frac{\partial P^*}{\partial r} = \frac{\partial u^*}{\partial t^*} + u^*\frac{\partial u^*}{\partial r^*} - \nu_L\Big(\frac{1}{r^{*2}}\frac{\partial}{\partial r^*}\Big(r^{*2}\frac{\partial u^*}{\partial r^*}\Big) - \frac{2u^*}{r^*}\Big). \tag{2.2.4}$$

Substituting the expression for $F(t^*)$ from equation (2.2.3) yields,

$$\frac{-1}{\rho}\frac{\partial P^*}{\partial r} = \frac{1}{r^{*2}}\frac{dF(t^*)}{dt^*} - \frac{2F(t^*)^2}{r^{*5}}. \tag{2.2.5}$$

Hence, integrating with respect to $\boldsymbol{r}$,

$$\frac{P_L^* - P_0}{\rho} = \frac{1}{2}\frac{F(t^*)^2}{r^{*4}} - \frac{1}{r^*}\frac{dF(t^*)}{dt^*}, \tag{2.2.6}$$

since $P_L^* \to P_0$ as $r^* \to \infty$. From the dynamic boundary condition (2.1.17), the net force in the radially outward direction per unit area in the absence of mass transport is given by,

$$\sigma_{rr}\big|_{r=R} + P_B - 2\sigma\kappa^* = 0. \tag{2.2.7}$$

Hence, substituting for P_L^* from equation (2.1.20) and using the fact that $F = R^{*2}dR^*/dt^*$, we arrive at the generalised Rayleigh-Plesset equation, given by,

$$\frac{P_B - P_0}{\rho} = R^*\frac{d^2R^*}{dt^{*2}} + \frac{3}{2}\Big(\frac{dR^*}{dt^*}\Big)^2 - \frac{T_{nn}^*}{\rho} + \frac{2\sigma\kappa^*}{\rho}. \tag{2.2.8}$$

Note that the Rayleigh-Plesset equation is a second order ordinary differential equation and can therefore be solved analytically, and as such, can be used to validate the radius history as calculated using the boundary integral method and the three-dimensional bubble code developed in Chapter 3. The Rayleigh-Plesset equation itself is inappropriate for three-dimensional bubble mechanics because it assumes that the bubble remains spherical for all time, and that the bubble is in an infinite domain space. Whereas, the bubble is mostly situate in semi-infinite domains throughout this thesis to analyse the non-spherical effects of the viscoelastic fluid.

2.2.2 Potential calculation

For a spherically symmetric flow, Laplace's equation is given by

$$\nabla^{*2}\phi^* = \frac{1}{r^{*2}}\frac{\partial}{\partial r^*}\Big(r^{*2}\frac{\partial\phi^*}{\partial r^*}\Big) = 0. \tag{2.2.9}$$

Integrating both sides with respect to $\boldsymbol{r}$, the corresponding velocity is given by

$$\boldsymbol{u}^* = \nabla^* \phi^* = \frac{\partial \phi^*}{\partial r^*} \hat{\boldsymbol{r}}^* = \frac{A}{r^{*2}} \hat{\boldsymbol{r}}^*, \tag{2.2.10}$$

where the velocity potential, ϕ^*, is given by

$$\phi^* = -\frac{A(t^*)}{r^*} + B(t^*), \tag{2.2.11}$$

and A and B are arbitrary functions of t^*. Now consider the radial motion of a spherical gas bubble in the absence of gravity. The volume flux of a sphere, m, is given by

$$m = 4\pi r^{*2} u^*(r^*, t^*) = 4\pi A. \tag{2.2.12}$$

For incompressible flow, the flux equals the rate of change of the bubble volume, i.e

$$4\pi R^{*2} \Big(\frac{A}{R^{*2}} \Big) = \frac{\partial}{\partial t^*} \Big(\frac{4}{3} \pi R^{*3} \Big) = 4\pi R^{*2} \frac{dR^*}{dt^*}, \tag{2.2.13}$$

$$\implies A = R^{*2} \frac{dR^*}{dt^*}, \quad \boldsymbol{u}^* = \frac{R^{*2}}{r^{*2}} \frac{dR^*}{dt^*} \hat{\boldsymbol{r}}^*, \quad \phi = \frac{-R^{*2}}{r^*} \frac{dR^*}{dt^*}. \tag{2.2.14}$$

Therefore, in the normal direction

$$\phi_n^* = u_r^* = \frac{R^{*2}}{r^{*2}} \frac{dR^*}{dt}. \tag{2.2.15}$$

Hence,

$$\phi_{nn}^* = \frac{\partial}{\partial r^*} \Big(\frac{R^{*2}}{r^{*2}} \frac{dR^*}{dt} \Big) = -\frac{2R^{*2}}{r^{*3}} \frac{dR^*}{dt}. \tag{2.2.16}$$

Therefore, on the bubble surface

$$\phi_{nn}^*|_{r^*=R^*} = -\frac{2}{R^*} \frac{dR^*}{dt} = -\frac{2}{R^*} \phi_n^*|_{\boldsymbol{r}^*=R^*}. \tag{2.2.17}$$

In Chapter 4, the calculation of $\phi_{nn}^*|_{r^*=R^*}$ using spherical bubble theory is com-

pared to the calculation via the boundary integral method to validate the three-dimensional bubble code.

2.3 Nondimensionalisation

For the remainder of the thesis, the non-spherical bubble model is converted into a nondimensional problem by introducing the following dimensionless quantities,

$$\boldsymbol{r}^* = R_0\boldsymbol{r}, \quad t^* = R_0\sqrt{\frac{\rho}{P_0 - P_v}}t, \quad \phi^* = R_0\sqrt{\frac{P_0 - P_v}{\rho}}\phi, \quad \kappa^* = \frac{\kappa}{R_0}, \tag{2.3.1}$$

where R_0 is the initial radius of the bubble. The stand-off distances towards the near and far boundaries, γ_N and γ_F, are normalised using the initial bubble radius,

$$\gamma_N = \frac{s_N}{R_0}, \text{ and } \gamma_F = \frac{s_F}{R_0}, \tag{2.3.2}$$

where s_N and s_F are the initial dimensional distances between the bubble centre and the near and far walls, respectively. For a flat rigid boundary, $\gamma_N = \gamma_F = \gamma$.

Hence, we obtain the dimensionless model for the non-spherical bubble

$$c(\boldsymbol{r}, t)\phi(\boldsymbol{r}, t) = \int_{\partial\Omega} \Big(\frac{\partial\phi(\boldsymbol{q}, t)}{\partial n}G(\boldsymbol{r}, \boldsymbol{q}) - \phi(\boldsymbol{q}, t)\frac{\partial G(\boldsymbol{r}, \boldsymbol{q})}{\partial n}\Big)dS, \tag{2.3.3}$$

$$\boldsymbol{u}\big|_S = \frac{D\boldsymbol{r}_p}{Dt} = \nabla\phi\big|_S, \tag{2.3.4}$$

$$\frac{D\phi}{Dt} = 1 + \frac{1}{2}|\nabla\phi|^2 - \delta^2 z - \varepsilon(\frac{V_0}{V})^\xi + \frac{2\kappa}{We} - T_{nn}, \tag{2.3.5}$$

Here, $\delta = \sqrt{gR_0\rho/(P_0 - P_v)}$ is the buoyancy parameter which provides a measure of the strength of the buoyancy force where a greater force leads to more uplift on the bubble and therefore increases bubble migration vertically upwards. Note that, for all cases considered in this thesis, the buoyancy force is considered negligible, i.e $\delta = 0$, however is non-negligible when validating the three-dimensional code

with experimental data. The parameter $\varepsilon = P_{g0}/(P_0 - P_v)$ is a measure of initial excess pressure inside the bubble relative to the ambient pressure. The greater the value of ε, the greater the difference in pressure across the bubble surface leading to larger bubble expansion and inertia. This in turn leads to a more violent collapse and jetting. The Weber number given by $We = R_0(P_0 - P_v)/\sigma$, is a measure of the importance of fluid inertia compared to surface tension (Blake et al. [1999]). A larger Weber number reduces the importance of surface tension on the bubbles expansion.

The dimensionless Rayleigh-Plesset equation is given by

$$R\frac{d^2R}{dt^2} = \varepsilon\Big(\frac{R_0}{R}\Big)^{3\gamma} - 1 - \frac{3}{2}\Big(\frac{dR}{dt}\Big)^2 - \frac{2}{We}\frac{1}{R} - T_{nn}, \tag{2.3.6}$$

which analytically provides the dimensionless bubble history for a spherical bubble in an infinite fluid. Note that the first two terms on the right hand side of equation (2.3.6) oscillate between a negative and positive value with the ratio between R_0 and R varying over the bubbles lifetime, and the third term also oscillating between negative and positive as the velocity of the bubble surface varies. This gives the radius history its oscillatory behaviour, with the surface tension and viscosity terms providing damping.

2.4 Initial conditions

A technique for developing a relationship for the initial bubble radius was given by Qianxi Wang et al, in the absence of viscosity and surface tension (Wang et al. [2005]). This is so the bubble is initiated at this given initial dimensionless radius so that the maximum dimensionless bubble radius is given by $R_{max} = 1$. In the absence of viscosity and surface tension, if the dimensionless pressure difference ε and ratio of specific heats, ζ are known, then the dimensionless initial radius can be found. In doing so, the radius history can be nicely plotted and analysed.

Given the nondimensional Rayleigh-Plesset equation

$$R\frac{d^2R}{dt^2}+\frac{3}{2}\Big(\frac{dR}{dt}\Big)^2=\varepsilon\Big(\frac{R_0}{R}\Big)^{3\xi}-1, \tag{2.4.1}$$

the initial bubble radius, R_0 can be computed provided that an initial non-zero radial velocity is known. Multiplying both sides by $2R^2dR/dt$ yields

$$2R^3\frac{dR}{dt}\frac{d^2R}{dt^2}+3R^2\Big(\frac{dR}{dt}\Big)^3=(2\varepsilon R_0^{3\xi}R^{2-3\xi}-2R^2)\frac{dR}{dt}. \tag{2.4.2}$$

Observe that

$$2R^3\Big(\frac{dR}{dt}\Big)^2+3R^2\Big(\frac{dR}{dt}\Big)^3=\frac{d}{dt}\Big(R^3\Big(\frac{dR}{dt}\Big)^2\Big). \tag{2.4.3}$$

Hence,

$$\frac{d}{dt}\Big(R^3\Big(\frac{dR}{dt}\Big)^2\Big)=(2\varepsilon R_0^{3\xi}R^{2-3\xi}-2R^2)\frac{dR}{dt}. \tag{2.4.4}$$

Integrating with respect to time yields

$$R^3\Big(\frac{dR}{dt}\Big)^2=\frac{2\varepsilon R_0^{3\xi}R^{3-3\xi}}{3-3\xi}-\frac{2}{3}R^3+c. \tag{2.4.5}$$

We now set appropriate boundary conditions to find c. At the boundary's $R=R_0$ and $R=1$, with 1 being the maximum dimensionless bubble radius, we set

$$\frac{dR}{dt}=0 \text{ at } R=R_0,1. \tag{2.4.6}$$

Hence, using the condition at $R=R_0$,

$$0=\frac{2}{3}\Big(\varepsilon\frac{R_0^3}{1-\xi}-R_0^3\Big)+c. \tag{2.4.7}$$

Thus,

$$c=\frac{2}{3}R_0^3\Big(1-\frac{\varepsilon}{1-\xi}\Big). \tag{2.4.8}$$

Now using this expression for c and the boundary condition at $R = 1$,

$$0 = \frac{2}{3}\Big(\frac{\varepsilon R_0^{3\xi}}{1-\xi} - 1 + R_0^3 - \frac{\varepsilon R_0^3}{1-\xi}\Big), \tag{2.4.9}$$

and so we end up with a relationship for the initial radius given by

$$\frac{\varepsilon(R_0^{3\xi} - R_0^3)}{1-\xi} = 1 - R_0^3. \tag{2.4.10}$$

2.5 Viscoelastic modelling

In this section, we introduce the weakly viscous modelling to approximate the viscous effects of liquids. The normal component of the stress tensor, T_{nn}, is defined differently depending on the fluid in which the bubble is situated. Conventionally, only a Newtonian fluid is considered for three-dimensional bubble mechanics. However, for axisymmetric bubble mechanics, the Maxwell and Jeffery models have been developed which we extend to the three-dimensional cases.

2.5.1 Newtonian model

For a Newtonian fluid, the dimensional, normal component of the stress tensor, T^*_{nn} is proportional to the rate of strain, $\dot{\gamma}^*_{nn}$, i.e

$$T^*_{nn} = 2\mu_L \dot{\gamma}^*_{nn} = 2\mu_L \frac{\partial^2 \phi^*}{\partial n^2} \tag{2.5.1}$$

for irrotational flow. However, here it is assumed that the viscosity in the bubble, μ_B, is much smaller than the viscosity in the liquid, μ_L. As such, the tangential shear stress at the bubble surface should be zero. But this is not the case for irrotational flow. To overcome this issue, a pressure correction term, p_{vc}, is introduced acting in the direction of the normal at the surface. This viscous correction pressure is then

assumed to be proportional to the normal stress such that

$$p_{vc} \approx 2\mu_L \dot{\gamma}^*_{nn} = 2\mu_L \frac{\partial^2 \phi^*}{\partial n^2} \implies p_{vc} = -2C\mu_L \frac{\partial^2 \phi^*}{\partial n^2}, \tag{2.5.2}$$

for some constant of proportionality, C, where p_{vc} satisfies,

$$\int_S u_n(-p_{vc})dS = \int_S \boldsymbol{u}_\tau \cdot \boldsymbol{\tau}_s dS, \tag{2.5.3}$$

to obey the conservation of energy (Manmi and Wang [2017]), where $\boldsymbol{\tau}_s$ is the shear stress at the bubble surface. The shear stress can be obtained by considering the rate of energy dissipation, D, given by

$$D = \int_S \boldsymbol{u} \cdot \boldsymbol{\sigma} \cdot \boldsymbol{n} dS = 2\mu_L \int_S u_n \frac{\partial^2 \phi^*}{\partial n^2} dS + \int_S \boldsymbol{u}_\tau \cdot \boldsymbol{\tau}_S dS, \tag{2.5.4}$$

Hence, substituting (2.5.2) into the rate of energy dissipation equation gives

$$D = 2\mu_L(1+C) \int_S \frac{\partial \phi^*}{\partial n} \frac{\partial^2 \phi^*}{\partial n^2} dS. \tag{2.5.5}$$

The rate of energy dissipation, D, can also be computed by considering the surface integral on the boundary for the irrotational flow (Lamb [1924]),

$$D = 2\mu_L \int_S \nabla\phi \frac{\partial \nabla \phi^*}{\partial n} dS. \tag{2.5.6}$$

Hence, by combining both forms of D, C is given by

$$C = \frac{\int_S \nabla^* \phi^* \cdot \frac{\partial \nabla^* \phi^*}{\partial n} dS}{\int_S \frac{\partial \phi^*}{\partial n} \frac{\partial^2 \phi^*}{\partial n^2} dS} - 1. \tag{2.5.7}$$

Hence, including the pressure correction term, T^*_{nn} for a Newtonian fluid is given by

$$T^*_{nn} = 2\mu_L \dot{\gamma}^*_{nn} = 2(1+C)\mu_L \frac{\partial^2 \phi^*}{\partial n^2}. \tag{2.5.8}$$

Nondimensionalising as before,

$$T_{nn} = 2\mu_L \dot{\gamma}_{nn} = \frac{2(1+C)}{Re}\frac{\partial^2 \phi}{\partial n^2}, \tag{2.5.9}$$

where $Re = R_0\sqrt{(P_0 - P_v)\rho}/\mu_L$ is the Reynolds number which measures the ratio between the inertial and viscous forces in the fluid. At low Reynolds number, viscous effects dominate which leads to laminar type flows. Whereas, a very high Reynolds number means the flow is dominated by inertia resulting in turbulence. Our modelling assumes a moderate to high Reynolds number.

2.5.2 Maxwell's model

Maxwell's constitutive equation is used to model the non-Newtonian properties of the fluid as it is the simplest model to provide significant viscoelastic effects. Here, the fluid is assumed to be purely polymeric with no solvent contribution. The equation yields a general irrotational equation of motion and provides no additional contribution to stress in the bulk and so the viscoelastic effects only appear in the normal stress balance condition. However, the model comes with the limitation of only being applicable for small deformations (Bird et al. [1987]). For general constitutive equations we cannot find a function ψ that satisfies $\nabla \cdot \boldsymbol{T} = \nabla\psi$ for general irrotational flows (Joseph and Liao [1994]), where $\boldsymbol{T}$ is the stress tensor. In these situations we have $\nabla \times \nabla \cdot \boldsymbol{T} \neq 0$ even though $\nabla \times \boldsymbol{u} = 0$, for velocity $\boldsymbol{u}$. We cannot always find a function ψ satisfying the above equation so that not all fluids will satisfy a Bernoulli equation. However, Bernoulli equations are admissible for linear Maxwell and Jeffrey's fluids. In the case of a inviscid Newtonian fluid, a viscous Newtonian fluid, a linear Maxwell fluid, and a linear Jeffrey fluid, $\psi = 0$. Thus, a 'material' Maxwell model is used. The material Maxwell model means that the material time derivative collapses to a time derivative in the particle reference frame and can therefore be easily calculated (Lind and Phillips [2010a]).

For a linear Maxwell fluid, the stress tensor, $\boldsymbol{T}^*$, is given by Maxwell's constitutive equation,

$$\boldsymbol{T}^* + \lambda_1 \frac{\partial \boldsymbol{T}^*}{\partial t^*} = 2\mu_L \dot{\boldsymbol{\gamma}}^*, \tag{2.5.10}$$

where λ_1 is the relaxation time of the fluid. The relaxation time can be described as the time required for a the shear stress on the fluid to return to zero under constant-strain conditions (Owens and Phillips [2002]). A more fluid-like material will require less time for this return to occur and as such will have a lower associated relaxation time. This time is considered to be instantaneous for Newtonian fluids and therefore, $\lambda_1 = 0$. On the other hand, a Hookean elastic linear solid will never relax to zero and is assumed to have an infinite relaxation time. In reality both of these extremes are never realised (Note that the relaxation time of water is $10^{-12}s$ whereas glass can exceed 28 hours. As the relaxation time increases, the fluid appears to have more solid-like characteristics.

An important note is that even though the relaxation time is not directly related to the viscosity and density of the fluid, in many fluids, an increase in the relaxation time will imply that the viscosity and/or the density will also be different. For example, blood has a higher relaxation time than water and the viscosity follows a shear-thinning type behaviour. However, the density of blood is comparable to pure water.

On the bubble surface the shear stress vanishes. Assuming that $\boldsymbol{T}^*$ is isotropic results in the relationship

$$\boldsymbol{T}^* = T^*_{nn}\delta_{ij}. \tag{2.5.11}$$

Hence, upon substitution into equation (2.5.10),

$$\lambda_1 \frac{\partial T^*_{nn}}{\partial t^*} + T^*_{nn} = 2\mu_L \dot{\gamma}^*_{nn} = 2\mu_L \frac{\partial^2 \phi^*}{\partial n^2}. \tag{2.5.12}$$

As for the Newtonian case, a constant, C, is introduced to compensate for the

tangential shear stress, i.e

$$\lambda_1 \frac{\partial T^*_{nn}}{\partial t^*} + T^*_{nn} = 2(1+C)\mu_L \frac{\partial^2 \phi^*}{\partial n^2}. \tag{2.5.13}$$

Nondimensionalising as before gives

$$De \frac{\partial T_{nn}}{\partial t} + T_{nn} = \frac{2(1+C)}{Re} \frac{\partial^2 \phi}{\partial n^2}. \tag{2.5.14}$$

where

$$De = \frac{\lambda_1}{R_0} \Big(\frac{P_0 - P_v}{\rho} \Big)^{\frac{1}{2}}, \tag{2.5.15}$$

is the Deborah number of the fluid which is a measure of the relative relaxation time of the fluid compared to the observation time or time-scale of the flow (Lind [2010]). As such, viscoelastic fluids do not have one Deborah number associated with them as the time-scale will vary depending on the flow process. For example, fluids can appear to show solid-like characteristics over very short time scales but behave more like a fluid over very long time periods. One of the better known examples of this is 'bouncing putty' which will find it's own level over a sufficient amount of time. Note that as λ_1 approaches zero, i.e, the relaxation time of the fluid becomes instantaneous, the Maxwell model reverts back to the Newtonian model.

2.5.3 Jeffrey's model

Now consider a Jeffrey's fluid (Lind and Phillips [2010b]). This is a simple extension of the Newtonian and Maxwell models which are respectively either entirely solvent or polymeric. The fluid is now assumed to have both a solvent and polymeric contribution and the Jeffrey model provides a description for the ratio between the two contributions. The stress tensor $\boldsymbol{T}^*$ is modelled using the Jeffrey's constitutive equation given by

$$\boldsymbol{T}^* + \lambda_1 \frac{D\boldsymbol{T}^*}{Dt^*} = 2\mu_L \Big(\dot{\boldsymbol{\gamma}}^* + \lambda_2 \frac{D\dot{\boldsymbol{\gamma}}^*}{Dt^*} \Big), \tag{2.5.16}$$

where λ_1 is once again the relaxation time and λ_2 is the retardation time given by

$$\lambda_2 = \frac{\mu_s}{\mu_s + \mu_p}. \tag{2.5.17}$$

Here, μ_s and μ_p are the solvent and polymeric viscosities of the fluid respectively, with

$$\mu_s = \frac{\lambda_2}{\lambda_1}\mu_L, \quad \mu_p = \Big(1 - \frac{\lambda_2}{\lambda_1}\Big)\mu_L. \tag{2.5.18}$$

The stress can then be decomposed into the solvent and polymeric contributions, giving

$$\boldsymbol{T}^* = 2\mu_s\dot{\boldsymbol{\gamma}}^* + \boldsymbol{\tau}^*, \tag{2.5.19}$$

where $\boldsymbol{\tau}^*$ is the polymeric contribution given by Maxwell's constitutive equation (2.5.10),

$$\boldsymbol{\tau}^* + \lambda_1\frac{D\boldsymbol{\tau}^*}{Dt^*} = 2\mu_p\dot{\boldsymbol{\gamma}}^*. \tag{2.5.20}$$

Hence, for irrotational flow

$$T^*_{nn} = 2\mu_s\frac{\partial^2\phi^*}{\partial n^2} + \tau^*_{nn}, \tag{2.5.21}$$

with

$$\tau^*_{nn} + \lambda_1\frac{D\tau^*_{nn}}{Dt^*} = 2\mu_p\frac{\partial^2\phi^*}{\partial n^2}. \tag{2.5.22}$$

Nondimensionalising once again, and introducing the compensation constant, C,

$$T_{nn} = \frac{2\beta(1+C)}{Re}\frac{\partial^2\phi}{\partial n^2} + \tau_{nn}, \tag{2.5.23}$$

$$\tau_{nn} + De\frac{D\tau_{nn}}{Dt} = \frac{2(1-\beta)(1+C))}{Re}\frac{\partial^2\phi}{\partial n^2}. \tag{2.5.24}$$

where β is a ratio between the solvent and total viscosity given by

$$\beta = \frac{\mu_s}{\mu_s + \mu_p}. \tag{2.5.25}$$

Note that, as β tends to zero, i.e. the solvent contribution of the fluid becomes negligible, the Jeffrey's model approaches the Maxwell model. Furthermore, as β tends to one, and the fluid has only a solvent contribution, the model approaches the Newtonian model. Also, observe that as the Deborah number tends to zero, the model once again approaches the Newtonian case as the relaxation time of the fluid becomes instantaneous.

CHAPTER 3

NUMERICAL MODEL

The boundary integral method can be implemented to model potential flow theory as no additional stress is contributed from the bulk as the flow is inertia dominated being irrotational and inviscid. Hence, all equations exist only on the boundary itself. Since, the viscoelastic effects appear only in the thin boundary layer around the bubble's free surface, which remains approximately irrotational, the viscoelastic effects only appear through an additional boundary equation. Therefore, the boundary integral method can be extended to also include viscoelastic effects in a similar manner to the viscous Newtonian model, for any boundary equation which also satisfies Bernoulli's equation, such as Maxwell's constitutive equation and Jeffrey's constitutive equation.

In this chapter, the boundary integral method is introduced and the numerical method is developed for computationally simulating the evolution of a microbubble using potential flow theory. Detailed descriptions are given on the surface discretization, the boundary integral method along with it's advantages and disadvantages, numerical integration for the normal stress tensor, Lagrangian time integration, and three-dimensional mesh smoothing.

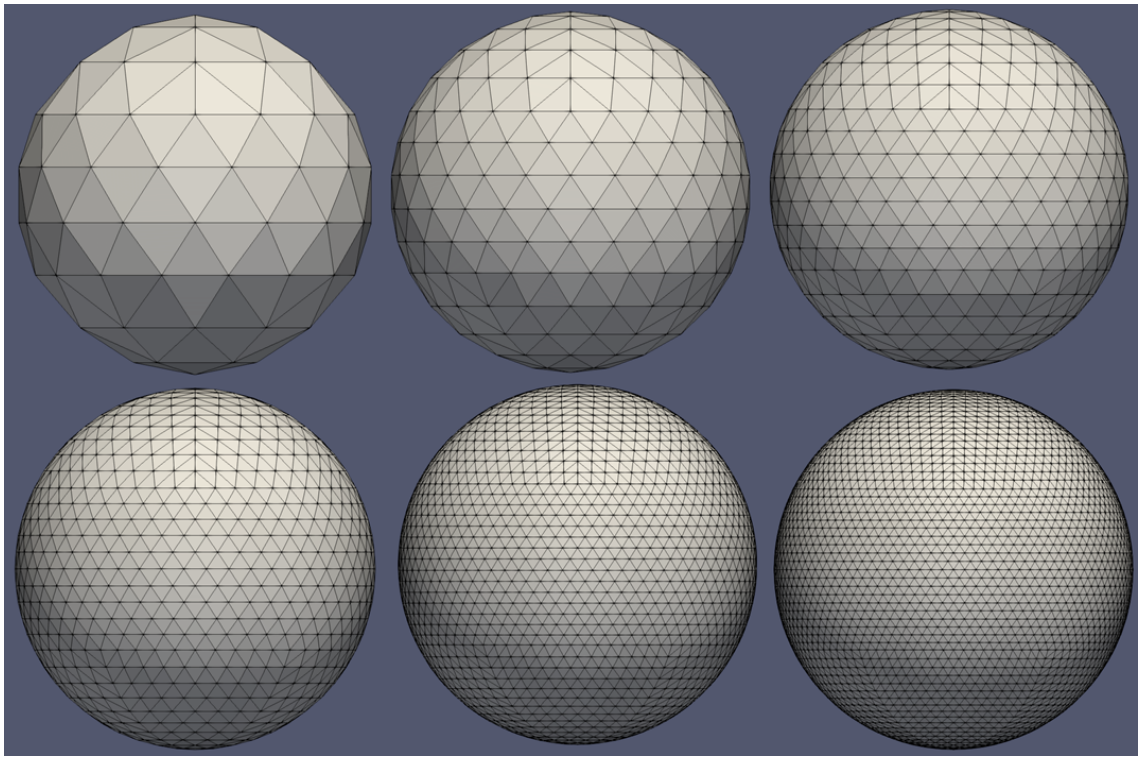


Figure 3.1: A schematic representation of increasing mesh levels to approximate the surface of a bubble, with the top left representing a level 3 mesh, and the bottom right representing a level 20 mesh. As shown, the increased mesh level better approximates the surface of a sphere but it more computationally demanding.

3.1 Interpolation of the surface

To begin modelling the bubble numerically, we first generate an initial mesh to approximate the bubble surface. The first approximation is given by a icosahedron, which consists of 20 equal-sized triangles and 12 nodes situated on the bubble surface. The mesh is then improved by dividing each triangle into 4 smaller triangles, with new nodes introduced at the midpoint of each line segment and projected onto the surface of a sphere. The number of divisions defines the level of the mesh, where each new level better approximates the original shape of the bubble with each new level becoming more computationally demanding. A schematic of this can be found in Figure 3.1. The development of this mesh can be found in Wang [1998].

Once the bubble surface is discretized, Greens second identity, (2.3.3) can be written as the sum of the integration over all the boundary elements, i.e

$$c(\boldsymbol{r},t)\phi_i = \sum_{j=1}^{N}\int_{S_j}\frac{\partial\phi_j}{\partial n}G(\boldsymbol{r},\boldsymbol{q})dS - \sum_{j=1}^{N}\int_{S_j}\phi_j\frac{\partial G(\boldsymbol{r},\boldsymbol{q})}{\partial n}dS. \tag{3.1.1}$$

Considering an arbitrary triangular element, ABC, we introduce a normalised coordinate system (ξ,η), where the three vertices A, B and C of the triangular element are located at $(1,0)$, $(0,1)$ and $(0,0)$ respectively. On each element, the field point $\boldsymbol{r}$, velocity potential ϕ, and normal velocity $\partial\phi/\partial n$, are linearly interpolated using

$$\boldsymbol{r} = (1-\xi-\eta)\boldsymbol{r}_A + \xi\boldsymbol{r}_B + \eta\boldsymbol{r}_C, \tag{3.1.2}$$

$$\phi = (1-\xi-\eta)\phi_A + \xi\phi_B + \eta\phi_C, \tag{3.1.3}$$

$$\frac{\partial\phi}{\partial n} = (1-\xi-\eta)\frac{\partial\phi_A}{\partial n} + \xi\frac{\partial\phi_B}{\partial n} + \eta\frac{\partial\phi_C}{\partial n}, \tag{3.1.4}$$

where the subscripts, A, B, and C, represent the corresponding node on the triangle. Hence, using equation (3.1.4), the first integration in equation (3.1.1) can then be expressed as

$$A = \int_{S_j}\frac{\partial\phi_j}{\partial n}G(\boldsymbol{r},\boldsymbol{q})dS = \frac{\partial\phi_A}{\partial n}A_1 + \frac{\partial\phi_B}{\partial n}A_2 + \frac{\partial\phi_C}{\partial n}A_3, \tag{3.1.5}$$

with

$$A_i = \int_0^1\int_0^{1-\eta}\frac{f_i(\xi,\eta)Jd\xi d\eta}{\sqrt{c_1\xi^2 + c_2\eta^2 + c_3\xi\eta + c_4\xi + c_5\eta + c_6}}, \text{ for } i = 1,2,3, \tag{3.1.6}$$

where J is the Jacobian of the transformation given by

$$J = \Big|\frac{\partial\boldsymbol{r}}{\partial\xi}\times\frac{\partial\boldsymbol{r}}{\partial\eta}\Big| = |(\boldsymbol{r}_B - \boldsymbol{r}_A)\times(\boldsymbol{r}_C - \boldsymbol{r}_A)|, \tag{3.1.7}$$

and

$$f_1(\xi,\eta) = 1-\xi-\eta, \quad f_2(\xi,\eta) = \xi, \quad f_3(\xi,\eta) = \eta, \tag{3.1.8}$$

$$c_1 = |\boldsymbol{r}_A - \boldsymbol{r}_B|^2, \quad c_2 = |\boldsymbol{r}_A - \boldsymbol{r}_C|^2, \quad c_3 = 2(\boldsymbol{r}_A - \boldsymbol{r}_B) \cdot (\boldsymbol{r}_A - \boldsymbol{r}_C),$$
$$c_4 = 2(\boldsymbol{r}_A - \boldsymbol{r}_B) \cdot (\boldsymbol{r}_p - \boldsymbol{r}_A), \quad c_5 = 2(\boldsymbol{r}_A - \boldsymbol{r}_C) \cdot (\boldsymbol{r}_p - \boldsymbol{r}_A), \quad c_6 = |\boldsymbol{r}_p - \boldsymbol{r}_A|^2. \tag{3.1.9}$$

Similarly, the second integral in equation (3.1.1) can be expressed as

$$B = \int_{S_j} \phi_j \frac{\partial G(\boldsymbol{r}, \boldsymbol{q})}{\partial n} dS = \phi_A B_1 + \phi_B B_2 + \phi_C B_3, \tag{3.1.10}$$

with

$$B_i = \int_0^1 \int_0^{1-\eta} \frac{f_i(\xi, \eta) J r_n d\xi d\eta}{(c_1\xi^2 + c_2\eta^2 + c_3\xi\eta + c_4\xi + c_5\eta + c_6)^{3/2}}, \text{ for } i = 1, 2, 3, \tag{3.1.11}$$

where $r_n = \boldsymbol{n} \cdot (\boldsymbol{r}_p - \boldsymbol{r}_A)$.

Once discretizing the surface and preforming the integration over every node point, equation (3.1.1) can be written as the matrix equation,

$$\boldsymbol{H}\boldsymbol{X} = \boldsymbol{G}\boldsymbol{Y}, \tag{3.1.12}$$

with

$$\boldsymbol{H} = \begin{cases} A_i & \text{if the vertex is on } S_B, \\ -B_i & \text{if the vertex is on } S_R, \end{cases} \tag{3.1.13}$$

$$\boldsymbol{G} = \begin{cases} B_i & \text{if the vertex is on } S_B, \\ -A_i & \text{if the vertex is on } S_R, \end{cases} \tag{3.1.14}$$

where

$$\boldsymbol{X} = \begin{cases} \frac{\partial \phi_i}{\partial n} & \text{if the vertex is on } S_B, \\ \phi_i & \text{if the vertex is on } S_R, \end{cases} \tag{3.1.15}$$

is to computed and

$$\boldsymbol{Y} = \begin{cases} \phi_i & \text{if the vertex is on } S_B, \\ \frac{\partial \phi_i}{\partial n} & \text{if the vertex is on } S_R, \end{cases} \tag{3.1.16}$$

is known. Note that solving the above matrix equation is the most computationally demanding process of the boundary integral method. Now, the first stage of the boundary integral method can be implemented.

The BIM is grid-free in the flow domain making it computationally efficient, thus the approach has been used extensively in many bubble dynamics simulations. At each time step, the bubble surface and potential distribution on the surface are known. An advanced, built-in Linear Algebra Package (LAPACK) is used to solve the linear system (3.1.12) with a seven-point Gaussian quadrature being used to integrate the off-diagonal elements of the matrix of coefficients. The weak singularities that occur in equation (3.1.1) are dealt with via the change to polar coordinates (Li et al. [2012b], Wilkerson [1990]). The remaining singularities are eliminated by adopting a 4π rule (Wang [2005]), where for

$$B_{ij} = \sum_{m=1}^{M} \sum_{k=1}^{3} \delta_{kj} B_i, \tag{3.1.17}$$

we have

$$B_{ii} = 4\pi - \sum_{j=1 i \neq j}^{N} B_{ij}. \tag{3.1.18}$$

The solid angle $c(\boldsymbol{r}, t)$ can be approximated, from spherical triangle theory, using

$$c(\boldsymbol{r}, t) = \sum_{1}^{N_b} \delta_i + (2 - N_b)\pi, \tag{3.1.19}$$

where N_b is the number of neighbouring nodes and δ_i is the angle between every two connected nodes.

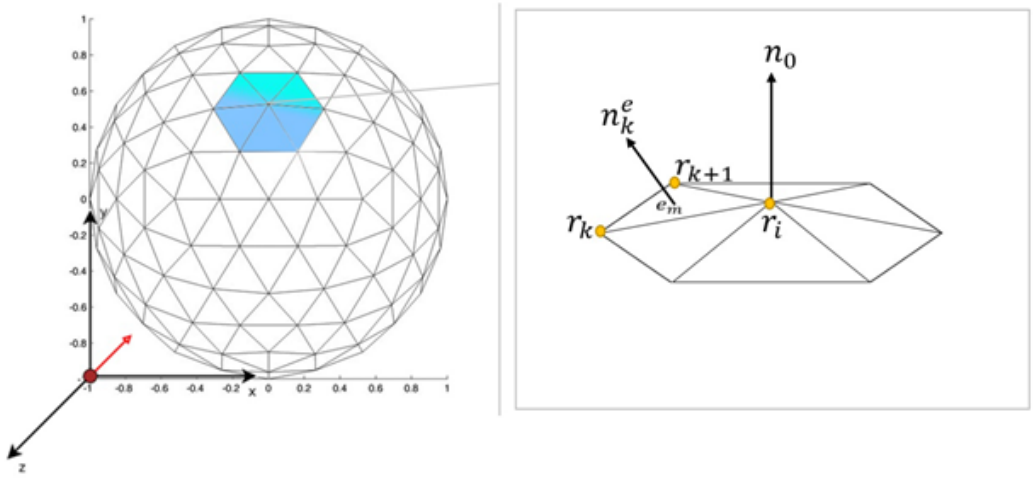


Figure 3.2: A schematic depicting the unit normal and its surrounding nodes at a given node point (Mahmud [2017]). The normal at a node can be approximated using the surrounding normals of the mesh elements.

3.2 Normal vector, mean curvature, tangential velocity, and bubble centroid calculations

The calculation of the normal is of the upmost importance for the viscoelastic models as it is used to calculate the normal stress, T_{nn}. However, at some node $\boldsymbol{r}_i$, the normal $\boldsymbol{n}_0$ can not be calculated due to the discontinuity of the mesh at the node. Hence, the normal, $\boldsymbol{n}_0$, is approximated using a weighted sum of the unit normals, $\boldsymbol{n}_k^e$, of the surrounding segments, centred at $\boldsymbol{r}_k^e$. Hence,

$$\boldsymbol{n}_0 = \sum_{k=1}^{M_s} w_k \boldsymbol{n}_k^e, \tag{3.2.1}$$

where M_s is the amount of triangular segments surrounding the node $\boldsymbol{r}_i$ and w_k is the weighted coefficients which should decrease with the distance between $\boldsymbol{r}_0$ and $\boldsymbol{r}_k^e$. Therefore, w_k can be taken as

$$w_k = \exp\left(\frac{-|\boldsymbol{r}_k^e - \boldsymbol{r}_i|}{2d}\right), \tag{3.2.2}$$

with d being the average distance from the surrounding nodes to $\boldsymbol{r}_i$ (Wang [2005]).

Once the normal has been approximated, the bubble surface can now be interpolated using a moving least square method, by adopting a local Cartesian coordinate system, $0 - XYZ$, with the origin placed at the node $\boldsymbol{r}_0$, and the *Z-axis* in the direction of the unit normal, $\boldsymbol{n}_0$, as estimated by equation (3.2.1) (Han et al. [2016], Zhang et al. [2001]). Hence, using a second order polynomial interpolation, the bubble surface can be expressed as

$$Z = F(X, Y) = a_1 + a_2 X + a_3 Y + a_4 XY + a_5 X^2 + a_6 Y^2, \tag{3.2.3}$$

and

$$f(X, Y, Z) = F(X, Y) - Z = a_1 + a_2 X + a_3 Y + a_4 XY + a_5 X^2 + a_6 Y^2 - Z. \tag{3.2.4}$$

Here, the coefficients, a_i, for $i = 1, 2, ..., 6$, are determined via a weighted moving least square method with error function

$$\sigma(a_1, a_2, ..., a_6) = \sum_{k=1}^{N_B} w_k [F(X_k, Y_k) - Z_k]^2, \tag{3.2.5}$$

where the coordinates (X_k, Y_k, Z_k) represent the coordinates of the surrounding nodes. The derivatives of the error function, σ, with respect to a_j are set to zero, that is,

$$\frac{\partial \sigma}{\partial a_j} = 0, \text{ for } j = 1, 2, ..., 6, \tag{3.2.6}$$

to minimise the error function, resulting in

$$\frac{\partial \sigma}{\partial a_j} = \frac{\partial}{\partial a_j} \sum_{k=1}^{N_B} w_k [F(X_k, Y_k) - Z_k]^2 = 0. \tag{3.2.7}$$

Hence, we obtain the linear algebraic equations

$$\sum_{j=1}^{6} A_{ij} a_j = B_i \text{ for } i = 1, 2, ..., 6, \tag{3.2.8}$$

with

$$A_{ij} = \sum_{j=1}^{N_b} w_k \beta_{kj} \beta_{kj}, \text{ for } k = 1, 2, ..., N_b, \tag{3.2.9}$$

$$B_i = \sum_{j=1}^{N_b} w_k Z_k \beta_{kj}, \text{ for } k = 1, 2, ..., N_b, \tag{3.2.10}$$

where

$$\begin{aligned} \beta_{k1} = 1, \ \beta_{k2} = X_k, \ \beta_{k3} = Y_k, \ \beta_{k4} = X_k^2, \\ \beta_{k5} = X_k Y_k, \ \beta_{k6} = Y_k^2, \text{ for } k = 1, 2, ..., N_b. \end{aligned} \tag{3.2.11}$$

Once the coefficients, a_i, for $i = 1, 2, ..., 6$, are obtained, a more accurate approximation of the normal at $\boldsymbol{r}_i$ can be given by

$$\boldsymbol{n} = \frac{\nabla f}{|\nabla f|} = \mp \frac{(a_2, a_3, -1)}{\sqrt{1 + a_2^2 + a_3^2}}, \tag{3.2.12}$$

where the sign is determined using $\boldsymbol{n} \cdot \boldsymbol{n}_0 > 0$ (Wang and Manmi [2014]) and f is given by equation (3.2.4). This same scheme is used to interpolate the velocity potential distribution on the bubble surface, where now Z_k is replaced with the potential, ϕ_k, at the node (X_k, Y_k, Z_k). This interpolation is given by

$$\phi(X, Y) = b_1 + b_2 X + b_3 Y + b_4 XY + b_5 X^2 + b_6 Y^2,$$

where,

$$\sum_{j=1}^{6} A_{ij} b_j = B_i \text{ for } i = 1, 2, ..., 6, \tag{3.2.13}$$

with

$$A_{ij} = \sum_{j=1}^{N_b} w_k \beta_{kj} \beta_{kj}, \text{ for } k = 1, 2, ..., N_b, \tag{3.2.14}$$

$$B_i = \sum_{j=1}^{N_b} w_k \phi_k \beta_{kj}, \text{ for } k = 1, 2, ..., N_b. \tag{3.2.15}$$

We are now in a position the calculate the velocity, $\boldsymbol{u}$. This is given in terms of the velocity potential, ϕ, by

$$\boldsymbol{u} = \nabla\phi = \frac{\partial\phi}{\partial n} + \boldsymbol{u}_\tau. \tag{3.2.16}$$

Here, $\boldsymbol{u}_\tau$ is the tangential velocity. The x, y, and z components of the tangential velocity are obtained using the interpolation of the potential and are given by

$$\phi_x = \phi_X \frac{\partial X}{\partial x} + \phi_Y \frac{\partial Y}{\partial x} = b_2 \frac{\partial X}{\partial x} + b_3 \frac{\partial Y}{\partial x}, \tag{3.2.17}$$

$$\phi_y = \phi_X \frac{\partial X}{\partial y} + \phi_Y \frac{\partial Y}{\partial y} = b_2 \frac{\partial X}{\partial y} + b_3 \frac{\partial Y}{\partial y}, \tag{3.2.18}$$

$$\phi_z = \phi_X \frac{\partial X}{\partial z} + \phi_Y \frac{\partial Y}{\partial z} = b_2 \frac{\partial X}{\partial z} + b_3 \frac{\partial Y}{\partial z}, \tag{3.2.19}$$

Hence, the tangential velocity is given by

$$\boldsymbol{u}_\tau = \Big(\frac{\partial}{\partial x}(b_2 X + b_3 Y), \frac{\partial}{\partial y}(b_2 X + b_3 Y), \frac{\partial}{\partial z}(b_2 X + b_3 Y) \Big). \tag{3.2.20}$$

Therefore,

$$\boldsymbol{u}_\tau = b_2 \nabla X(x, y, z) + b_3 \nabla Y(x, y, z), \tag{3.2.21}$$

where we determine $X(x, y, z)$ and $Y(x, y, z)$ from the transformation to the local coordinates (X, Y, Z). With the normal approximated, $\partial^2\phi/\partial n^2$ can be calculated using

$$\frac{\partial^2\phi}{\partial n^2} = n_x \phi_x + n_y \phi_y + n_z \phi_z, \tag{3.2.22}$$

where n_x, n_y, and n_z are the components of $\boldsymbol{n}$. This is then used to calculate the viscous and viscoelastic terms for T_{nn}.

3.3 Lagrangian integration with time

The normal stress tensor, T_{nn}, is now obtained using a backward Euler approximation for Maxwell's constitutive equation (2.5.14). This is given by,

$$De\Big(\frac{T_{nn}(x(t),t) - T_{nn}(x(t-\Delta t),t-\Delta t)}{\Delta t}\Big) + T_{nn}(x(t),t) = \frac{2(1+C)}{Re}\frac{\partial^2\phi(x(t),t)}{\partial n^2}, \tag{3.3.1}$$

and so

$$T_{nn}(x(t),t) = \frac{De}{\Delta t + De}T_{nn}(x(t-\Delta t),t-\Delta t) + \frac{2\Delta t(1+C)}{Re(\Delta t + De)}\frac{\partial^2\phi(x(t),t)}{\partial n^2}. \tag{3.3.2}$$

A backwards Euler method is used as the material time derivative has collapsed down to a first-order time derivative as described in Chapter (2). Hence, a backward Euler-method can accurately integrate the boundary equation without creating considerable instabilities at collapse, and without increasing CPU time like more advanced, high-order numerical integration techniques.

Similarly for the Jeffrey's model, Jeffrey's constitutive equation (2.5.24) can be calculated using

$$\tau_{nn}(x(t),t) = \frac{De}{\Delta t + De}\tau_{nn}(x(t-\Delta t),t-\Delta t) + \frac{2\Delta t(1+C)(1-\beta)}{Re(\Delta t + De)}\frac{\partial^2\phi(x(t),t)}{\partial n^2}. \tag{3.3.3}$$

and so the normal stress tensor, T_{nn}, at each time-step is given by

$$T_{nn}(x(t),t) = \frac{2\beta(1+C)}{Re}\frac{\partial^2\phi(x(t),t)}{\partial n} + \tau(x(t),t). \tag{3.3.4}$$

The varied time-step is chosen as

$$\Delta t = \frac{\Delta\phi}{\boldsymbol{max}|1 + \frac{1}{2}|\nabla\phi|^2 - \delta^2 z - \varepsilon(\frac{V_0}{V})^{\xi} + \frac{2\kappa}{We} - T_{nn}|}, \tag{3.3.5}$$

for some constant $\Delta\phi$ found experimentally. This is such that the time-step decreases

as the velocity, $\nabla\phi$, increases, such as when the jet starts to form. The mean curvature, κ, is given by

$$\kappa = \frac{\nabla f \ \mathrm{H}(f) \nabla f^T - |\nabla f|^2 \ \mathrm{Trace}(\mathrm{H}(f))}{2|\nabla f|^3}, \tag{3.3.6}$$

where $H(f)$ is the Hessian. This gives

$$\kappa = -\frac{a_5 + a_6 + a_6 a_2^2 + a_5 a_3^2 - a_2 a_3 a_4}{(1 + a_2^2 + a_3^2)^{3/2}}. \tag{3.3.7}$$

Therefore, the new bubble surface and potential distribution at the next time step, $t + \Delta t$, can be obtained by integrating the kinematic boundary condition (2.3.4) and the dynamic boundary condition (2.3.5), which is computed using a fourth-order Runge-Kutta scheme as it provides greater stability over the collapsing of the bubble. When tried with lower order schemes, significant numerical instabilities could arise resulting in 'splintering' on the bubble mesh and inaccurate bubble profiles.

3.4 Calculation of Kelvin impulse

The Kelvin impulse, having the dimensions of momentum, corresponds to the apparent inertia of the cavitation bubble (Blake [1988]). The direction of the Kelvin impulse can be calculated and provides a good estimation for the migration of the bubble once a jet is formed (Best and Blake [1994]). The Kelvin Impulse of a cavity is defined as

$$\boldsymbol{I}(t) = \oint_s \phi \boldsymbol{n} dS, \tag{3.4.1}$$

where $\boldsymbol{I}(t)$ changes in response to the action of forces according to

$$\frac{d\boldsymbol{I}(t)}{dt} = \boldsymbol{F}(t), \tag{3.4.2}$$

where $\boldsymbol{F}(t)$ is the Bjerknes force defined via Newton's second law of motion

$$\boldsymbol{F}(t) = m\frac{d\boldsymbol{u}}{dt}. \tag{3.4.3}$$

Hence,

$$\boldsymbol{F}(t) = \frac{d}{dt}\oint_s \phi \boldsymbol{n} dS. \tag{3.4.4}$$

Integrating with respect to time, and setting $\boldsymbol{I}(0) = 0$, we obtain an expression for the Kelvin impulse given by

$$\boldsymbol{I}(t) = \int_0^t \boldsymbol{F}(t')dt'. \tag{3.4.5}$$

Note that the potential ϕ, can be expressed in the form

$$\phi(\boldsymbol{r}, t) = \frac{-m(t)}{4\pi}\frac{1}{|\boldsymbol{r} - \boldsymbol{q}|} + \psi(\boldsymbol{r}, t). \tag{3.4.6}$$

where ψ is the potential contribution from the image points. Using the divergence theorem on equation (3.4.4) and taking the time derivative inside the integral, the Bjerknes force, $\boldsymbol{F}(t)$, can be expressed (Best and Blake [1994]) by

$$\boldsymbol{F}(t) = -m(t)\nabla\psi(\boldsymbol{r}, t). \tag{3.4.7}$$

where $-m(t) = dV/dt$ is the volume flux of the spherical bubble. Hence, provided we can find an appropriate expression for the velocity potential, we can determine an expression for the Kelvin impulse on the bubble and then estimate the direction of the bubble migration.

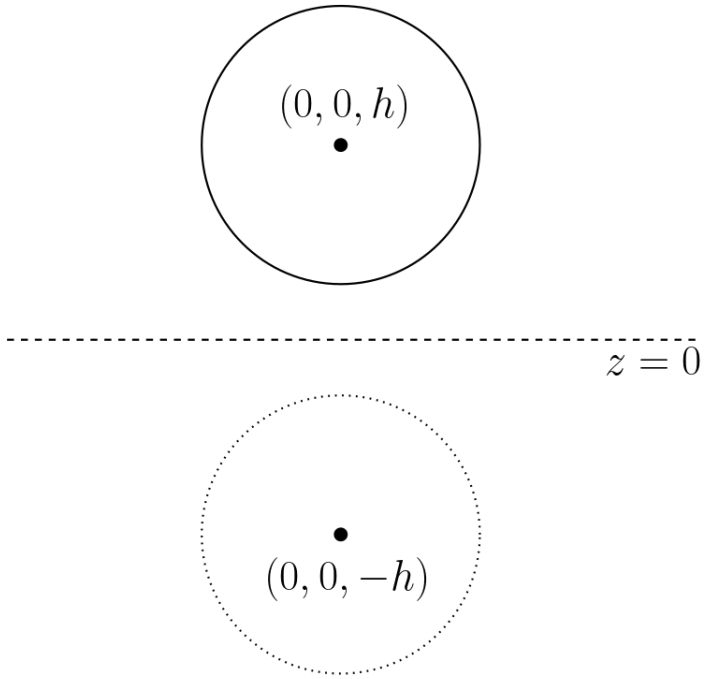


Figure 3.3: A schematic representation of the method of images for a bubble near a rigid boundary. The wall is simulated by introducing a image bubble symmetrically below the wall.

3.4.1 Kelvin impulse near a flat rigid boundary

Consider a bubble with centre located at $(0, 0, h)$ with a rigid boundary located at $z = 0$. In this case, the potential can be expressed as

$$\phi(\boldsymbol{r}, t) = \frac{-m(t)}{4\pi}\left(\frac{1}{(x^2 + y^2 + (z-h)^2)^{1/2}} + \frac{1}{(x^2 + y^2 + (z+h)^2)^{1/2}}\right). \tag{3.4.8}$$

Here, a method of images has been used with an image bubble situate with centre at $(0, 0, -h)$ to model the effects of the rigid wall. This is shown in Figure 3.3. Therefore,

$$\psi(\boldsymbol{r}, t) = \frac{-m(t)}{4\pi}\left(\frac{1}{(x^2 + y^2 + (z+h)^2)^{1/2}}\right). \tag{3.4.9}$$

Hence, using equation (3.4.7), we have that

$$\boldsymbol{F}(t) = -m(t)\nabla\left(\frac{-m(t)}{4\pi}\frac{1}{(x^2 + y^2 + (z+h)^2)^{1/2}}\right)\Bigg|_{(0,0,h)=\boldsymbol{r}_s}, \tag{3.4.10}$$

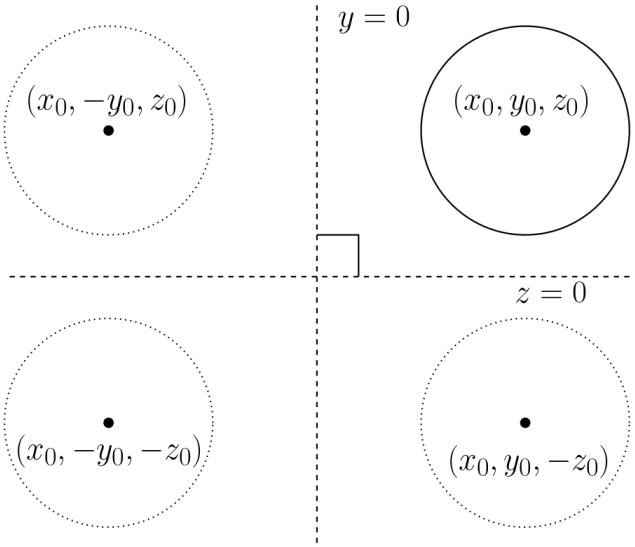


Figure 3.4: A schematic representation of the method of images for a bubble at a corner of angle $\alpha = \pi/2$. Four different image bubbles are introduced to simulate the interaction with the two rigid boundaries. In doing so, the BIM must be solved four times at each time-step.

$$= \frac{m(t)^2}{4\pi} \frac{\partial}{\partial z} \left(\frac{1}{(x^2 + y^2 + (z+h)^2)^{1/2}} \right) \Bigg|_{(0,0,h)=\boldsymbol{r}_s} \boldsymbol{k}. \tag{3.4.11}$$

Therefore, computing the derivative,

$$\boldsymbol{F}(t) = \frac{m(t)^2}{4\pi} \left[\frac{-(z+h)}{(x^2 + y^2 + (z+h)^2)^{3/2})} \right]_{(0,0,h)=\boldsymbol{r}_s} \boldsymbol{k} = \frac{-m(t)^2}{16\pi h^2} \boldsymbol{k}. \tag{3.4.12}$$

Hence, the Kelvin impulse for a bubble near a rigid boundary is given by

$$\boldsymbol{I}(t) = -\int_0^t \frac{m(t')^2}{16\pi h^2} \boldsymbol{k} dt'. \tag{3.4.13}$$

Observe that, the minus sign implies the Kelvin impulse is directed in the negative z direction and thus provides an estimation for the direction in which the bubble will migrate once a jet is formed.

3.4.2 Kelvin impulse near a corner

For a corner of angle $\alpha = \pi/l$ for some $l \in \mathbb{N}$, a bubble is located and some field point $\boldsymbol{r} = \boldsymbol{q}$. The corner is situated at the point of intersection of two rigid boundaries. This is shown in Figure 3.4 for the case when $l = 2$. For general l, the potential can be represented by

$$\phi(\boldsymbol{r}, t) = \frac{-m(t)}{4\pi}\left(\frac{1}{|\boldsymbol{r} - \boldsymbol{q}|} + \sum_{i=1}^{2l-1} \frac{1}{|\boldsymbol{r} - \boldsymbol{q}_i|}\right), \tag{3.4.14}$$

where $2l - 1$ represents the number of image points needed, and $\boldsymbol{r}_j$ for $j \geq 1$ are obtained from the method of images. Therefore,

$$\psi(\boldsymbol{r}, t) = \frac{-m(t)}{4\pi} \sum_{i=1}^{2l-1} \frac{1}{|\boldsymbol{r} - \boldsymbol{q}_i|}. \tag{3.4.15}$$

Hence, $F(t)$ can then be obtained as

$$\boldsymbol{F}(t) = -m(t)\nabla\psi(\boldsymbol{r}, t) = \frac{m(t)^2}{4\pi} \sum_{i=1}^{2l-1} \nabla\left(\frac{1}{|\boldsymbol{r} - \boldsymbol{q}_i|}\right)\Bigg|_{\boldsymbol{r}=\boldsymbol{q}}, \tag{3.4.16}$$

$$= \frac{m(t)^2}{4\pi} \sum_{i=1}^{2l-1} \frac{\boldsymbol{r} - \boldsymbol{q}_i}{|\boldsymbol{r} - \boldsymbol{q}_i|^3}\Bigg|_{\boldsymbol{r}=\boldsymbol{q}} = \frac{m(t)^2}{4\pi} \sum_{i=1}^{2l-1} \frac{\boldsymbol{q} - \boldsymbol{q}_i}{|\boldsymbol{q} - \boldsymbol{q}_i|^3}. \tag{3.4.17}$$

The Kelvin impulse for a bubble near a corner is therefore given by

$$\boldsymbol{I}(t) = \frac{-1}{4\pi} \int_0^t m(t')^2 \sum_{i=1}^{2l-1} \frac{\boldsymbol{q} - \boldsymbol{q}_i}{|\boldsymbol{q} - \boldsymbol{q}_i|^3} dt'.$$

It is then clear to see that the direction of the jet migration will depend on the location of the bubble centre initially and the position and number of image points.

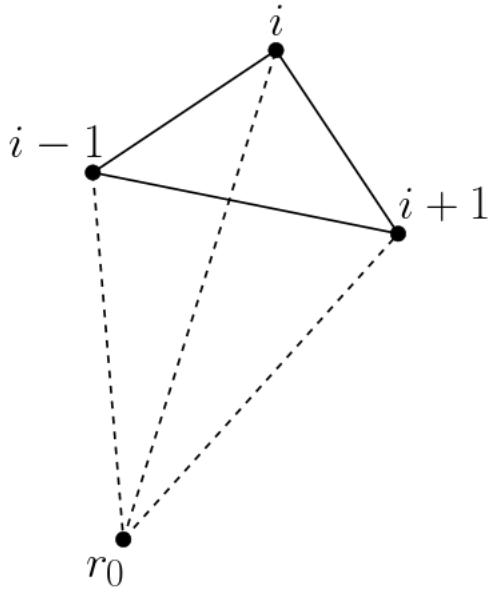


Figure 3.5: A schematic representation of the tetrahedrons created from an internal point in the bubble, $\boldsymbol{r_0}$, and three surface nodes, $i-1$, i, and $i+1$. By creating a tetrahedron from every mesh element, the total volume of the bubble can then be approximated.

3.5 Calculation of bubble volume and bubble centroid

At each time step, the volume of the non-spherical bubble can be calculated by considering each triangular element. By taking a point of origin inside the bubble, $\boldsymbol{r}_0$, and connecting to all nodes on the bubble surface, the bubble volume is then split into a combination of tetrahedrons. An example of this is shown in Figure 3.5, where the origin point is connected to nodes, $i-1$, i, and $i+1$.

Say for each triangular element, the nodes are given by

$$\boldsymbol{r}_0 = (x_0, y_0, z_0), \text{ and } \boldsymbol{r}_k = (x_k, y_k, z_k) \text{ for } k = i-1, i, i+1. \tag{3.5.1}$$

Then the volume of the *ith* tetrahedron is given by

$$6V_i = \begin{vmatrix} x_0 & y_0 & z_0 & 1 \\ x_{i-1} & y_{i-1} & z_{i-1} & 1 \\ x_i & y_i & z_i & 1 \\ x_{i+1} & x_{i+1} & x_{i+1} & 1 \end{vmatrix}, \tag{3.5.2}$$

Hence,

$$6V_i = \begin{vmatrix} x_{i-1} & y_{i-1} & z_{i-1} \\ x_i & y_i & z_i \\ x_{i+1} & y_{i+1} & z_{i+1} \end{vmatrix} - \begin{vmatrix} x_0 & y_0 & z_0 \\ x_i & y_i & z_i \\ x_{i+1} & y_{i+1} & z_{i+1} \end{vmatrix} + \begin{vmatrix} x_0 & y_0 & z_0 \\ x_{i-1} & y_{i-1} & z_{i-1} \\ x_{i+1} & y_{i+1} & z_{i+1} \end{vmatrix} - \begin{vmatrix} x_0 & y_0 & z_0 \\ x_{i-1} & y_{i-1} & z_{i-1} \\ x_i & y_i & z_i \end{vmatrix}. \tag{3.5.3}$$

However, a point must be made for when the bubble is no longer convex. The origin point does not have to lie within the bubble and can therefore be chosen as an exterior point. Applying the same method, tetrahedrons are created by joining this origin to each triangular node. If the nodes are on the opposite side of the bubble surface to the origin point, the volume of the tetrahedron is added. If the triangular element is on the closest side of the bubble surface, then the volume of the tetrahedron is taken away. In doing so, an approximation can then be made for the total volume inside the bubble. This is represented in two dimensions in Figure 3.6. The area of the triangle with nodes 0, i, and $i+1$ will be subtracted from the total area as the nodes are on the side of the surface closest to the origin point. The triangular with nodes given by 0, k, and $k+1$ will be added to the total area as the nodes are on the opposite side of the bubble surface. In doing so, the area which is added to the total is the area of the shape with nodes i, $i+1$, k, and $k+1$. The same concept is applied to three spatial dimensions.

Once the bubble volume is known, the bubble centroid coordinates, $\boldsymbol{\xi}_C$, can be calculated. This is given by

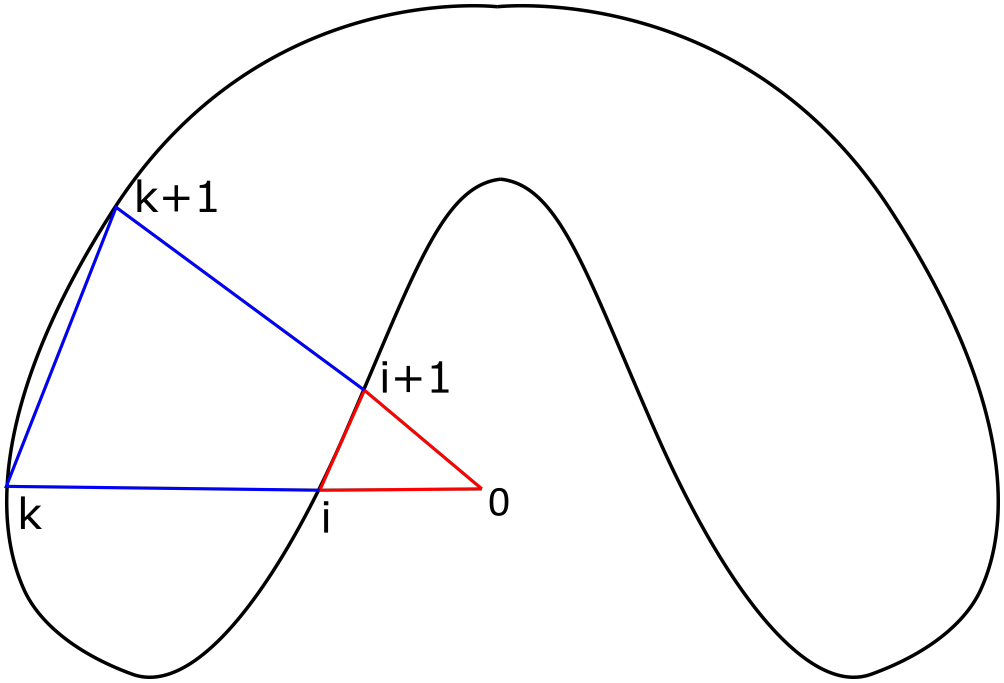


Figure 3.6: A two-dimensional representation of how the addition of triangle $0, k, k+1$ and the subtraction of triangle $0, i, i+1$ gives an approximation of the area $i, i+1, k, k+1$. A similar idea is applied to three dimensions.

$$\boldsymbol{\xi}_C \approx \frac{\sum_{i=1}^{M_T} \boldsymbol{\xi}_k V_k}{\sum_{i=1}^{M_T} V_k}, \tag{3.5.4}$$

where M_T is the total number of tetrahedrons, V_k is the volume of each tetrahedron, and $\boldsymbol{\xi}_k$ is the centroid of the k-th tetrahedron (Mahmud [2017]).

3.6 Elastic mesh technique

Historically, a Lagrangian method has been used to update the nodal positions on the bubble surface using the material velocities. However, when the bubble becomes non-spherical, nodes can bunch up near the end of the bubble jet. This reduces the line segment length in the jet leading to poor mesh quality and numerical instabilities (Wang and Manmi [2014]). Hence, a redistribution of the nodes across the bubble surface is required to ensure a consistently smooth mesh and to reduce numerical instabilities. One such developed technique is the elastic mesh technique.

The elastic mesh technique (EMT) is implemented to optimise the mesh by minimising the total elastic energy stored in each mesh segment. To do this, the tangential velocity, $\boldsymbol{u}_\tau$ in equation (3.2.16), can be approximated by minimising the total elastic energy rather than its approximation in the Lagrangian method given by equation (3.2.21). In doing so, this provides a more stable approximation for the non-spherical bubble surface when a jet begins to form (Wang et al. [2003]). This is due to meshing technique maintaining a minimum line segment length whilst providing enough surface nodes in areas where the surface velocity is greatest.

The total elastic energy, E_{mesh}, stored in the mesh at time $t + \Delta t$ is given by

$$E_{mesh} = \sum_{i=1}^{N} \sum_{j=1}^{M_i} \int_0^{l_{ij}} f_e(l) dl, \tag{3.6.1}$$

where N is the total number of nodes, M_i is the number of nodes surrounding node i, and l_{ij} is the segment length between two nodes $\boldsymbol{r}_i$ and $\boldsymbol{r}_j$ after the time step. Hence, l_{ij} is given by

$$l_{ij} = |(\boldsymbol{r}_i + \boldsymbol{u}_i \Delta t) - (\boldsymbol{r}_j + \boldsymbol{u}_j \Delta t)|, \tag{3.6.2}$$

where $\boldsymbol{u}_i$ and $\boldsymbol{u}_j$ represent the velocities of the corresponding nodes. The elastic force, $f_e(l)$, is taken in this work as

$$f_e(l) = k_e l^3, \tag{3.6.3}$$

where k_e is the coefficient of elasticity. To minimise the elastic energy stored in the mesh, we must have that

$$\frac{\partial E_{mesh}}{\partial \boldsymbol{r}_i} = 0 \text{ for } i = 1, ..., N. \tag{3.6.4}$$

A solution to equation (3.6.4) can be found via an iterative process given by

$$\boldsymbol{u}_i^{n+1} = \frac{\partial \phi}{\partial n_i} + \boldsymbol{u}_{\tau i} = \frac{\partial \phi}{\partial n_i} + P\Big(\frac{\sum_{j=1}^{M_i}(f(l_{ij}^n)(\boldsymbol{r}_j - \boldsymbol{r}_i + \Delta t \boldsymbol{u}_j^n)/l_{ij}^n)}{\Delta t \sum_{j=1}^{M_i} f(l_{ij}^n)/l_{ij}^n}\Big), \tag{3.6.5}$$

where $\boldsymbol{u}_i^n$ is the *n-th* iteration of the prescribed velocity at node i, and P is an operator projecting the vector onto the tangential plane at the *i-th* node (a complete derivation of equation (3.6.5) can be found in Wang et al. [2003]). Upon solving equation (3.6.5), an optimum velocity, $\boldsymbol{u}_i^{emt}$, is found to find the new bubble surface after each time step, allowing for a more stable mesh when a jet begins to form.

Hybrid mesh technique

The EMT technique removes the instabilities caused by the Lagrangian integration. However, for the majority of the bubble oscillation, the bubble remains relatively spherical and so a Lagrangian approach is sufficient in maintaining a smooth surface mesh. Furthermore, if the mesh nodes are redistributed too often, energy and information can be lost regarding the intended updated bubble surface leading to an inaccurate description of the jet. However, at jet formation, the EMT method should be implemented to accurately model the jet profile and reduce numerical errors. To this end, a hybrid method is developed such that the EMT method is only implemented when necessary to reduce CPU time and loss of uniqueness. The hybrid approach is implemented such that

$$\boldsymbol{u}_i^{hybrid} = W\boldsymbol{u}_i + (1-W)\boldsymbol{u}_i^{emt}, \quad W \in [0,1] \tag{3.6.6}$$

where W represents some weight which is found experimentally, and differs for each bubble simulation. The weight, W, is used to determine how often the Lagrangian method should be used compared to the EMT method. The weight is chosen by testing the BIM code with the required simulation and determining at which stages and how often smoothing is required, and placing those conditions in the BIM

code. This hybrid approach leads to a finer and smoother mesh surface than the EMT method alone whilst reducing CPU time and maintaining an accurate bubble profile.

CHAPTER 4

NUMERICAL SIMULATIONS OF THE MAXWELL MODEL

In this chapter, the numerical model established in Chapter 3 is implemented to analyse the effect of the Deborah number on a three-dimensional bubble. The boundary integral method is firstly used to simulate the evolution of a bubble in various infinite Maxwell fluids and is validated using comparisons between the BIM code and the Rayleigh-Plesset model for spherical bubbles in an infinite Maxwell fluid. Results are then presented on the bubble radius history and average velocity over the bubble surface as a result of an increase in the relaxation time of the fluid.

Furthermore, a flat rigid boundary is introduced below the microbubble and results are presented on the bubble centroid migration, Kelvin impulse and jet shape at collapse in different viscoelastic fluids. A second wall is then introduced to simulate the three-dimensional effects on the bubble of a viscoelastic fluid near a corner. The simulations are validated by comparison with experimental data for a corner of angle $\alpha = \pi/2$ and $\alpha = \pi/4$. Results are given on the three-dimensional effects of the Deborah number on the jet shape, bubble centroid migration and jetting angle. Also, results are given on the effects of reducing the fluid domain by changing the corner angle.

Finally, the large-scale effects of the Deborah number and Reynolds number are analysed on all investigated properties of the bubble.

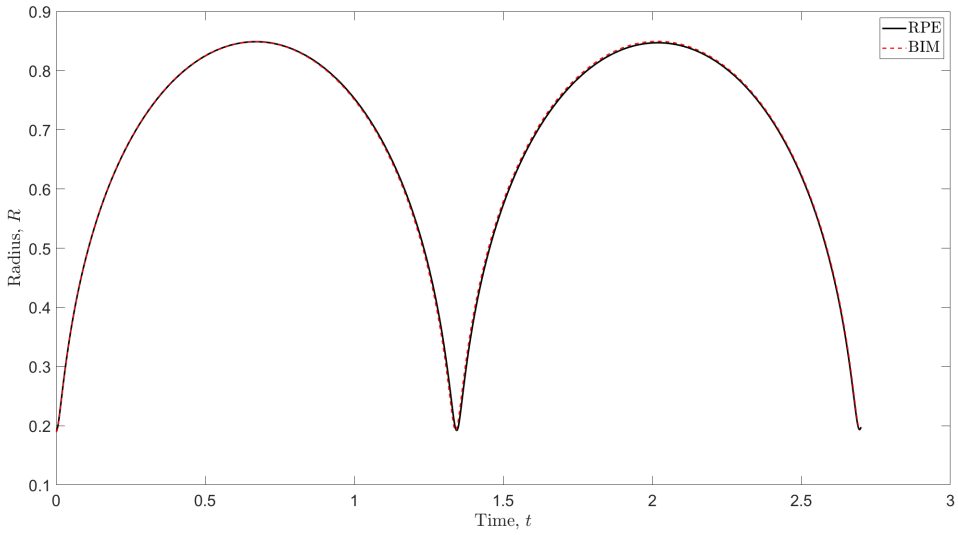


Figure 4.1: The comparison of the radius history of a spherical bubble in a Maxwell fluid with $De = 2.0$, between the non-Newtonian Rayleigh-Plesset equation (2.3.6) and the BIM code. The parameters of the bubble and the surrounding liquid are $\zeta = 1.667$, $\sigma = 0.073 Nm^{-1}$, $P_0 = 101.3 kPa$, $P_v = 0.023 P_0$ and $\rho = 999 kgm^{-3}$.

4.1 Infinite fluid

Firstly, we look at the effect of the relaxation time of the fluid on a bubble in a infinite domain.

4.1.1 Validation of radius history with Rayleigh-Plesset equation

To validate the boundary integral method for the Maxwell model, we compare the radius history of the BIM code for a Maxwell fluid, to the radius history given by the non-Newtonian Rayleigh-Plesset equation (2.3.6). We initiate a bubble in an infinite fluid with an initial radius of $R_0^* = 4.5 \mu m$. A level 10 mesh is used with the parameters of the gas and liquid given by $\xi = 1.667$, $\sigma = 0.073 Nm^{-1}$, $P_0 = 101.3 kPa$, $P_v = 0.023 P_0$ and $\rho = 999 kgm^{-3}$. The pressure difference is set to $\varepsilon = 100$. The simulation is then repeated for a Maxwell fluid with Deborah numbers $De = 0.0$, 0.2, 2.0 and 20.0. The results for $De = 2.0$ are found in Figure 4.1 whilst the remaining results are found in Appendix A.1 in Figures A.4, A.5, and A.6.

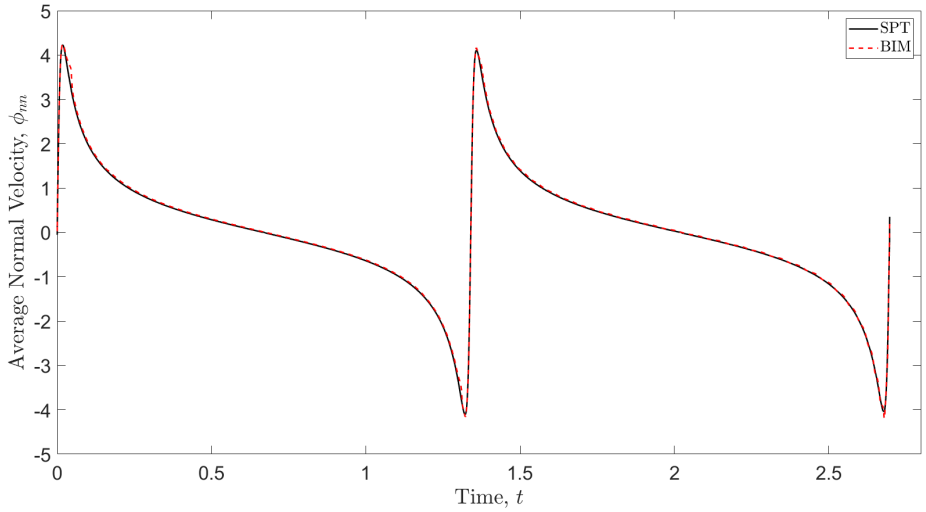


Figure 4.2: The comparison of ϕ_{nn} for a spherical bubble in a Maxwell fluid with $De = 2.0$, between spherical bubble theory (2.2.17) and the BIM code with the remaining parameters being the same as in Figure 4.1.

Figure 4.1 represents the radius history for a bubble in a fluid of Deborah number, $De = 2.0$, as calculated both by the BIM three-dimensional code (black line) and the analytical solution the the Rayleigh-Plesset equation (2.3.6) (red line). As shown, both the analytical solution to the Rayleigh-Plesset equation and the numerical solution provided by the BIM code are in strong agreement with each other over the entirety of the first two oscillations for the Maxwell model. Therefore, given the strong agreement between the two curves, the BIM can be implemented throughout the simulations in this thesis for a Maxwell fluid.

4.1.2 Validation of potential calculation with spherical bubble theory

For a spherical bubble, the calculation of ϕ_{nn} using the BIM method can be verified using the average value of the velocity on the surface via equation (2.2.17).

Thus, to validate the calculation of ϕ_{nn}, we run the BIM code for a bubble in an infinite fluid using the same parameters as in section 4.1.1 and take an average value of ϕ_{nn} over the bubble surface to reduce the effect of localised errors. The results

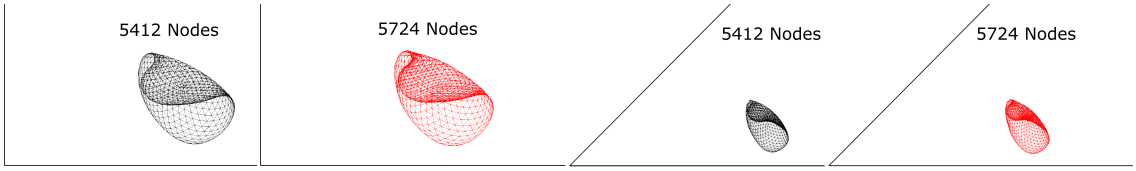


Figure 4.3: The jet profiles and location of a bubble initiated with 5412 nodes and 5724 nodes for angles, $\alpha = \pi/2$ and $\pi/4$ with the remaining parameters being the same as in Figure 4.1.

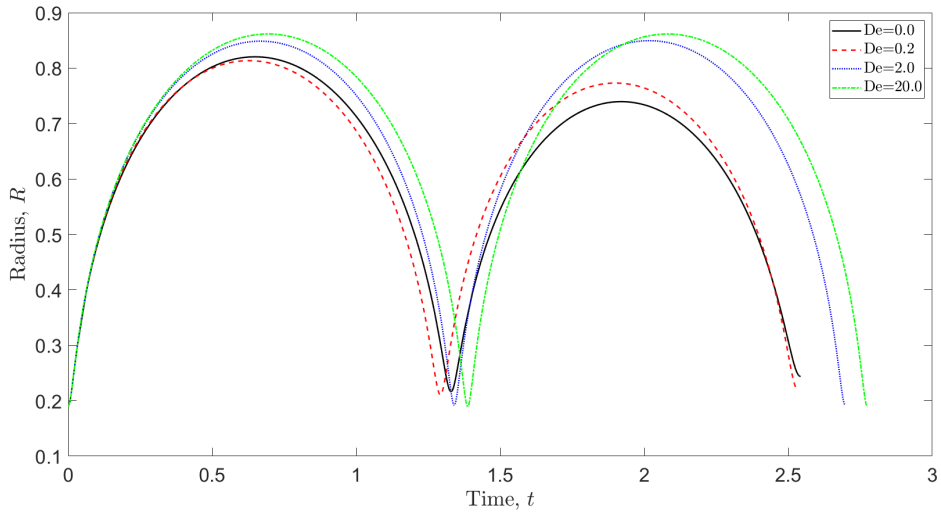


Figure 4.4: The influence of the Deborah number on the radius history a bubble in an infinite Maxwell fluid with $De = 0.0$, 0.2, 2.0, and 20.0. The remaining parameters of the fluid are the same as in Figure 4.1.

for $De = 2.0$ are shown in Figure 4.2. In the figure, the black solid line represents the potential history over the first two oscillations as found analytically by equation (2.2.17), where the red dotted line represents the potential history as computed by the BIM code.

As shown, there is a strong agreement between the BIM code and the spherical bubble theoretical solution for ϕ_{nn} over the first two oscillations. The calculations for the remaining values of De are shown in Appendix A.1 in Figures A.1, A.2, and A.3, for $De = 0.0$, 0.2, and 20.0, respectively. There is however, slight numerical error around the turning points for the lower values of De, but for only a very brief amount of time. Therefore, we can conclude that the viscous calculations made by the boundary integral method are adequate enough to accurately model the

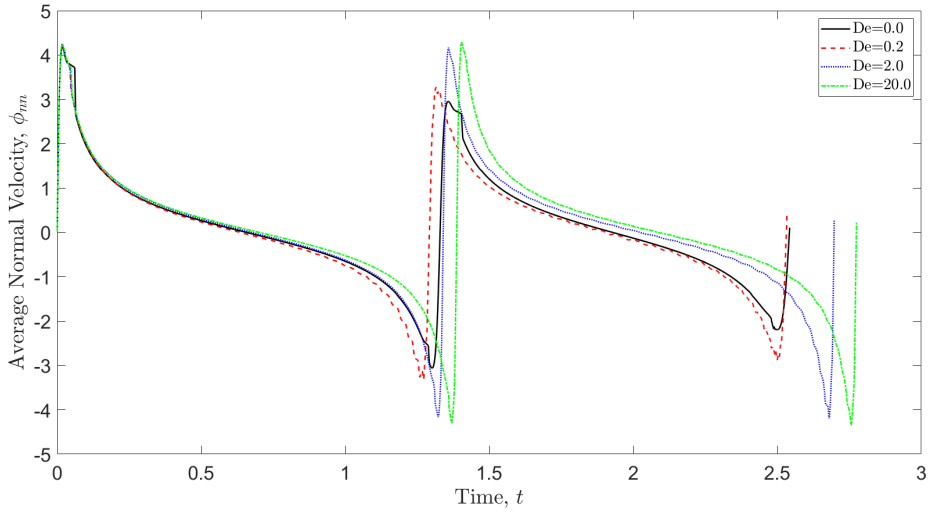


Figure 4.5: The influence of the Deborah number, De, on the average velocity of a bubble in an infinite Maxwell fluid. The parameters of the surrounding liquid are the same as in Figure 4.1.

viscoelastic effects of a non-Newtonian fluid.

4.1.3 Convergence test

To analyse the convergence of the BIM model, convergence tests were conducted for a bubble near a corner of angles $\alpha = \pi/2$ and $\pi/4$ with the remaining parameters being the same as in Figure 4.1. The jet profiles at collapse are shown in Figure 4.3 for number of elements $M = 5412$ and $M = 5724$ which corresponds to a level 10 mesh and a level 11 mesh, respectively. Note that the convergence test was also done for a level 8 and level 9 mesh. However, Figure 4.3 only shows the mesh levels which results in no significant changes in the bubble profile whist still accurately predicting the bubble profile at collapse.

As the mesh level increases, the minimum line segment decreases and so interpolates the bubble surface more accurately. However, in doing so the CPU time drastically increases and so we aim to keep the mesh density low whilst still providing accurate results. A smaller line segment can also result in numerical instabilities as the nodes get congested in the jet profile or the line segment length approaches a

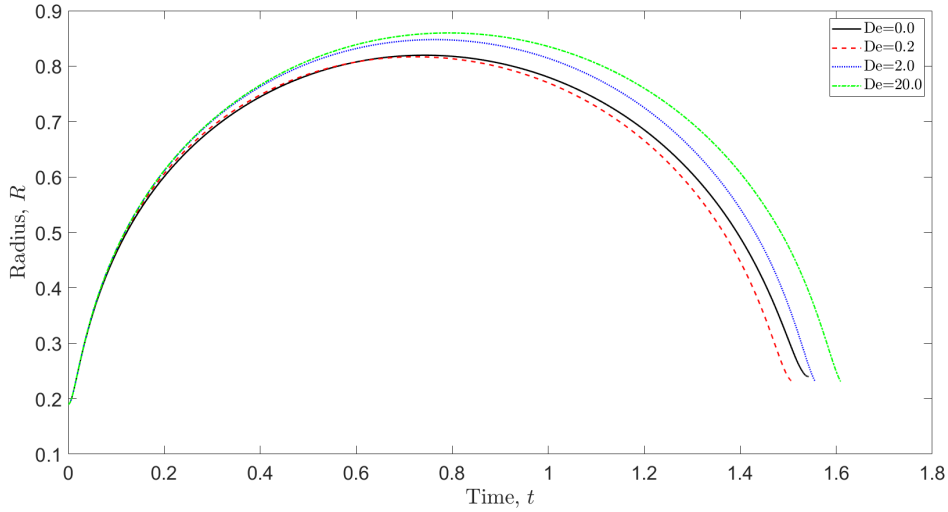


Figure 4.6: The influence of the Deborah number, De, on the radius history of a bubble near a wall with stand-off distance, $\gamma = 1.0$ in a Maxwell fluid. The parameters of the surrounding liquid are the same as in Figure 4.1.

similar order to the time-step. Hence, we choose the lowest level of mesh for which a further increase in mesh density results in no significant change in bubble profile.

As shown, the jet profiles are in excellent agreement for both mesh levels and values of M with $\alpha = \pi/2$ and $\alpha = \pi/4$. As such, since a level 10 mesh is the lowest mesh level for which the bubble profile does not change with an increase to a higher mesh level, all the remaining calculations in this study are performed for a level 10 mesh with $M = 5412$.

4.1.4 Results for an infinite fluid

Firstly, we consider the evolution of a microbubble in an infinite fluid. The parameters of the bubble and the surrounding fluid are the same as for Section 4.1.1. We consider the effect of the Deborah number on the radius history of the bubble. The radius of the bubble over the first two oscillations for $De = 0.0$, 0.2, 2.0, and 20.0 is given by Figure 4.4.

As shown, a small increase in the Deborah number to $De = 0.2$ from the initial Newtonian case $De = 0.0$, results in a slight decrease in the time taken for the bubble

to expand and collapse over the first cycle from $t = 1.33$ to 1.29. This is because we have increased the Deborah number independently without also considering the change in density and viscosity which we have assumed to be constant. In doing so, we can assess the effects of changing the relaxation time alone. However, in reality, the increased relaxation time would more than likely result in a change in the viscosity or density as the fluid becomes more non-Newtonian. This 'dependence' results in the non-monotonic relationship between the oscillation period and the Deborah number over the first oscillation period.

Furthermore, an increase in the Deborah number results in a significant increase in the maximum radius of the bubble over the first oscillation from 0.82 for $De = 0.0$, to 0.862 for $De = 20.0$. Note that on the second oscillation, the oscillation period no longer slightly decreases as the Deborah number increases. Now, an increase in the Deborah number results in an significant increase in the oscillation period. As the Deborah number increases from $De = 0.0$ to $De = 20.0$, the oscillation time for the evolution of the bubble over the first two cycles increases from $t = 2.54$ to 2.78. Note that, from equation (3.3.1) as the Deborah number increases significantly, the model approaches the inviscid case meaning there is less viscous damping between oscillations. This becomes apparent from the maximum radius of the bubble over the second oscillation of the bubble which increases from 0.74 for $De = 0.0$ to 0.86 for $De = 20.0$. The increased maximum radius and oscillation period results from the increased elasticity of the fluid. As the elasticity increases, more energy is saved rather than dissipated throughout the fluid and is therefore better captured by the bubble.

We consider the effect of the Deborah number on the average velocity of the bubble. The average velocity of the bubble over the first two oscillations for $De =$ 0.0, 0.2, 2.0, and 20.0 is given by Figure 4.5. As shown, and increase in the Deborah number results in an substantial increase in the absolute value of the average velocity on the bubble surface from 3.06 for $De = 0.0$ to 4.30 for $De = 20.0$ at the end of

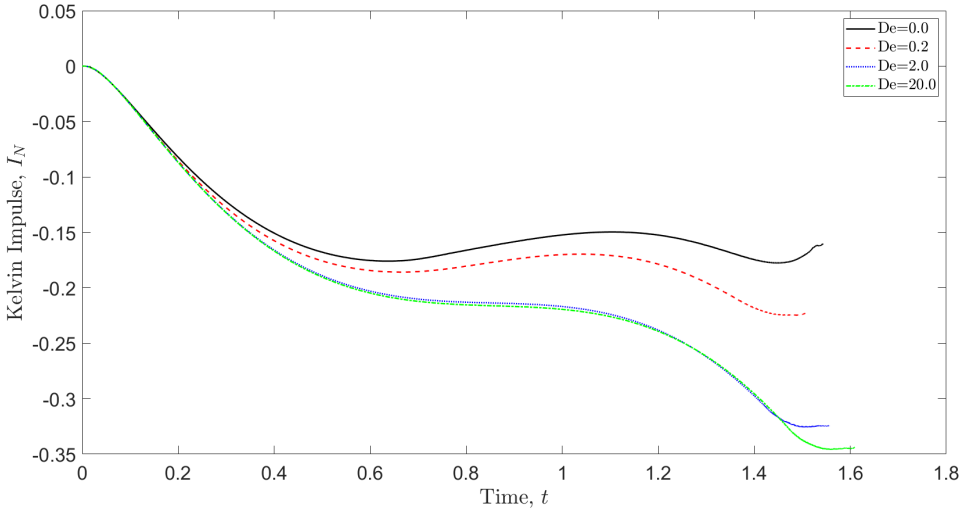


Figure 4.7: The influence of the Deborah number, De, on the Kelvin impulse of a bubble near a wall with stand-off distance $\gamma = 1.0$ in a Maxwell fluid. The parameters of the surrounding liquid are the same as in Figure 4.1.

the first oscillation. This corresponds to a 41% increase in the absolute value of the average velocity. Similarly, over the second oscillation, there is a 98% increase from 2.20 to 4.35.

4.2 Bubble near a flat rigid boundary

We now consider the effect of the Deborah number on the evolution of a microbubble near a flat rigid boundary. The parameters of the bubble and the surrounding fluid are the same as for Section 4.1.1 with the stand-off distance from the rigid boundary being $\gamma = 1.0$.

4.2.1 Results on radius history, bubble migration, Kelvin impulse and jet shape

The radius histories of the bubble over the first oscillation and subsequent bubble collapse are given by Figure 4.6 for $De = 0.0$, 0.2, 2.0, and 20.0. As with the radius of the bubble in an infinite fluid, a small increase in the Deborah number

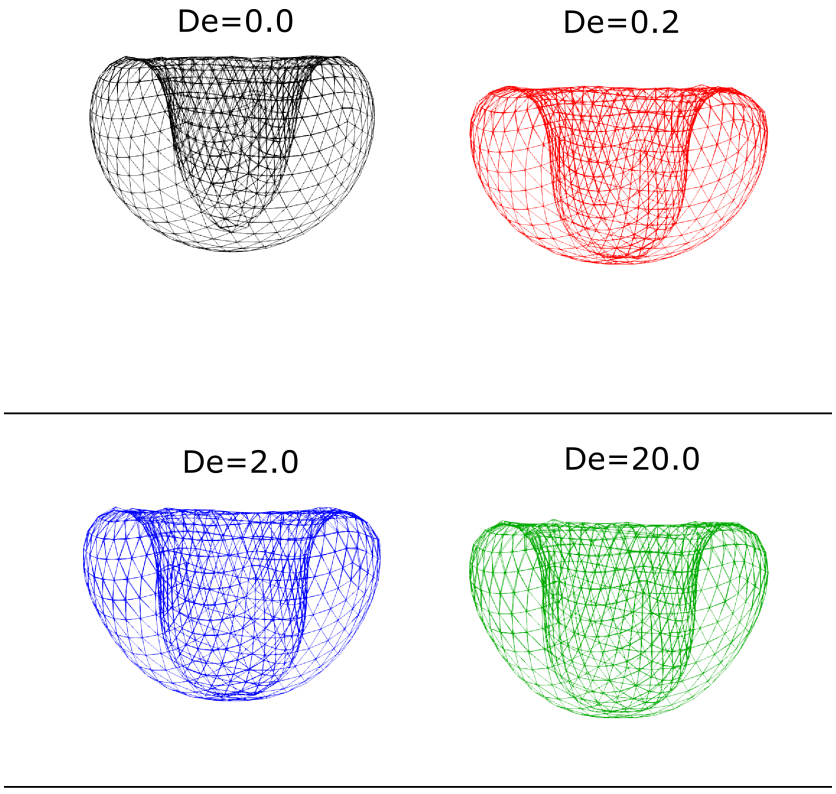


Figure 4.8: The influence of the Deborah number, De, on the jet shape of a bubble near a wall with stand-off distance $\gamma = 1.0$ in a Maxwell fluid. The parameters of the surrounding liquid are the same as in Figure 4.1.

from $De = 0.0$ to $De = 0.2$ results in a slight decrease in the bubble radius and oscillation time. However, increasing the Deborah number further results in both an increase in the bubble radius and the oscillation period.

We can now see the effect of the Deborah number on the Kelvin impulse of the bubble in the direction of the wall. The Kelvin impulse towards the wall over the first oscillation and subsequent bubble collapse is given by Figure 4.7 for $De = 0.0$, 0.2, 2.0, and 20.0. As shown, an increase in the Deborah number results in a large increase in the absolute value of the Kelvin impulse and therefore corresponds to a higher apparent inertia towards the wall. The absolute value of the Kelvin impulse, I_N, increases from 0.18 for $De = 0.0$ to 0.35 for $De = 20.0$ which represents a 94% increase.

Now we consider the shape of the bubble profile at collapse. The jet shapes are given in Figure 4.8 for $De = 0.0$, 0.2, 2.0, and 20.0, with the black line below the

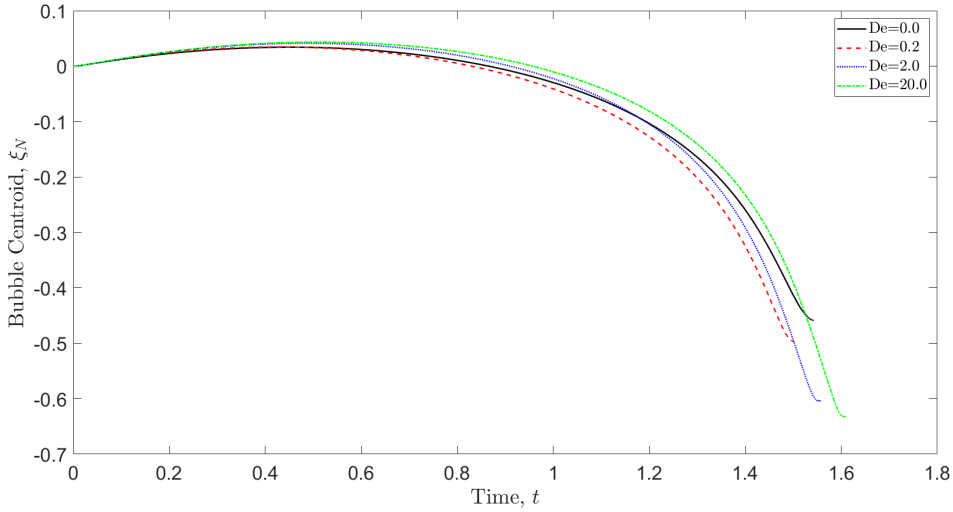


Figure 4.9: The influence of the Deborah number, De, on the migration of a bubble near a wall in a Maxwell fluid. The stand-off distance is given by $\gamma = 1.0$ and the location of the wall would correspond to the line $\xi_N = -1.0$. The parameters of the surrounding liquid are the same as in Figure 4.1.

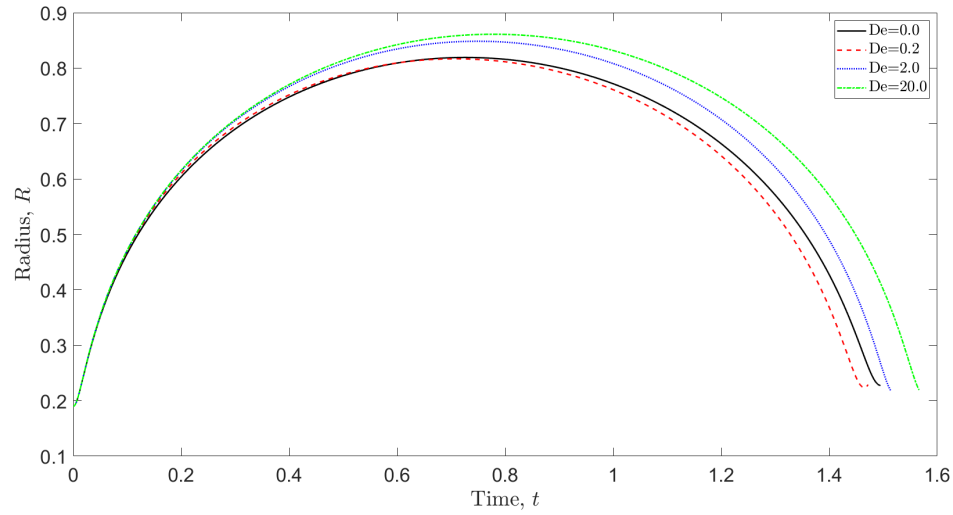


Figure 4.10: The influence of the Deborah number, De, on the radius history of a bubble near a wall with stand-off distance $\gamma = 1.25$ in a Maxwell fluid. The parameters of the surrounding liquid are the same as in Figure 4.1.

bubbles representing the location of the rigid boundary. As shown, the bubble itself is flatter as the Deborah number increases. This is because the bubble collapses to a smaller radius as the Deborah number increases, as shown in Figures 4.4 and 4.6. As a direct result, the jet is also flatter and broader at collapse as the Deborah number increases. Furthermore, the jet migration towards the wall is greater as the

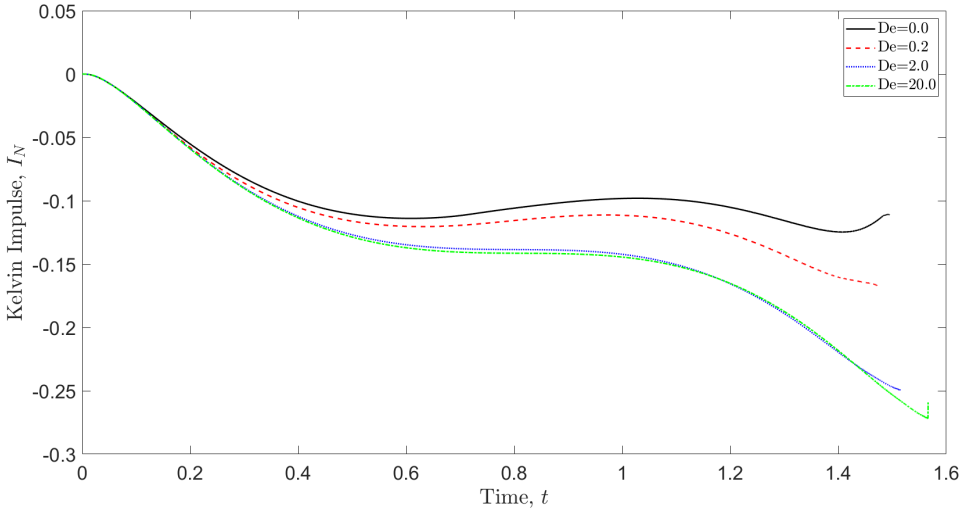


Figure 4.11: The influence of the Deborah number, De, on the Kelvin impulse of a bubble near a wall with stand-off distance $\gamma = 1.25$ in a Maxwell fluid. The parameters of the surrounding liquid are the same as in Figure 4.1.

Deborah number increases. This point is both shown in Figure 4.8 and reiterated in Figure 4.9 which shows the bubble centroid migration towards the rigid boundary for the first oscillation which achieves a greater negative value as De increases.

4.2.2 Increased stand-off distance

Next, we consider the effect of the Deborah number on the evolution of a microbubble near a flat rigid boundary with an increased stand-off distance to see if the viscoelastic effects are consistent for all stand-off distances. The parameters of the bubble and the surrounding fluid are once again the same as for Section 4.1.1 with the stand-off distance from the rigid boundary now being $\gamma = 1.25$.

The radius of the bubble near a wall with stand-off distance $\gamma = 1.25$, over the first oscillation and subsequent bubble collapse is given by Figure 4.10 for $De = 0.0$, 0.2, 2.0, and 20.0. As with the radius of the bubble near a wall of stand-off distance $\gamma = 1.0$, a small increase in the Deborah number from $De = 0.0$ to $De = 0.2$ results in a slight decrease in the bubble radius and oscillation time. However, increasing the Deborah number further results in both an increase in the bubble radius and

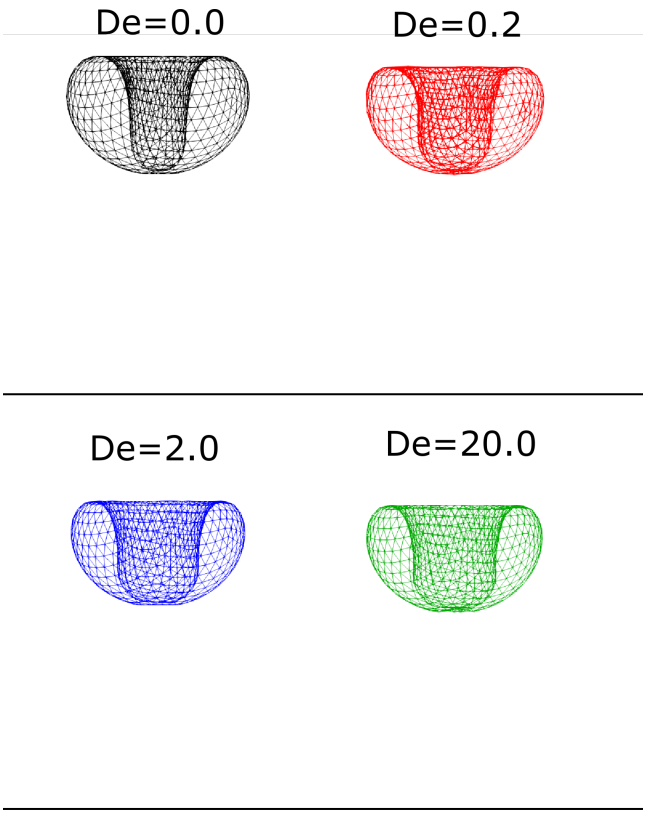


Figure 4.12: The influence of the Deborah number, De, on the jet shape of a bubble near a wall with stand-off distance $\gamma = 1.25$ in a Maxwell fluid. The parameters of the surrounding liquid are the same as in Figure 4.1.

the oscillation period as before. This suggests that the stand-off distance has no effect on the trend of the bubble radius and oscillation period due to an increased Deborah number.

We can now see the effect of the Deborah number on the Kelvin impulse of the bubble in the direction of the wall. The Kelvin impulse towards the boundary over the first oscillation and subsequent bubble collapse is given by Figure 4.11 for $De = 0.0$, 0.2, 2.0, and 20.0. Once again, an increase in the Deborah number results in a large increase in the absolute value of the Kelvin impulse and therefore corresponds to a higher apparent inertia towards the wall. The absolute Kelvin impulse increases from 0.11 for $De = 0.0$ to 0.27 for $De = 20.0$ which represents a 145% increase, which is a greater change than for the smaller stand-off distance of $\gamma = 1.0$. However, note that the absolute values of the Kelvin impulse are lower now

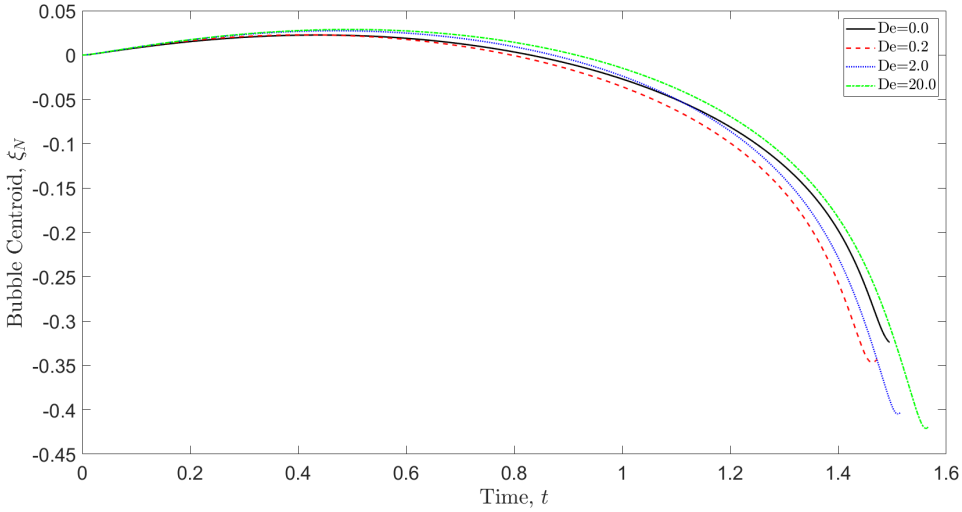


Figure 4.13: The influence of De on the migration of a bubble near a wall in a Maxwell fluid. The stand-off distance is given by $\gamma = 1.25$ and the location of the wall would correspond to the line $\xi_N = -1.25$. The parameters of the surrounding liquid are the same as Figure 4.1.

due to the larger stand-off distance but the overall trend with the Deborah number is still the same.

Next, we consider the shape of the bubble profile at collapse. The jet shapes are given in Figure 4.12 for $De = 0.0$, 0.2, 2.0, and 20.0, with the black line below the bubbles again representing the location of the rigid boundary. As shown, the bubble itself is flatter as the Deborah number increases, which is consistent with the smaller stand-off distance, due to the bubble collapsing to a smaller radius as the Deborah number increases. This is shown in Figures 4.4 and 4.10. As before the jet is also flatter and broader at collapse as the Deborah number increases and the jet migration towards the wall is greater as the Deborah number increases. This point is both shown in Figure 4.12 and reiterated in Figure 4.13 which shows the bubble centroid migration towards the boundary for the first oscillation which achieves a greater negative value as De increases. Hence, all investigated properties of the bubbles evolution are consistent for all stand-off distances. A point further reiterated in the next section.

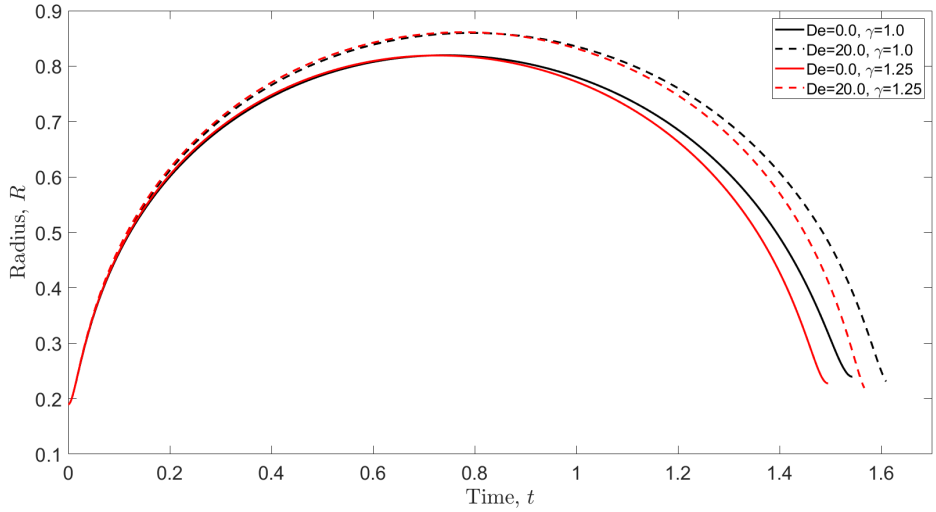


Figure 4.14: The influence of stand-off distance on the radius of a bubble near a flat rigid boundary in a Maxwell fluid. The remaining parameters are the same as for Figure 4.1.

4.2.3 Effect of stand-off distance

We now look at the effect of increasing the stand-off distance on the evolution of the bubble. Figure 4.14 shows the radius history for a bubble near a rigid wall of stand-off distances $\gamma = 1.0$ and $\gamma = 1.25$ for Deborah numbers $De = 0.0$ and 20.0. As shown, in both cases, the increase in oscillation time and maximum bubble radius are roughly the same. For $\gamma = 1.0$ the change in maximum radius and oscillation time is 0.040 and 0.067 respectively. Moreover, for $\gamma = 1.25$ the changes are 0.042 and 0.054. Hence, the influence of the Deborah number is comparable for any stand-off distance, γ.

4.3 Bubble near a rigid corner

We now analyse the effect of the Deborah number on a bubble situated near a rigid corner. The BIM code is implemented using a method of images on two separate rigid boundaries.

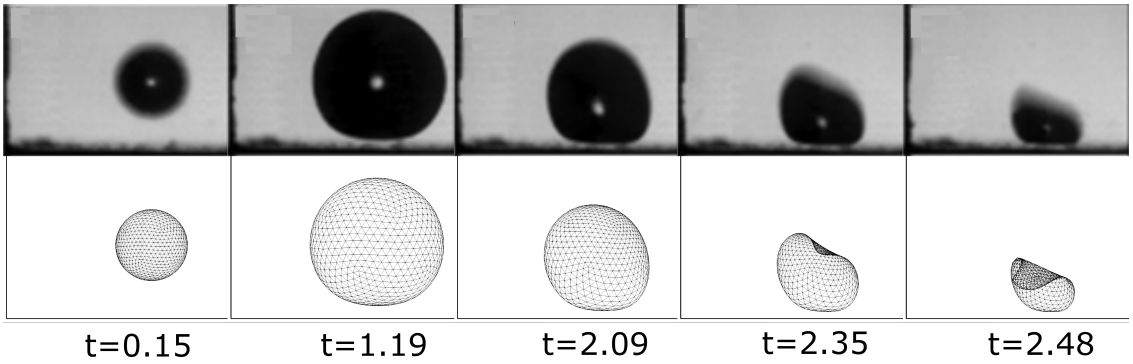


Figure 4.15: Comparison for the evolution of a bubble in a corner of angle, $\alpha = \pi/2$ between the BIM code and experimental data in a Newtonian fluid, with parameters $R_m^* = 0.85mm$, $\gamma_F = 2.17$, $\gamma_N = 1.08$, $\varepsilon = 100$, and $\kappa = 1.4$, where $Re = 8.4 \times 10^3$, $We = 8.7 \times 10^{-3}$, and $\delta = 0.009$.

4.3.1 Comparison with experimental data

To evaluate the Newtonian BIM model, we compare experimental data (Brujan et al. [2018]) with computational results calculated using the three-dimensional bubble code. The experiment is conducted for a laser-induced cavitation bubble situated near two rigid, $10mm$, aluminium walls. The bubbles were created in a glass tank filled with distilled water, by ionising the water using a high-energy laser with the energy deposited appearing as an expanding bubble. A high-speed camera was used to record the bubbles evolution with a frame rate of $100,000$ frames s^{-1}. The camera had a resolution of $14\mu m$ pixel^{-1} with a flash duration of $500\mu s$. Since, the bubble was situated in distilled water, the parameters of the fluid are readily available, such as surface tension, pressure, viscosity, and specific heat ratio. Using this information, the dimensionless parameters of the fluid, We, Re, and δ can be estimated to a great degree of accuracy. The pressure difference parameter, ε, is estimated under the assumption that the ionisation products consists of atomic hydrogen and oxygen with a small amount of water vapour. Upon doing so, a range of values can be considered and the simulations repeated until the desired value of P_{g0}, and hence ε, are found.

The experimental bubble has a maximum radius, $R_m = 0.85mm$ with an error estimation of $\pm 0.05mm$, at a right-angled corner of angle, $\alpha = \pi/2$. The stand-off

distances from the near and far wall are $\gamma_N = 1.08$ and $\gamma_F = 2.17$, respectively. The parameters of the fluid are given by $\epsilon = 100$, and $\kappa = 1.4$, where $Re = 8.4 \times 10^3$, $We = 8.7 \times 10^{-3}$, and $\delta = 0.009$.

As shown in Figure 4.15, during the early stages of expansion, the bubble remains relatively spherical except for the surface facing directly towards the near wall. The expansion of the surface on this side is restricted by the short stand-off distance. Continuing into the second and third frame, the surface furthest away from the corner still expands spherically, whilst the surfaces near to the walls are flattened, with greater flattening occurring close to the near wall. Examining frames four and five, as the bubble collapses the near wall surfaces remain in contact with the walls whilst the far side surface collapses inwards and a jet begins to form. Finally, at collapse, a wide jet forms and penetrates the bubble surface pointing towards the corner. As shown in Figure 4.15, all features are reproduced by the BIM three-dimensional computations and the bubble profiles are in very strong agreement with the experimental results.

We also compare the BIM model for a bubble near a corner of angle, $\alpha = \pi/4$, with experimental data. The experimental data is for a bubble with maximum radius, $R_m = 13.5mm$. The stand-off distances from the near and far wall are both $\gamma_N = 1.03$ and $\gamma_F = 1.03$. The parameters of the fluid are given by $\epsilon = 100$, and $\kappa = 1.4$, where $Re = 1.3 \times 10^5$, $We = 1886$, and $\delta = 0.036$. The comparison is shown in Figure 4.16. Once again, all features are reproduced by the BIM three-dimensional computations and the bubble profiles are in very strong agreement with the experimental results, meaning the BIM code can implemented for all simulations of a bubble near a corner of angles, $\alpha = \pi/2$ and $\alpha = \pi/4$.

4.3.2 Evolution of a bubble near a corner in a Maxwell fluid

We look at the evolution of a microbubble near corners of angle $\alpha = \pi/2$ and $\alpha = \pi/4$ in a Maxwell fluid with Deborah number $De = 2.0$. The stand-off distances are given

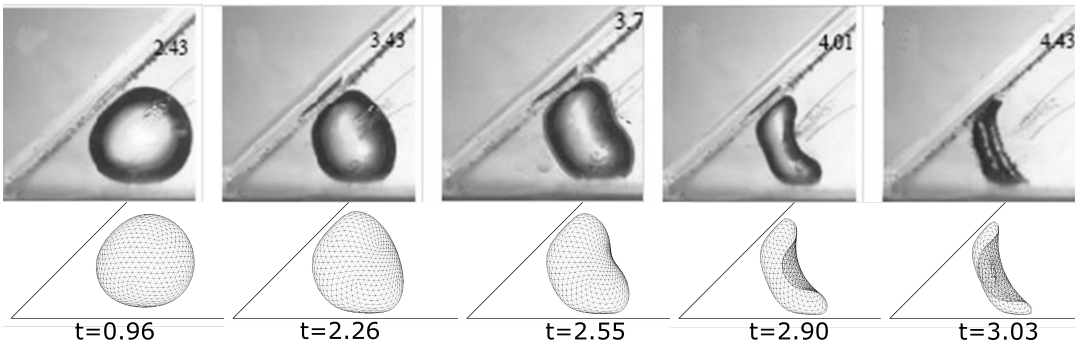


Figure 4.16: Comparison for the evolution of a bubble in a corner of angle, $\alpha = \pi/4$ between the BIM code and experimental data in a Newtonian fluid, with parameters $R_m^* = 13.5mm$, $\gamma_N = 1.03$, $\gamma_F = 1.03$, $\varepsilon = 100$, and $\kappa = 1.4$, where $Re = 1.3 \times 10^5$, $We = 1886$, and $\delta = 0.036$.

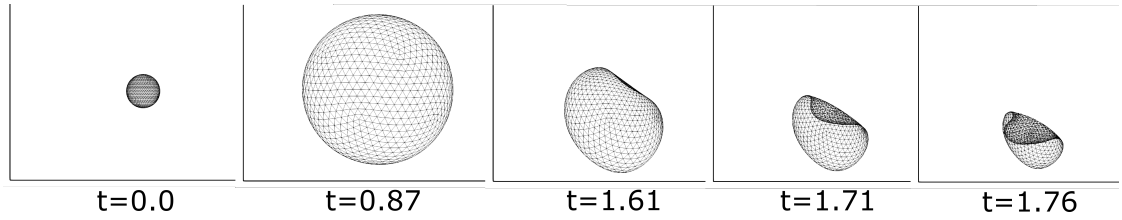


Figure 4.17: The evolution of a three-dimensional bubble near a right-angled corner in a Maxwell fluid of Deborah number $De = 2.0$ with stand-off distances, $\gamma_N = 1.0$ and $\gamma_F = 1.5$ towards the near and far wall, respectively. All remaining parameters are the same as in Figure 4.1.

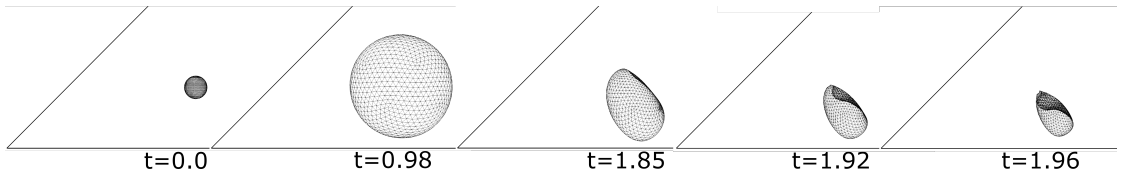


Figure 4.18: The evolution of a three-dimensional bubble near a corner of angle $\alpha = \pi/4$ in a Maxwell fluid of Deborah number $De = 2.0$ with stand-off distances, $\gamma_N = 1.0$ and $\gamma_F = 1.5$ towards the near and far wall, respectively. All remaining parameters are the same as in Figure 4.1.

by $\gamma_N = 1.0$ for the nearer horizontal wall below the bubble and $\gamma_F = 1.5$ for the further vertical wall to the left of the bubble. As shown in Figure 4.17 for $\alpha = \pi/2$, the bubble expands approximately spherically until it reaches its maximum volume at $t = 0.87$. Due to the Bjerknes forces from the two rigid walls, the majority of the non-spherical collapse occurs on the side of the bubble furthest away from the corner. So, as the jet starts to form at $t = 1.61$, the sides of the bubble nearest to the walls remain relatively spherical whilst the side furthest from the corner becomes

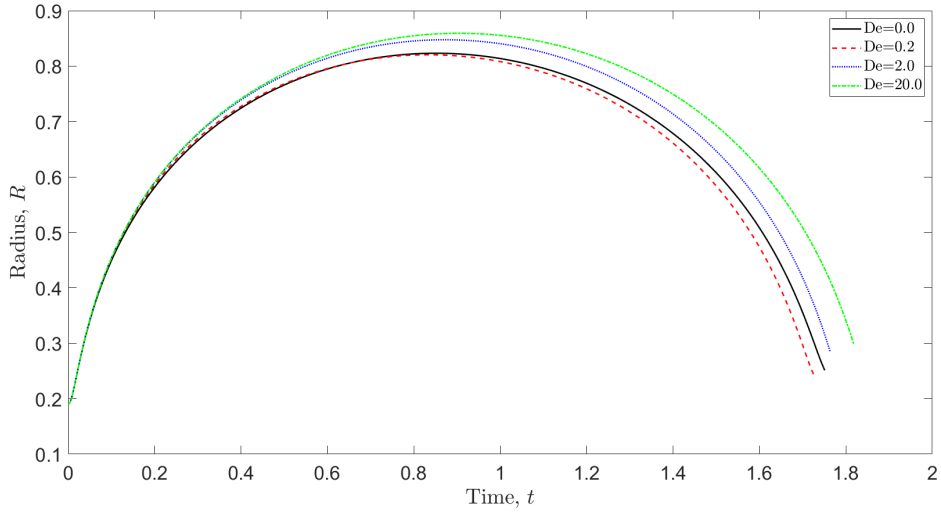


Figure 4.19: The influence of the Deborah number, De, on the radius history of a bubble near a corner of angle $\alpha = \pi/2$ with stand-off distances $\gamma_N = 1.0$ and $\gamma_F = 1.5$ in a Maxwell fluid. The parameters of the surrounding liquid are the same as in Figure 4.1.

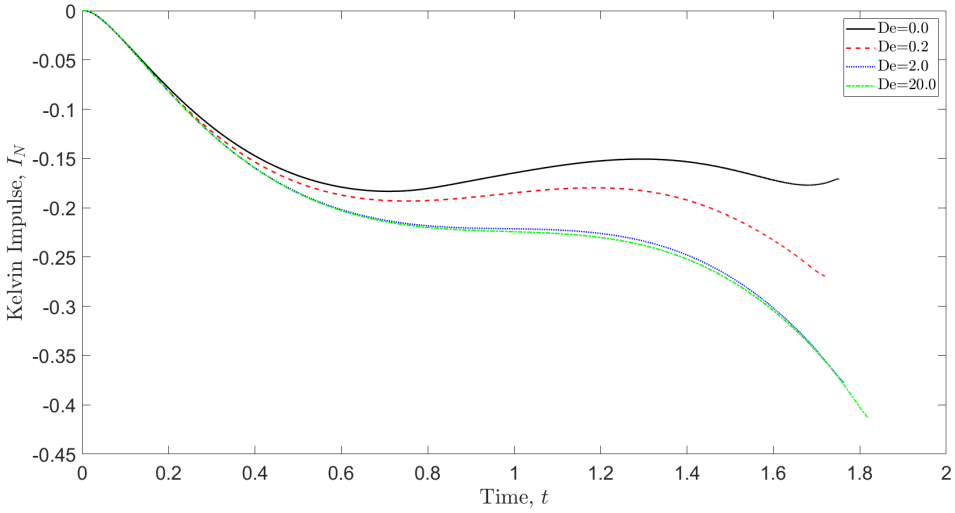


Figure 4.20: The influence of the Deborah number, De, on the Kelvin impulse towards the near wall of a bubble near a corner of angle, $\alpha = \pi/2$ in a Maxwell fluid. The parameters of the surrounding fluid are the same as in Figure 4.1.

flatter. Note that there is more flattening on the side of the bubble closest to the far wall as opposed to the side of the bubble closest to the near wall. The collapse continues in this fashion until the bubble becomes toroidal at $t = 1.76$ with the jet rotated towards the far wall. As can be seen, the bubble has migrated towards the near wall with the bottom of the bubble remaining nearly spherical.

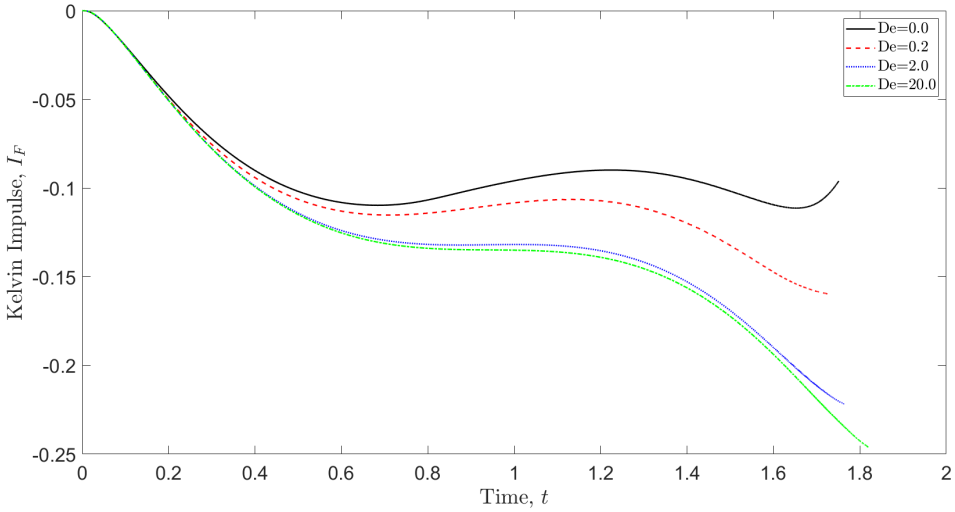


Figure 4.21: The influence of the Deborah number, De, on the Kelvin impulse towards the far wall of a bubble near a corner of angle, $\alpha = \pi/2$ in a Maxwell fluid. The parameters of the surrounding fluid are the same as in Figure 4.1.

Figure 4.18 shows the evolution of a bubble in a Maxwell fluid near a corner of angle $\alpha = \pi/4$. The evolution is similar to the bubble near a corner of angle, $\alpha = \pi/2$ with the collapse occurring mostly on the bubble surface furthest away from the corner, and the jet rotated towards the far wall. Note the increase in oscillation period from 1.76 to 1.96.

4.3.3 Bubble near a right-angled corner

We now conduct the simulations for $De = 0.0$, 0.2, 2.0, and 20.0 to analyse the effect of the Deborah number on the evolution of a microbubble near a corner of angle, $\alpha = \pi/2$. The parameters of the bubble and the surrounding fluid are once again the same as for Section 4.1.1 where now the stand-off distances are given by $\gamma_N = 1.0$ for the nearer horizontal wall below the bubble and $\gamma_F = 1.5$ for the further vertical wall to the left of the bubble.

As with the bubble in an infinite and semi-infinite fluid, we can once again consider the effect of the Deborah number, De, on the radius of the bubble near a corner. This is given in Figure 4.19. As with a bubble near a flat rigid boundary,

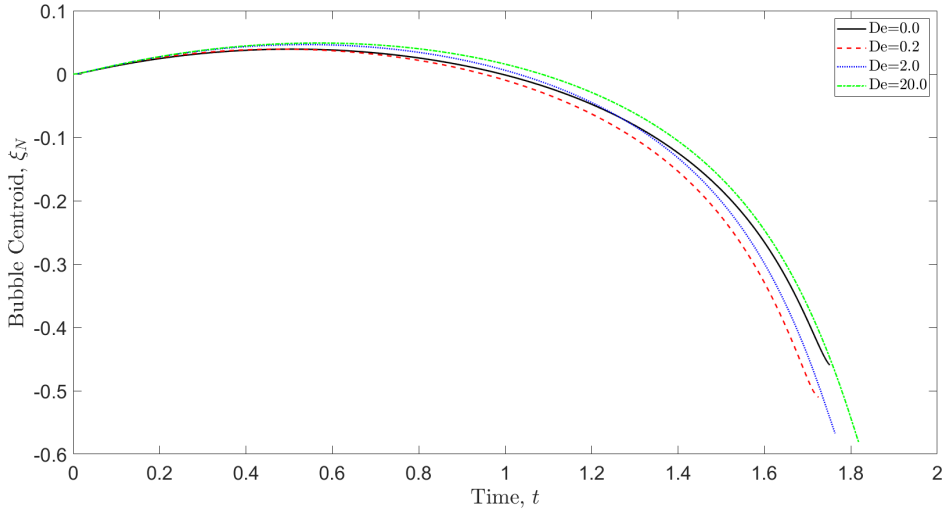


Figure 4.22: The influence of the Deborah number, De, on the migration towards the near wall of a bubble near a corner of angle $\alpha = \pi/2$ in a Maxwell fluid. The stand-off distance is given by $\gamma_N = 1.0$ and the location of the wall would correspond to the line $\xi_N = -1.0$. The parameters of the surrounding liquid are the same as in Figure 4.1.

an increase in the Deborah number increases the maximum radius of the bubble from 0.82 for $De = 0.0$ to 0.86 for $De = 20.0$. Likewise, the oscillation period also increases as the Deborah number increase from 1.75 to 1.82.

With the inclusion of two rigid boundaries to form a right-angled corner, we can now inspect the effect of the Deborah number, De, on the Kelvin impulse on the bubble towards both walls. The Kelvin impulse towards the near wall is given in Figure 4.20 for $De = 0.0$, 0.2, 2.0, and 20.0. As with the case for a bubble near a flat rigid boundary, an increase in De results in an increase of the absolute value of the Kelvin impulse at collapse from 0.17 for $De = 0.0$ to 0.41 for $De = 20.0$, corresponding to a 141% increase which is greater than the corresponding increase near a singular flat rigid boundary. Furthermore, a similar analysis can be done on the Kelvin impulse on the bubble in the direction of the far wall. This is presented in Figure 4.21. As with the near boundary, an increase in the Deborah number increases the absolute value of the Kelvin impulse at collapse from 0.09 for $De = 0.0$ to 0.25 for $De = 20.0$, corresponding to a 178% increase. Note that the values for

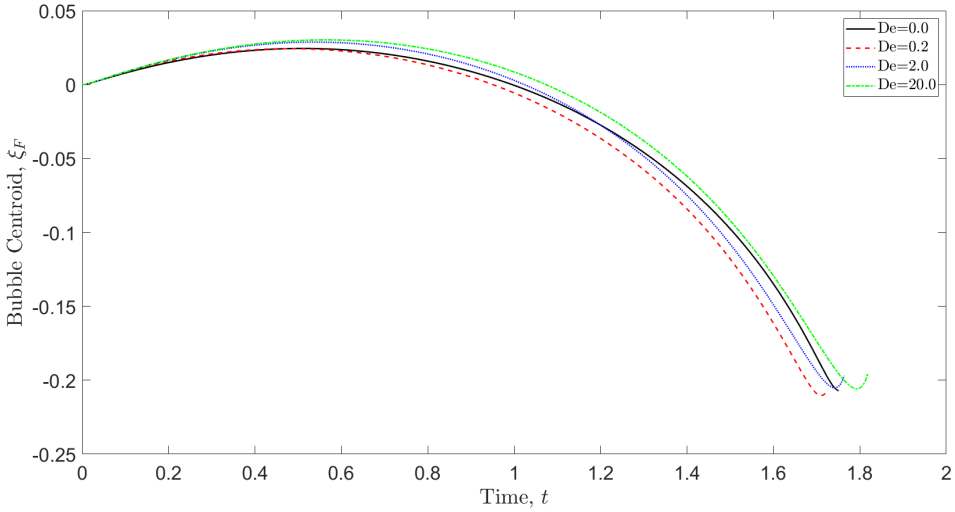


Figure 4.23: The influence of the Deborah number, De, on the migration towards the far wall of a bubble near a corner of angle, $\alpha = \pi/2$ in a Maxwell fluid. The stand-off distance is given by $\gamma_F = 1.5$ and the location of the wall would correspond to the line $\xi_F = -1.5$. The parameters of the surrounding liquid are the same as in Figure 4.1.

the Kelvin impulse are smaller in this direction due to the increased initial stand-off distance.

The results on the Kelvin impulse have a direct impact on the bubble migration. As with the case with one rigid boundary, we can analyse the bubble migration towards the near wall. This is given in Figure 4.22. As before the bubble migration towards the near wall increases as the Deborah number increases. However, now there is the bubble migration towards the far wall to consider also. This is shown in Figure 4.23. As can be seen, there appears to not be much of a difference in the bubble migration towards the far wall as what was seen towards the near wall before. Note from Figure 4.24 that indeed the left-hand side of the bubble is closer to the vertical wall, but so also the right-hand side of the bubble is further away as the Deborah number increases. So the bubble centroid remains in a roughly similar position for all Deborah numbers.

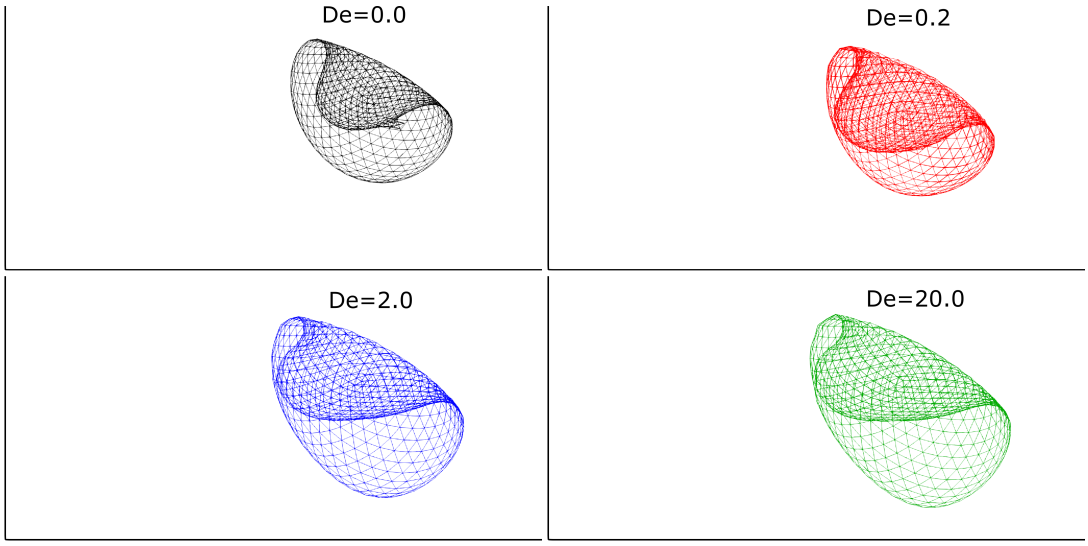


Figure 4.24: The influence of the Deborah number, De, on the jet profile of a bubble initiated in a corner of angle, $\alpha = \pi/2$. The remaining parameters are the same as in Figure 4.1.

4.3.4 Results on jet shape and angle at collapse

Once again we can consider the bubble profile at collapse shown in Figure 4.24. Similar to the single rigid boundary, the jet shape is broader as the Deborah number increases. However, now the bubble is much larger as the jet penetrates through the surface. This is a result of the higher maximum radius as De increases, as there is a greater Bjerknes attraction between the bubble and the horizontal wall below the bubble. This is apparent from the fact that the bottom of the bubble is much closer to the horizontal wall as the Deborah number increases. Furthermore, because of this Bjerknes attraction, the jetting angle is more towards the far wall to the left as the Deborah increases, with a more asymmetric profile overall, as the jet becomes more sloped.

4.3.5 Decreased corner angle

Next, we look at a microbubble initiated near a corner of angle, $\alpha = \pi/4$ in a Maxwell fluid with Deborah numbers $De = 0.0$, 0.2, 2.0, and 20.0. The stand-off distances are given by $\gamma_N = 1.0$ for the nearer horizontal wall below the bubble and

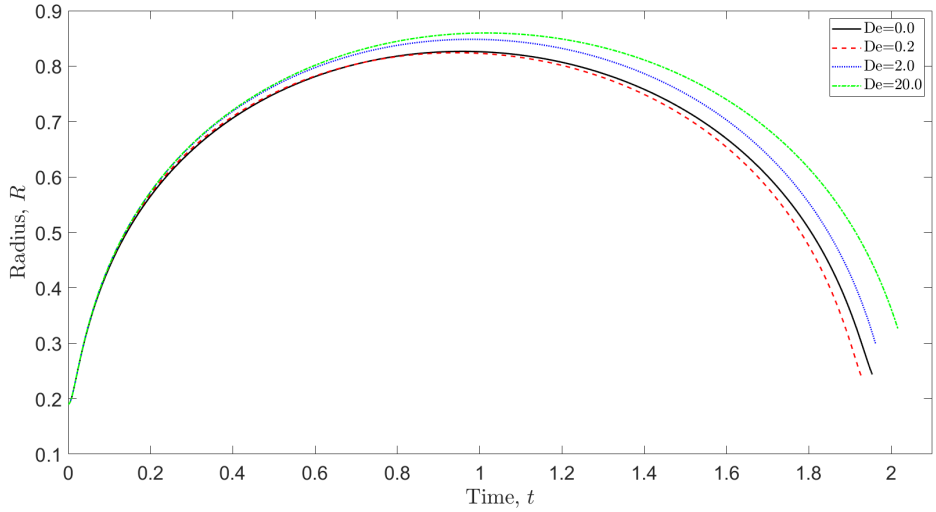


Figure 4.25: The influence of the Deborah number, De, on the radius history of a bubble near a corner of angle, $\alpha = \pi/4$ with stand-off distances $\gamma_N = 1.0$ and $\gamma_F = 1.5$ in a Maxwell fluid. The parameters of the surrounding liquid are the same as in Figure 4.1.

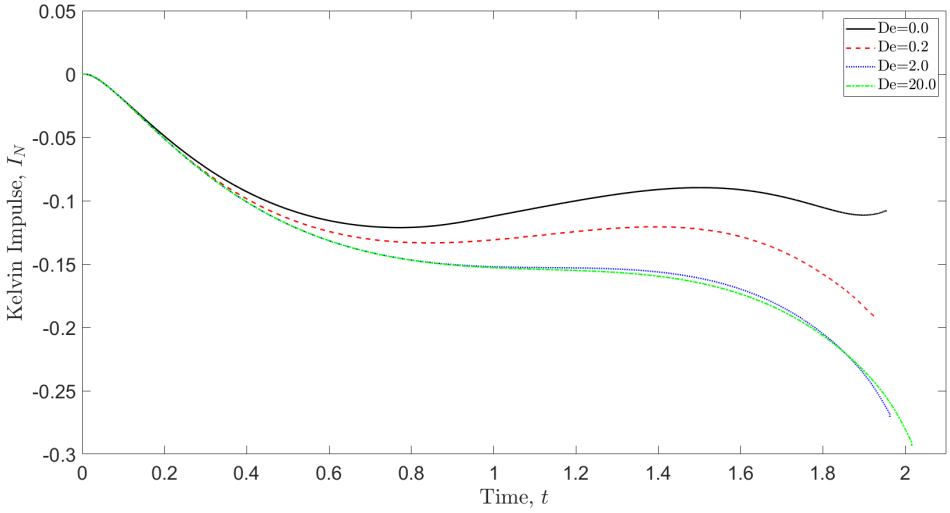


Figure 4.26: The influence of the Deborah number, De, on the Kelvin impulse towards the near wall of a bubble near a corner of angle, $\alpha = \pi/4$ in a Maxwell fluid. The parameters of the surrounding fluid are the same as in Figure 4.1.

$\gamma_F = 1.5$ for the further diagonal wall to the left of the bubble as before. All other parameters are the same as in Figure 4.1.

As with the bubble near a corner of angle $\alpha = \pi/2$, we can once again consider the effect of the Deborah number, De, on the radius of the bubble now near a corner of angle, $\alpha = \pi/4$. This is given in Figure 4.25. As with a bubble near a corner of

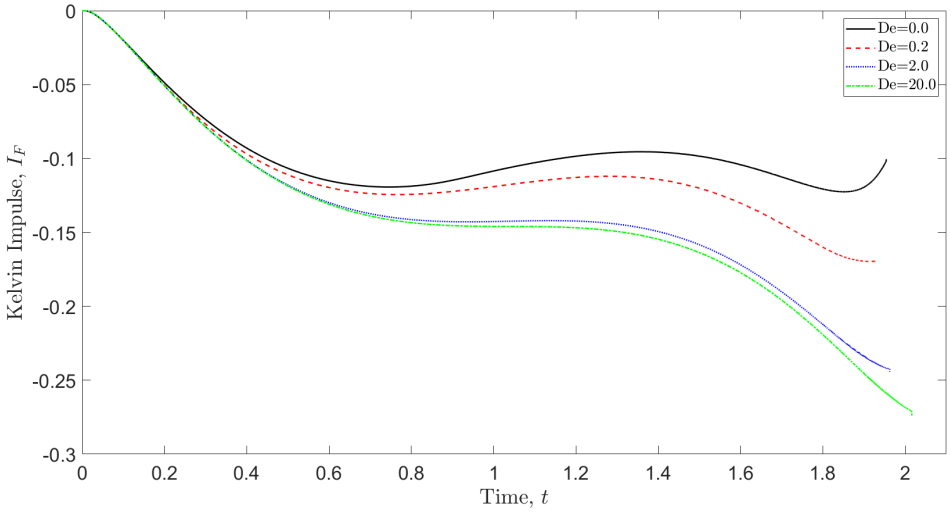


Figure 4.27: The influence of the Deborah number, De, on the Kelvin impulse towards the far wall of a bubble near a corner of angle, $\alpha = \pi/4$ in a Maxwell fluid. The parameters of the surrounding fluid are the same as in Figure 4.1.

angle $\alpha = \pi/2$, an increase in the Deborah number increases the maximum radius of the bubble from 0.83 for $De = 0.0$ to 0.86 for $De = 20.0$. Likewise, the oscillation period also increases as the Deborah number increases from 1.95 to 2.02.

We can again inspect the effect of the Deborah number, De, on the Kelvin impulse on the bubble towards both walls. The Kelvin impulse, I_N, towards the near wall is given in Figure 4.26 for $De = 0.0$, 0.2, 2.0, and 20.0. As with the case for a bubble near a corner of angle, $\alpha = \pi/2$, an increase in De results in an increase in the absolute value of the Kelvin impulse at collapse from 0.11 for $De = 0.0$ to 0.29 for $De = 20.0$, corresponding to a 164% increase. Furthermore, a similar analysis can be done on the Kelvin impulse on the bubble in the direction of the far wall. This is presented in Figure 4.27. As with the near boundary, an increase in the Deborah number increases the absolute value of the Kelvin impulse, I_F, at collapse from 0.10 for $De = 0.0$ to 0.27 for $De = 20.0$, corresponding to a 170.0% increase. As with a bubble near a corner of angle $\alpha = \pi/2$, note that the values for the Kelvin impulse are smaller in this direction due to the increased initial stand-off distance.

We can analyse the bubble migration towards the near wall. This is given in Figure 4.28. As before the bubble migration towards the near wall increases as the

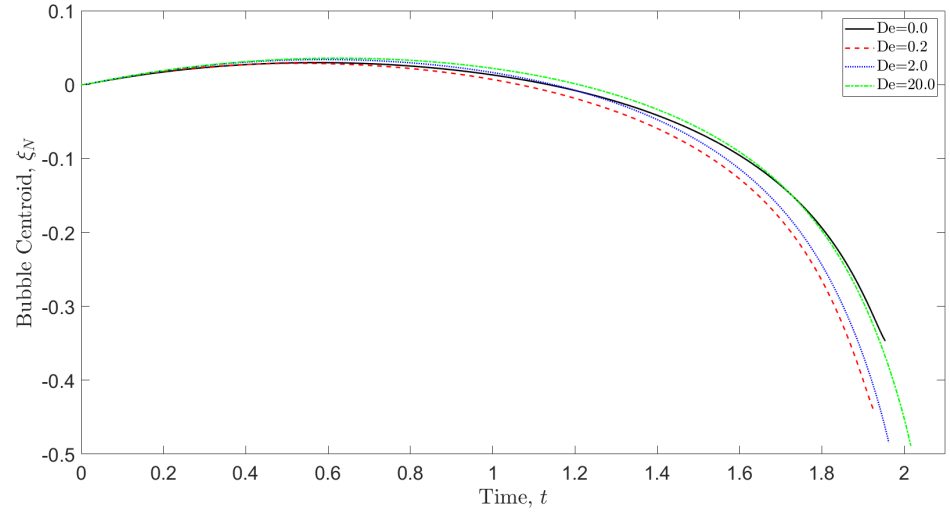


Figure 4.28: The influence of the Deborah number, De, on the migration towards the near wall of a bubble near a corner of angle, $\alpha = \pi/4$ in a Maxwell fluid. The stand-off distance is given by $\gamma_N = 1.0$ and the location of the wall would correspond to the line $\xi_N = -1.0$.The parameters of the surrounding liquid are the same as in Figure 4.1.

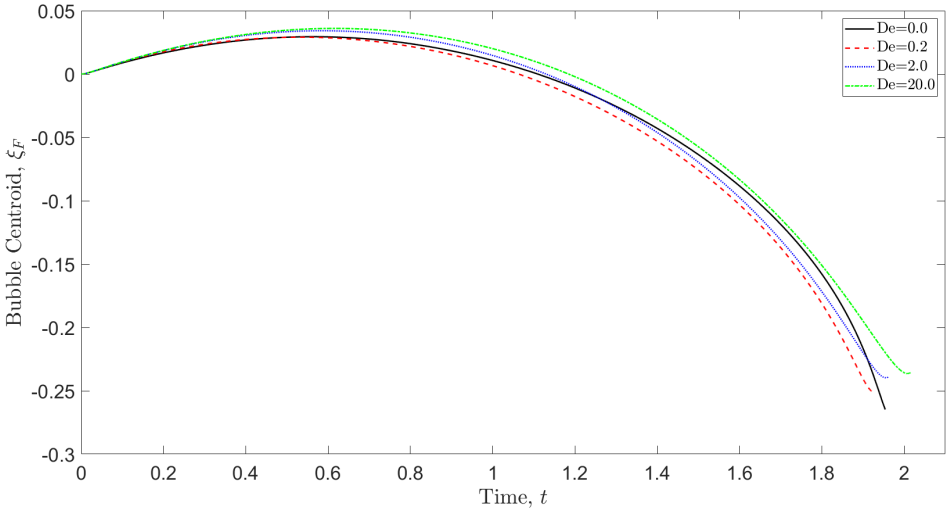


Figure 4.29: The influence of the Deborah number, De, on the migration towards the far wall of a bubble near a corner of angle, $\alpha = \pi/4$ in a Maxwell fluid. The stand-off distance is given by $\gamma_F = 1.5$ and the location of the wall would correspond to the line $\xi_F = -1.5$. The parameters of the surrounding liquid are the same as in Figure 4.1.

Deborah number increases. However, now there is the bubble migration towards the far wall to consider also. This is shown in Figure 4.29. As can be seen, there appears to not be much of a difference in the bubble migration towards the far wall

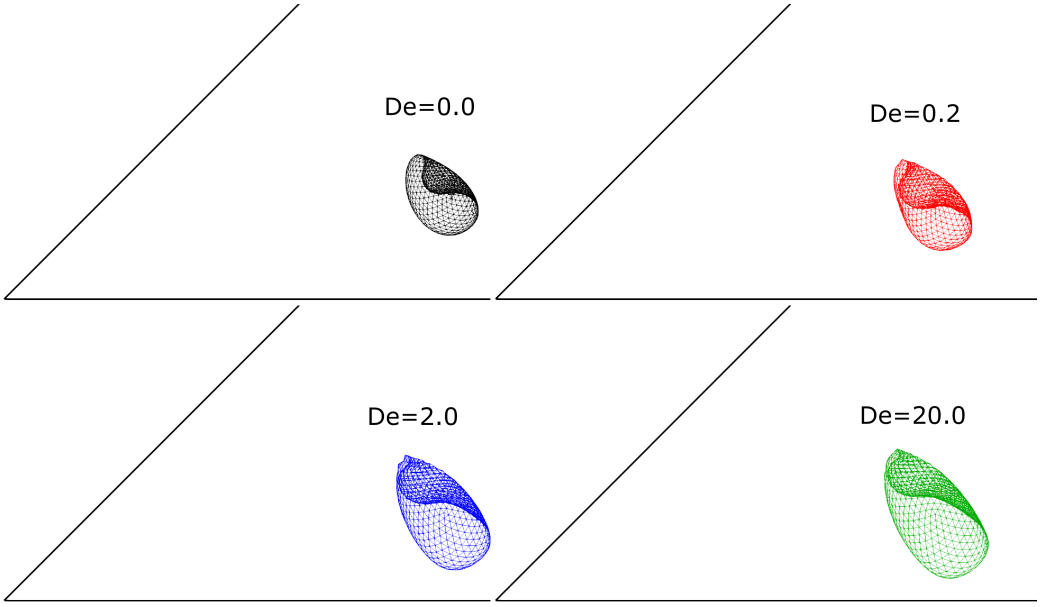


Figure 4.30: The influence of the Deborah number, De, on the jet profile of a bubble initiated in a corner of angle, $\alpha = \pi/4$. The remaining parameters are the same as in Figure 4.1.

as what was seen towards the near wall before. This is once again consistent with a bubble near a corner of angle $\alpha = \pi/2$, which also did not experience much change in migration towards the far wall. Note from Figure 4.30 however, that the left-hand side of the bubble is once again closer to the far wall, but also the right-hand side of the bubble is further away as the Deborah number increases. So the bubble centroid remains in a roughly similar position for all Deborah numbers.

The bubble profile at collapse for a corner of angle, $\alpha = \pi/4$ is provided in Figure 4.30. As shown, the collapse follows a similar trend for a corner of angle, $\alpha = \pi/2$. As the Deborah number increases, the jet is broader and the bubble collapses closer to the nearer boundary. Once again, the jet is rotated upwards towards the far wall. An effect that is more apparent here given the restricted domain size.

4.3.6 Effects of domain size on the bubble in a Maxwell fluid

We now look at the change in radius history between a Maxwell fluid of $De = 0.0$ and $De = 20.0$, for a bubble near corners of angles, $\alpha = \pi/2$ and $\pi/4$. This is shown

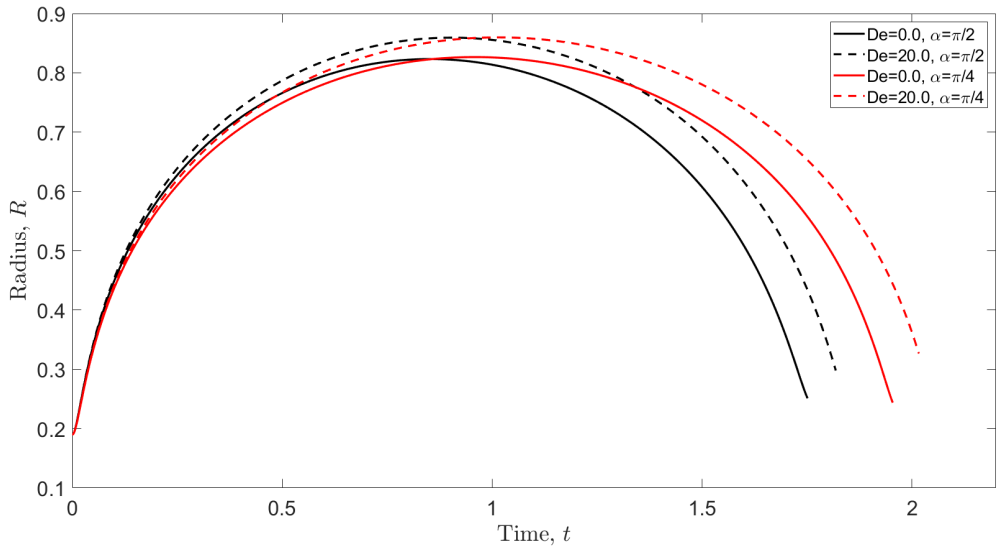


Figure 4.31: The influence of the domain size on the radius history of a bubble in a corner of various angles, α. The remaining parameters of the fluid are the same as in Figure 4.1.

in Figure 4.31 where the black lines represent $\alpha = \pi/2$ and the red lines represent $\alpha = \pi/4$. As shown, the maximum radius and oscillation period both once again increase with the Deborah number as discussed previously. However, restricting the domain size does not change the magnitude of this effect as the change in maximum radius and oscillation period is comparable for both corner angles. The oscillation period overall increases however, as the domain size is restricted (Wang et al. [2020]).

4.3.7 Convergence with Deborah number

We can now discuss the large scale effects of the Deborah number on the evolution of a bubble. Figure 4.32 shows the jet shape for bubbles at collapse in viscoelastic fluids of Deborah number $De = 2.0$, 20.0, 200.0, and 2000.0. As shown, an increase from $De = 2.0$ to 20.0 results in a slightly larger bubble and a jet angle pointed more towards the far wall. However, increasing the Deborah number beyond $De = 20.0$ results in minimal change to the bubble profile at collapse. This can be seen by observing that the bubble profile for $De = 200.0$ and $De = 2000.0$ have no significant

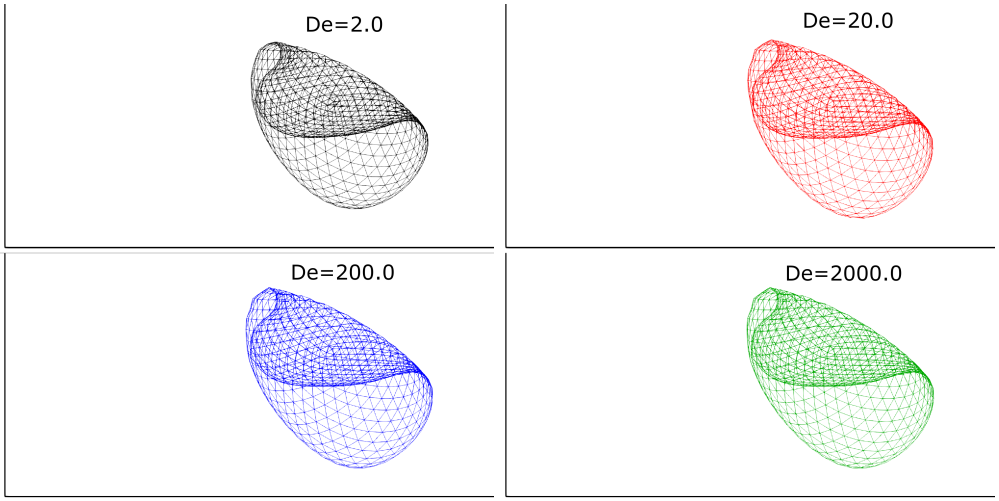


Figure 4.32: The large scale influence of the Deborah number on the jet profile of a bubble initiated in a corner of angle, $\alpha = \pi/2$. The remaining parameters are the same as in Figure 4.1.

differences from the bubble profile for $De = 20.0$. From Maxwell's constituitive equation (2.5.14), we can see that DT_{nn}/Dt is inversely proportional to De. As De is large, DT_{nn}/Dt and T_{nn} are small and negligible. As De increases, the Maxwell model converges to the non-viscous model where $T_{nn} \approx 0$ for all time.

This point is further shown in Figure 4.33 which shows the bubble radius history for $De = 2.0$, 20.0, 200.0, and 2000.0. As shown, an increase from $De = 2.0$ to $De = 20.0$ results in a significant increase in the maximum radius and oscillation period of the bubble. However, any subsequent increase past $De = 20.0$ results in no significant change in the maximum radius or oscillation period of the bubble.

4.3.8 Convergence with Reynolds number

We can also discuss the large scale influence of the Reynolds number on the evolution of a bubble near a rigid corner. Figure 4.34 shows the jet shapes at collapse for a bubble in a Maxwell fluid of Reynolds number, $Re = 450$ for $De = 0.0$, 0.2, 2.0, and 20.0. As shown, at this level of viscosity, the change in relaxation time of the fluid makes little to no difference on the collapse of the bubble as all jet profiles are comparable. This is apparent from equation (2.5.14), as the viscous effects and

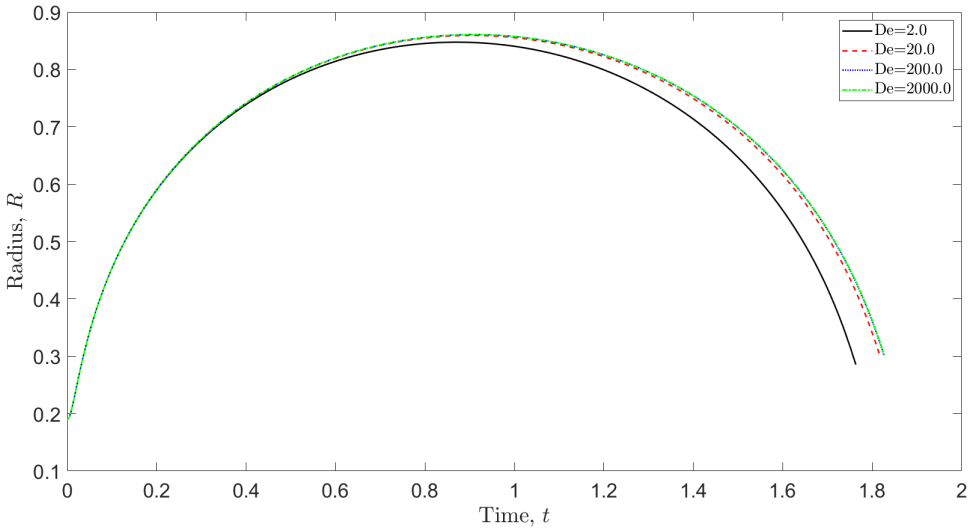


Figure 4.33: The large scale influence of the Deborah number, De, on the radius history of a bubble initiated in a corner of angle, $\alpha = \pi/2$. The remaining parameters are the same as in Figure 4.1.

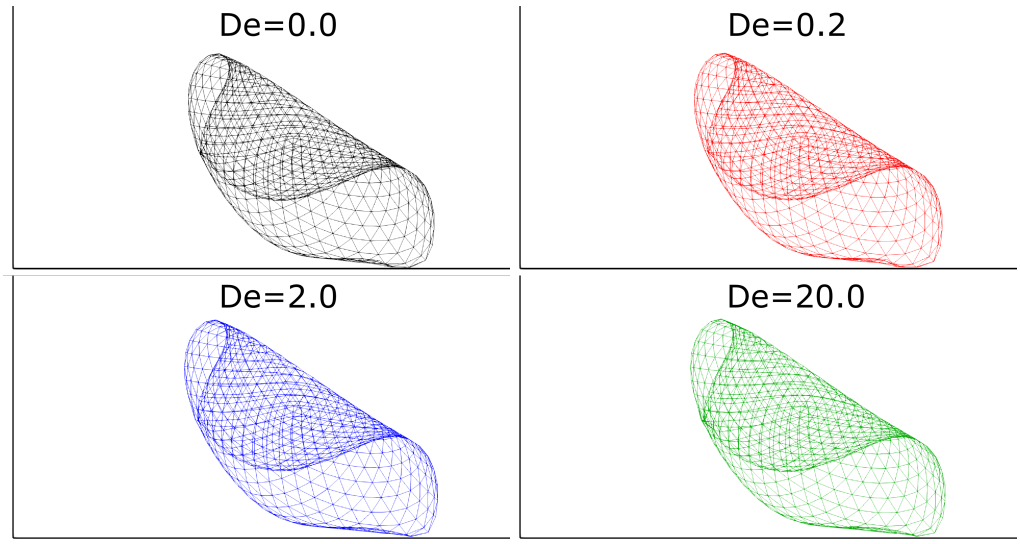


Figure 4.34: The influence of the Deborah number, De, on the jet profile of a bubble in a corner of angle, $\alpha = \pi/2$ with $Re = 450$. The remaining parameters are the same as in Figure 4.1.

viscoelastic effects become negligible as the Reynolds number increases.

This point is further reiterated by looking at the bubble radius in a Maxwell fluid of Reynolds number $Re = 450$ for $De = 0.0$, 0.2, 2.0, and 20.0. This is given in Figure 4.35. As can be seen, any change in the Deborah number results in little to no change in the bubble history or oscillation time, meaning the viscoelastic effects

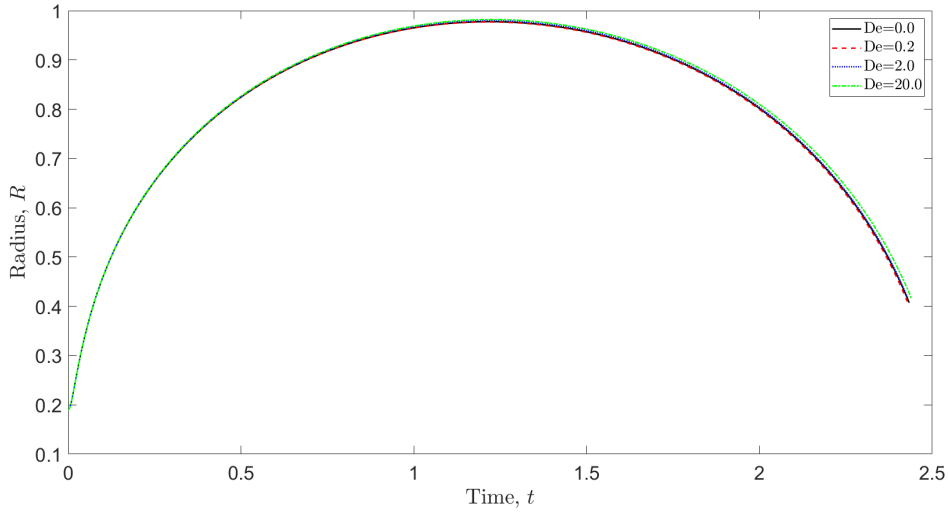


Figure 4.35: The influence of the Deborah number, De, on the radius of a bubble in a corner of angle, $\alpha = \pi/2$ with $Re = 450$. The remaining parameters are the same as in Figure 4.1.

of the fluid only affect the evolution of a bubble in lower Reynolds number fluids.

4.4 Conclusion

Bubble dynamics in non-Newtonian liquids are associated with wide applications in engineering and biomedical ultrasonics. A numerical model is described based on the boundary integral method coupled with the Maxwell constitutive equation. Here the flow is assumed to have moderate to high Reynolds number and thus is irrotational in the bulk domain. The viscoelastic effects are not negligible in a thin viscous layer at the bubble surface, and are approximated only through the normal stress balance at the bubble surface. A backwards Euler method is used to iteratively solve the Maxwell constitutive equation for the normal stress tensor. Computations are carried out for a bubble near a corner at various corner angles using the Green's function for the Laplace equation in the corner domain. The numerical model has excellent agreement with the corresponding Rayleigh-Plesset equation for spherical bubbles in a non-Newtonian liquid. The numerical results also agree very well with

the experiments for bubbles in a Newtonian fluid in a corner. Viscoelastic effects are studied in terms of Deborah number De, which is a ratio of the time it takes for a material to adjust to applied stresses to the characteristic bubble oscillation time. Simulation were performed for $De = 0.0$ (Newtonian fluid), $De = 0.02$, 2.0, and 20.0 (viscoelastic fluid).

The following new phenomena/features were observed:

1. The maximum radius and oscillation period increase with the Deborah number. This is due to more elastic energy being stored and released in the viscoelastic fluid for a larger Deborah number and less energy being lost due to viscosity.

2. The wall effects due to the corner are enhanced with a larger De as a result of an increase in the maximum radius. Bubble migration and oscillation amplitude increase with Deborah number.

3. The bubble jet shape is broader and flatter for a bubble near a rigid boundary or in a corner as De increases. The bubble jet is inclined to the further boundary when it is in a corner as De increases.

4. Results converge as Deborah number increases as the elastic effects become dominant compared with the viscous damping effects of the fluid.

5. Results converge as the Reynolds number increases as the viscosity of the fluid becomes negligible.

In conclusion, an increased Deborah number greatly enhances the effects of the surrounding boundaries on the bubbles collapse and provides a broader, flatter jet. This implies that a higher Deborah number in the fluid will greatly improve surface cleaning of all surrounding boundaries for ultrasonic cavitation cleaning and result in greater administration of noninvasive therapy and drug delivery. On the negative

side, cavitation damage in machinery will be greater with an increase in the Deborah number.

CHAPTER 5

NUMERICAL SIMULATIONS OF THE JEFFREY MODEL

In this chapter, the numerical model established in Chapter 3 is implemented to analyse the effect of the viscosity ratio, β, on a three-dimensional bubble. The boundary integral method is firstly used to simulate the evolution of a bubble in various infinite Jeffrey fluids and is validated using comparisons between the BIM code and the Rayleigh-Plesset model for spherical bubbles in an infinite Jeffrey fluid. Results are then presented on the bubble radius history and average velocity over the bubble surface as a result of an increase in the polymeric viscous contribution of the fluid.

Furthermore, a flat rigid boundary is introduced below the microbubble and results are presented on the bubble centroid migration, Kelvin impulse and jet shape at collapse in different viscoelastic polymeric fluids. A second wall is then introduced the simulate the three dimensional effects on the bubble of a viscoelastic fluid near a corner. Results are given on the three-dimensional effects of the viscosity ratio, β, on the jet shape, bubble centroid migration and jetting angle. Also, results are given on the effects of reducing the fluid domain by changing the corner angle.

Finally, the large scale effects of the Deborah number and Reynolds number are analysed on all investigated properties of the bubble.

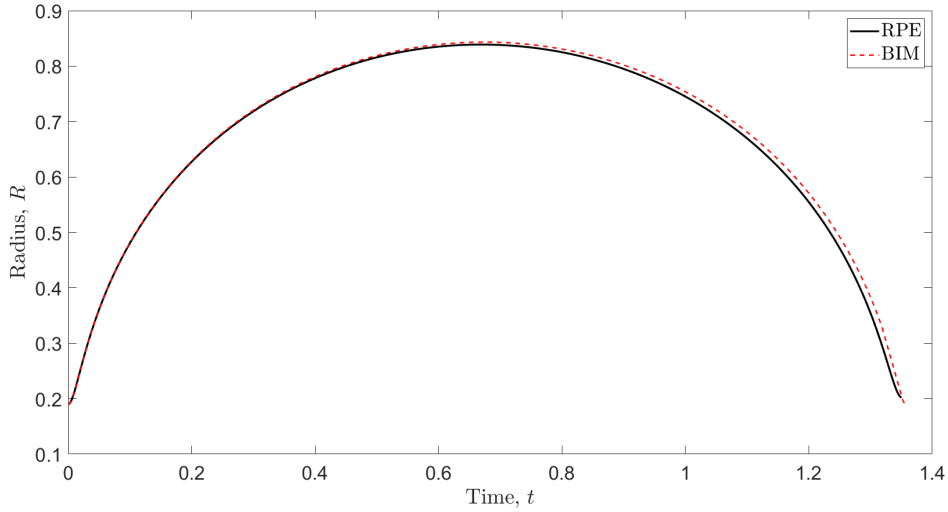


Figure 5.1: The comparison of the radius history of a spherical bubble in a Jeffrey fluid with $\beta = 0.4$, between the non-Newtonian Rayleigh-Plesset equation (2.3.6) and the BIM code. The parameters of the surrounding liquid are the same as in Figure 4.1.

5.1 Infinite fluid

5.1.1 Radius history validation with Rayleigh-Plesset equation

To validate the boundary integral method for the Jeffrey model, the radius history as computed by the BIM code is compared to the radius history given by the non-Newtonian Rayleigh-Plesset equation (2.3.6) with normal component of the stress tensor, T_{nn}, given by equation (2.5.23). As with Chapter 4, for the entirety of this Chapter, the microbubble has an initial radius of $R_0^* = 4.5\mu m$ where a level 10 mesh is used with the parameters of the gas and liquid being given by $\xi = 1.667$, $\sigma = 0.073 Nm^{-1}$, $P_0 = 101.3kPa$, $P_v = 0.023P_0$ and $\rho = 999 kgm^{-3}$. The pressure difference is set to $\varepsilon = 100$. The simulation is then repeated for a Jeffrey fluid with viscous ratios, $\beta = 0.2$, 0.4, 0.6 and 0.8. The results for the comparison between the code and the analytical solution for $\beta = 0.4$ are found in Figure 5.1. Similar results are shown in Appendix B.1 in Figures B.1, B.2, and B.3 for $\beta = 0.2$, 0.6, and 0.8 respectively.

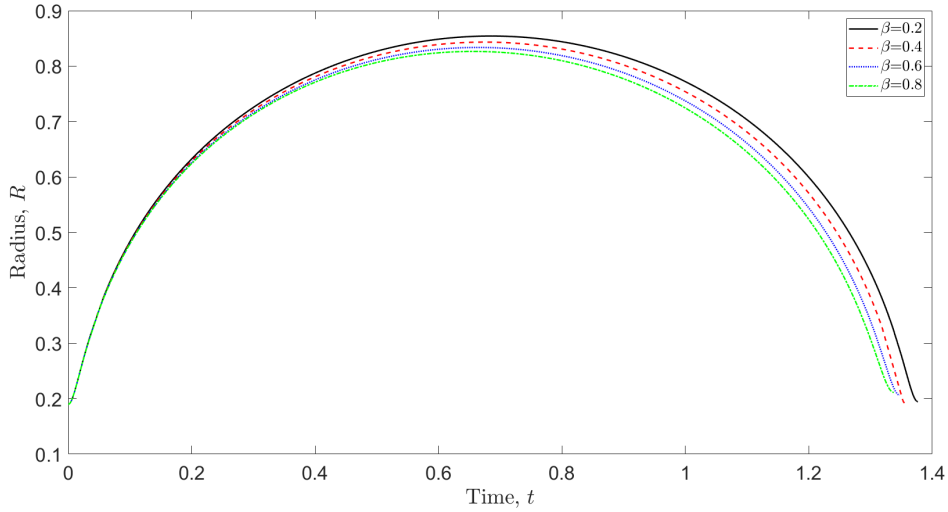


Figure 5.2: The influence of the viscosity ratio, β, on the radius history of a spherical bubble in an infinite Jeffrey fluid over the first oscillation. The parameters of the surrounding liquid are $\zeta = 1.667$, $\delta = 0$, $\sigma = 0.073 Nm^{-1}$, $P_0 = 101.3 kPa$, $P_v = 0.023 P_0$ and $\rho = 999 kgm^{-3}$.

Figure 5.1 represents the radius history for a bubble in a Jeffrey fluid with viscosity ratio, $\beta = 0.4$, as calculated both by the BIM three-dimensional code (black line) and the analytical solution the Rayleigh-Plesset equation (2.3.6) (red line). As shown, both the analytical solution to the Rayleigh-Plesset equation and the numerical solution provided by the BIM code are in strong agreement with each other over the entirety of the first oscillation for the Jeffrey model. Therefore, given the strong agreement between the two curves, the BIM can be implemented throughout the simulations in this thesis for a Jeffrey fluid.

5.1.2 Results for an infinite fluid

Firstly, we consider the evolution of a microbubble in an infinite fluid. The parameters of the bubble and the surrounding fluid are the same as for Section 5.1.1. We consider the effect of the viscosity ratio, β, on the radius history of the bubble. The radius histories of the bubble over the first oscillation for $\beta = 0.2$, 0.4, 0.6 and 0.8 are given by Figure 5.2.

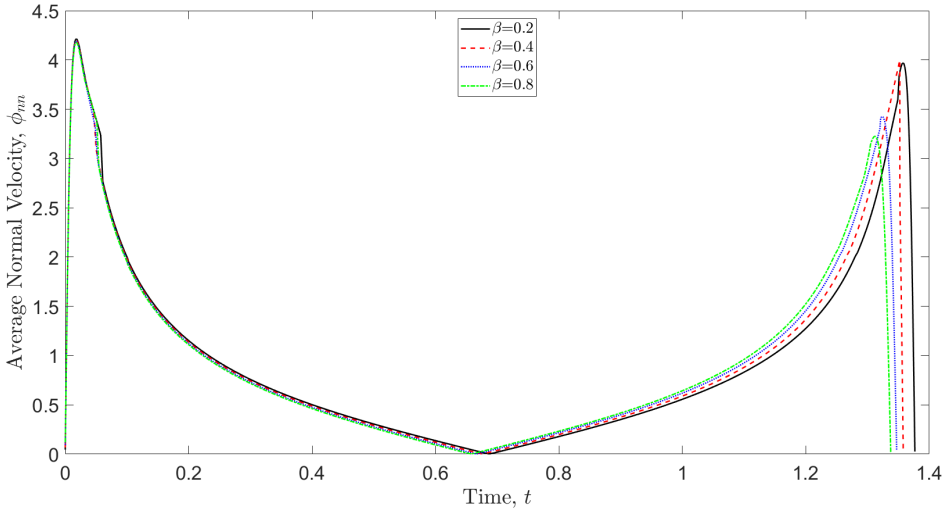


Figure 5.3: The influence of the viscosity ratio, β, on the maximum velocity of a spherical bubble in an infinite Jeffrey fluid over the first oscillation. The remaining parameters are the same as in Figure 5.2.

As shown, as β increases from 0.2 to 0.8, the maximum radius decreases from 0.85 to 0.83. Furthermore, the oscillation time of the bubble decreases from $t = 1.38$ to $t = 1.34$. This is apparent from equations (2.5.23) and (2.5.24). As β increases, the Jeffrey model approaches the Newtonian model and as seen in Chapter 4, a Newtonian fluid has a lower maximum radius and oscillation period as opposed to the purely polymeric non-Newtonian fluid.

Furthermore, a similar result can be shown for the average velocity on the bubble surface. This is shown in Figure 5.3 for $\beta = 0.2$, 0.4, 0.6 and 0.8 once again. As can be seen, an increase in β results in an decrease in the magnitude of the average velocity on the bubble surface from 3.97 to 3.23 which corresponds to a 23% decrease.

Hence, as β increases, the elastic energy stored in the fluid decreases and more energy is allowed to dissipated throughout the fluid resulting in the reduced radius, oscillation time, and average surface velocity.

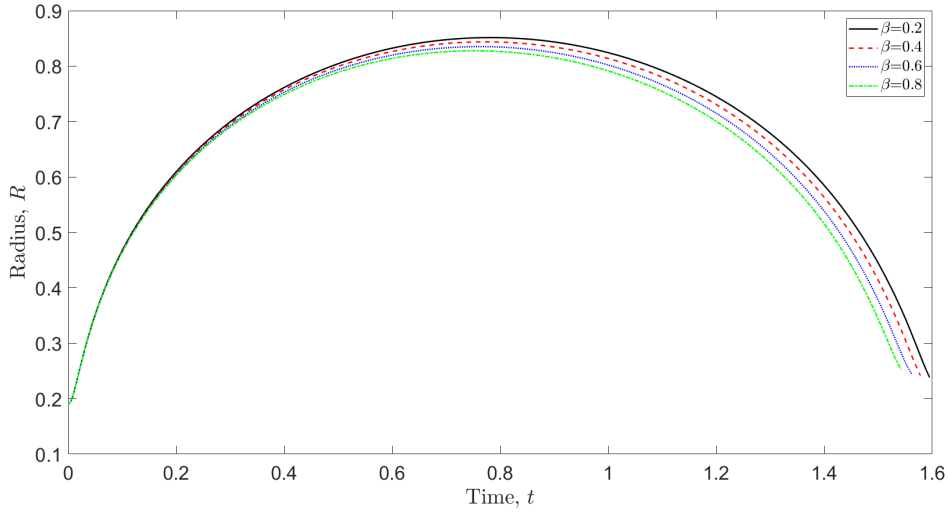


Figure 5.4: The influence of the viscosity ratio, β, on the radius history of a bubble near a wall with stand-off distance $\gamma = 1.0$ in a Jeffrey fluid. The parameters of the surrounding liquid are the same as in Figure 5.2.

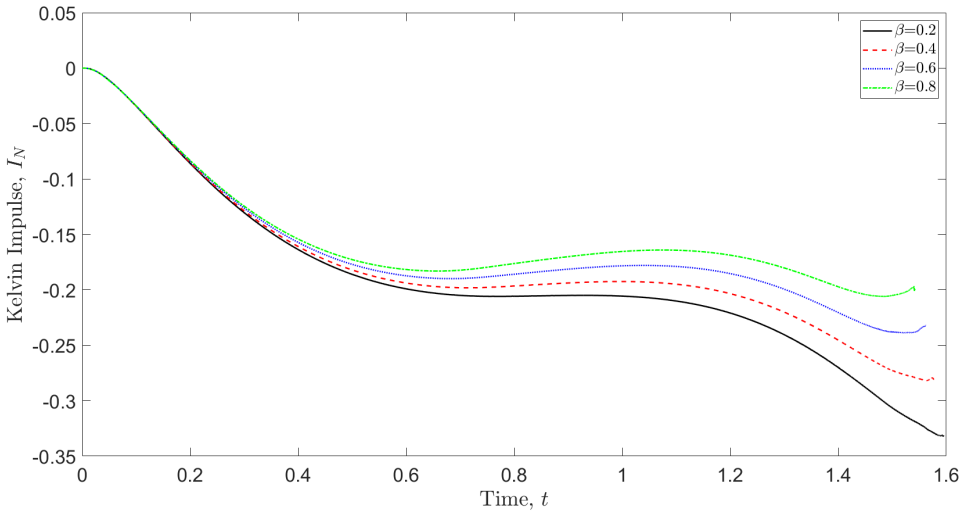


Figure 5.5: The influence of the viscosity ratio, β, on the Kelvin impulse of a bubble near a wall with stand-off distance $\gamma = 1.0$ in a Jeffrey fluid. The parameters of the surrounding liquid are the same as in Figure 5.2.

5.2 Bubble near a flat rigid boundary

Next, we consider the evolution of a microbubble near a flat rigid boundary with stand-off distance, $\gamma = 1.0$. The parameters of the bubble and the surrounding fluid are the same as for Section 5.1.1.

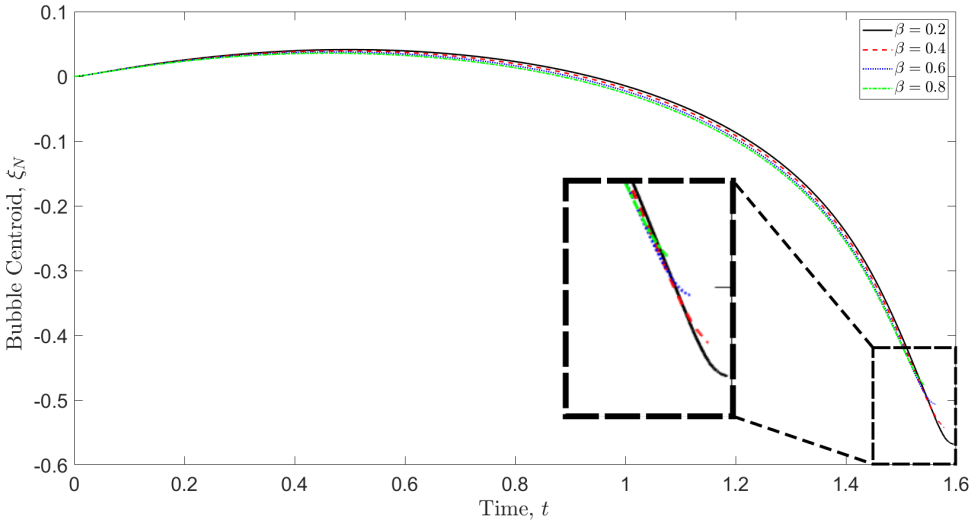


Figure 5.6: The influence of the viscosity ratio, β, on the migration of a bubble near a wall in a Jeffrey fluid. The stand-off distance is given by $\gamma_N = 1.0$ and the location of the wall would correspond to the line $\xi_N = -1.0$. The parameters of the surrounding liquid are the same as in Figure 5.2.

5.2.1 Results on radius history, bubble migration, Kelvin impulse and jet shape

We once again consider the effect of the viscosity ratio, β, on the radius history of the bubble near a rigid wall with stand-off distance $\gamma = 1.0$.

The radius histories of the bubble over the first oscillation near a flat rigid boundary for $\beta = 0.2$, 0.4, 0.6 and 0.8 are given by Figure 5.4. As with the bubble in an infinite Jeffrey fluid, an increase in the viscosity ratio β results in a decrease in the maximum bubble radius from 0.85 to 0.83 for $\beta = 0.2$ and $\beta = 0.8$, respectively. The oscillation time for the bubble also decreases from 1.60 to 1.54 for $\beta = 0.2$ and $\beta = 0.8$, respectively.

With the introduction of a rigid boundary, we can assess the influence of the viscosity ratio, β, on the Kelvin impulse between the bubble an the wall. This is shown in Figure 5.5 for $\beta = 0.2$, 0.4, 0.6, and 0.8. As can be seen, increasing the parameter β results in a decrease in the absolute value of the Kelvin impulse, meaning a greater solvent contribution in the fluid reduces the inertia between the bubble and the wall. At collapse, the absolute Kelvin impulse decreases from 0.33

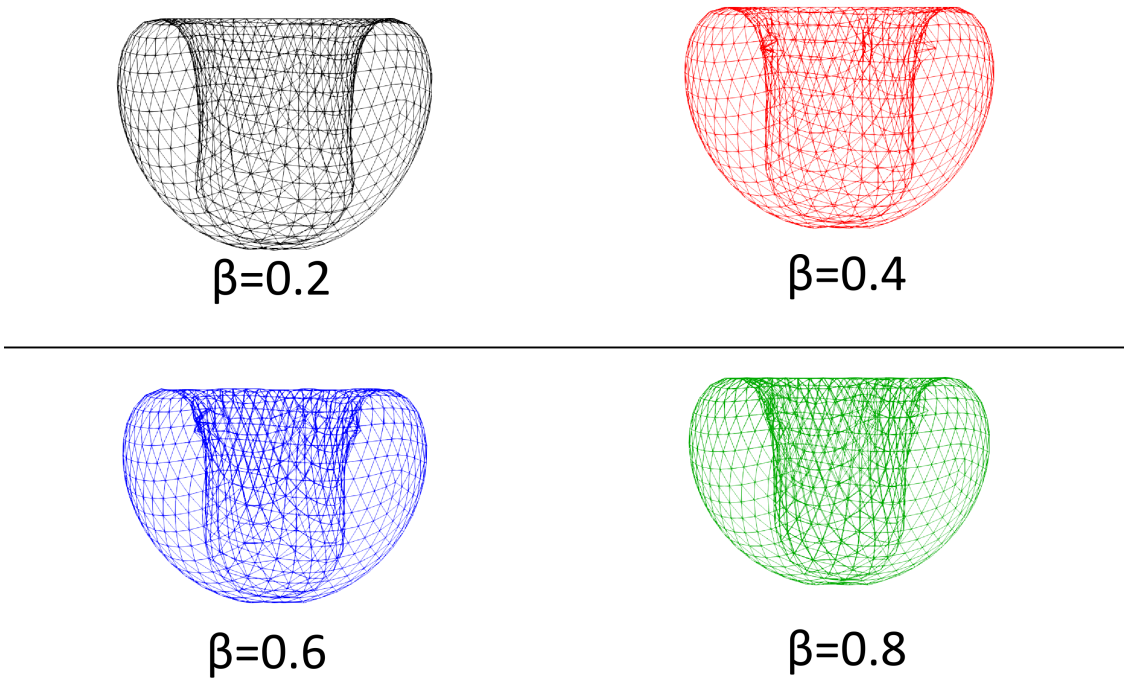


Figure 5.7: The influence of the viscosity ratio, β, on the jet shape of a bubble near a wall with stand-off distance $\gamma = 1.0$ in a Jeffrey fluid. The parameters of the surrounding liquid are the same as in Figure 5.2.

for $\beta = 0.2$ to 0.21 for $\beta = 0.8$, corresponding to a 36% decrease.

As a result of the change in Kelvin impulse, the bubble migration is also affected by the change in viscosity ratio, β. This is shown in Figure 5.6 towards the rigid boundary for $\beta = 0.2$, 0.4, 0.6, and 0.8. It is seen that an increase in the viscosity parameter, β, results in a decrease in the magnitude of the bubble migration towards the wall. This means that an increase in the solvent contribution of the fluid results in a decrease in the wall effects on the bubbles migration.

This decrease in wall effects also becomes apparent when considering the jet profile at collapse. The jet profiles for $\beta = 0.2$, 0.4, 0.6, and 0.8 are given in Figure 5.7. As shown, an increase in β results in the surface of the bubble closest to the wall being further away from the rigid boundary at collapse. Furthermore, increasing the viscosity ratio results in a thinner jet at collapse. This in agreement with the results found in Chapter 4 as an increase in the solvent contribution of the fluid greater

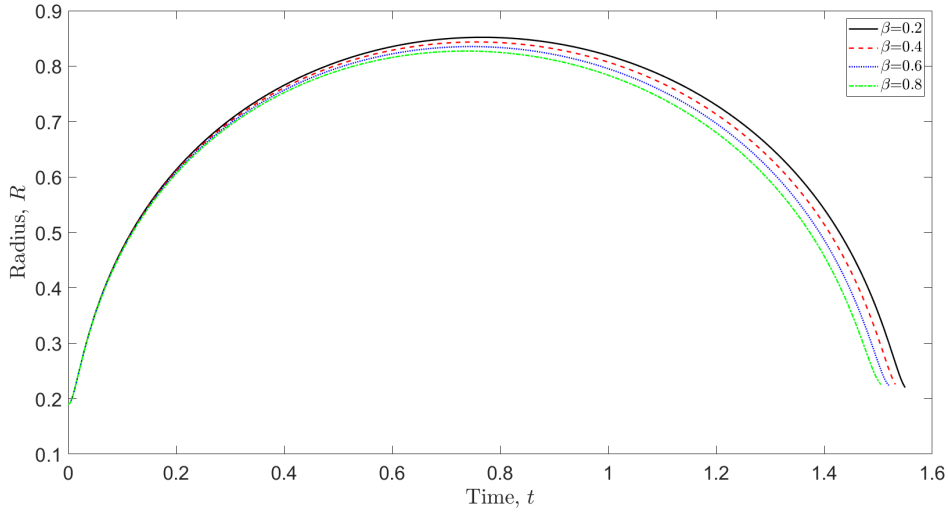


Figure 5.8: The influence of the viscosity ratio, β, on the radius history of a bubble near a wall with stand-off distance $\gamma = 1.25$ in a Jeffrey fluid. The parameters of the surrounding liquid are the same as in Figure 5.2.

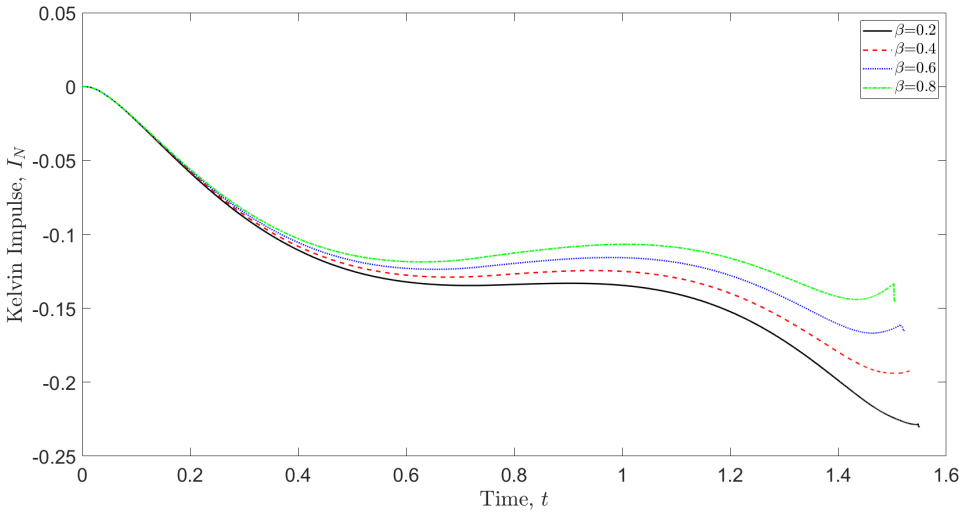


Figure 5.9: The influence of the viscosity ratio, β, on the Kelvin impulse of a bubble near a wall with stand-off distance $\gamma = 1.25$ in a Jeffrey fluid. The parameters of the surrounding liquid are the same as in Figure 5.2.

approximates the Maxwell fluid of corresponding Deborah number, De.

5.2.2 Increased stand-off distance

Next, we consider the evolution of a microbubble near a flat rigid boundary with stand-off distance, $\gamma = 1.25$. The parameters of the bubble and the surrounding

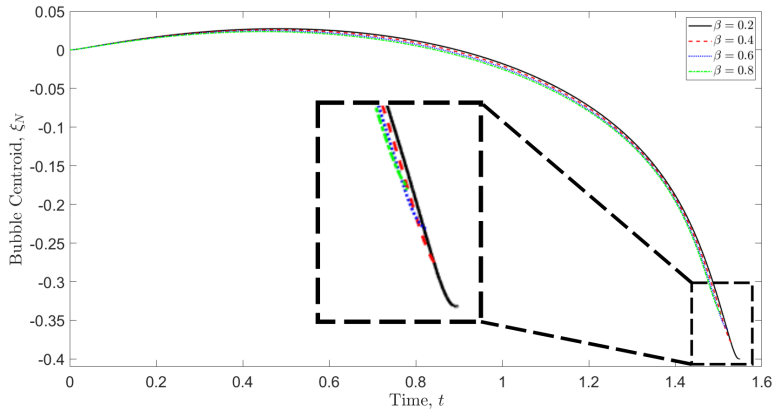


Figure 5.10: The influence of the viscosity ratio, β, on the migration of a bubble near a wall with in a Jeffrey fluid. The stand-off distance is given by $\gamma_N = 1.25$ and the location of the wall would correspond to the line $\xi_N = -1.25$. The parameters of the surrounding liquid are the same as in Figure 5.2.

fluid are once again the same as for Section 5.1.1.

The radius histories of the bubble over the first oscillation near a wall for $\beta = 0.2$, 0.4, 0.6 and 0.8 are given in Figure 5.8. As with the bubble near a wall with stand-off distance, $\gamma = 1.0$, an increase in the viscosity ratio, β, results in a decrease in the maximum bubble radius from 0.85 to 0.83 for $\beta = 0.2$ and 0.8, respectively. As before, the oscillation time for the bubble also decreases from 1.55 for $\beta = 0.2$ to 1.51 for $\beta = 0.8$.

We can once again assess the influence the viscosity ratio, β has on the Kelvin impulse between the bubble and the wall. This is shown in Figure 5.9 for $\beta = 0.2$, 0.4, 0.6, and 0.8. As expected, increasing the parameter β results in a decrease in the absolute value of the Kelvin impulse from 0.23 for $\beta = 0.2$ to 0.15 for $\beta = 0.8$, corresponding to a 35% decrease. Note that the absolute values of the Kelvin impulse are lower at this stand-off distance compared to the reduced stand-off distance as to be expected.

Due to the change in Kelvin impulse, the bubble migration is also affected by the change in viscosity ratio, β as before. This is shown in Figure 5.10 towards the rigid boundary for $\beta = 0.2$, 0.4, 0.6, and 0.8. It is easily seen that an increase in the viscosity ratio, β, results in a decrease in the magnitude of the bubble migration

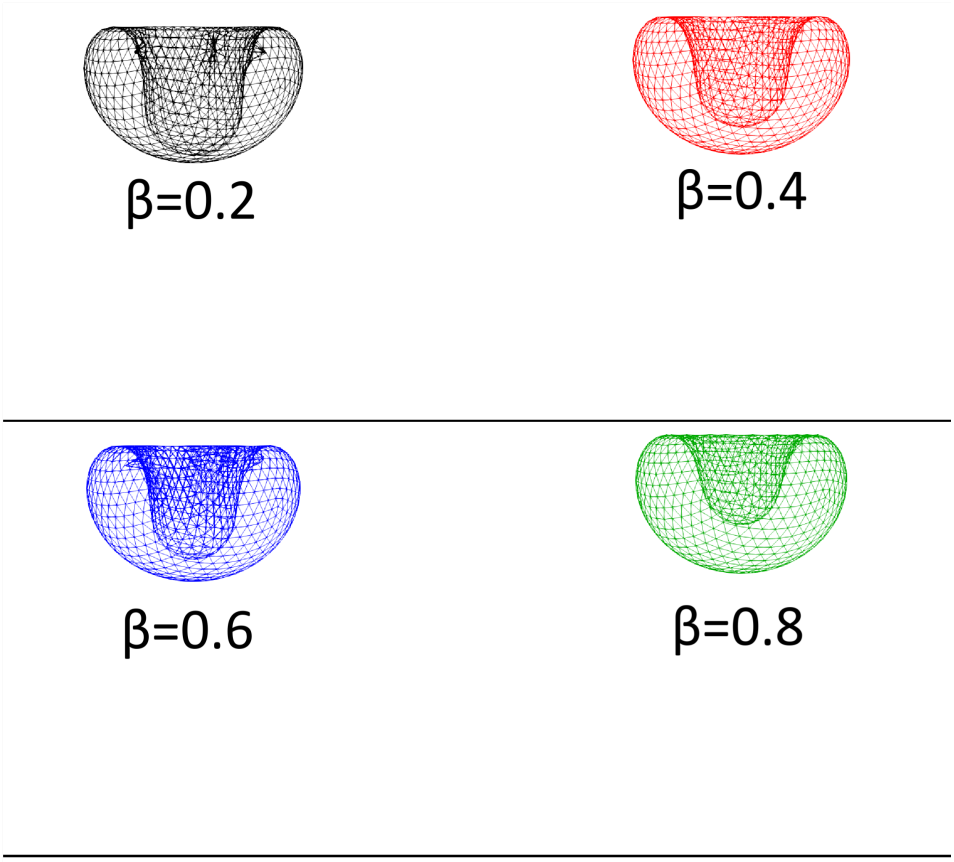


Figure 5.11: The influence of the viscosity ratio, β, on the jet shape of a bubble near a wall with stand-off distance $\gamma = 1.25$ in a Jeffrey fluid. The parameters of the surrounding liquid are the same as in Figure 5.2.

towards the wall.

This decrease in Kelvin impulse and bubble migration is further emphasised when considering the jet profile at collapse. The jet profiles for $\beta = 0.2$, 0.4, 0.6, and 0.8 are given in Figure 5.11. Once again, an increase in β results in the surface of the bubble closest to the wall being further away from the rigid boundary at collapse. Furthermore, increasing the viscosity ratio results in a thinner jet at collapse. This in agreement with the results found for a bubble near a rigid boundary with stand-off distance, $\gamma = 1.0$. Therefore, a greater solvent contribution of the fluid decreases all wall effects resulting in a lower maximum bubble radius, oscillation period, Kelvin impulse and bubble migration, and is consistent for all stand-off distances.

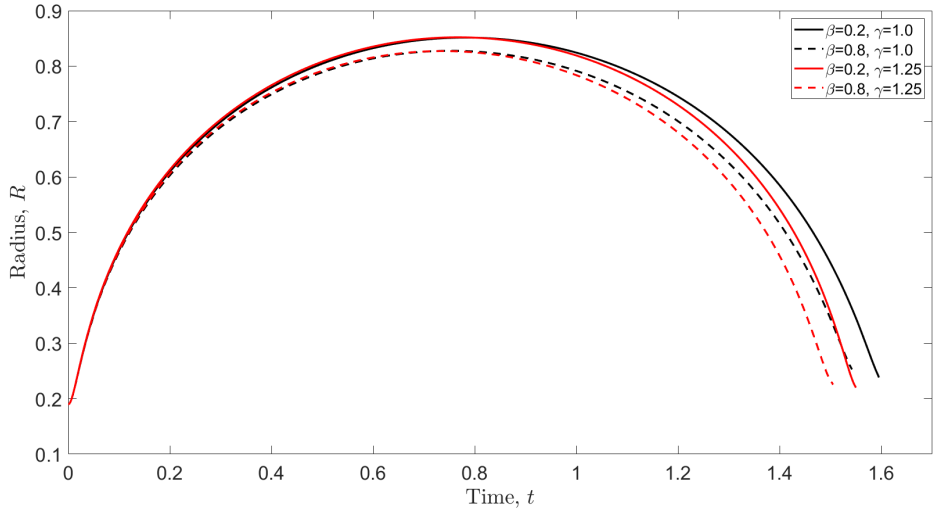


Figure 5.12: The influence of stand-off distance on the radius of a bubble near a flat rigid boundary in a Jeffrey fluid. The remaining parameters are the same as for Figure 5.2.

5.2.3 Effect of stand-off distance

We now look at the effect of increasing the stand-off distance on the influence of the viscosity ratio, β, on the evolution of a bubble. Figure 5.12 shows the radius history for a bubble near a rigid wall of stand-off distances $\gamma = 1.0$ and $\gamma = 1.25$ for viscosity ratios $\beta = 0.2$ and 0.8. As shown, in both cases, the decreases in oscillation time and maximum bubble radius are roughly the same. For $\gamma = 1.0$ the change in maximum radius and oscillation time is 0.02 and 0.05 respectively, and, for $\gamma = 1.25$ the changes are 0.02 and 0.05, respectively. Hence, the influence of β is comparable for any stand-off distance, γ.

5.3 Bubble near a rigid corner

Next, we consider the evolution of a microbubble near a corner of angle, $\alpha = \pi/4$. The parameters of the bubble and the surrounding fluid are the same as for Section 5.1.1 with the stand-off distances from the near and far wall being given by $\gamma_N = 1.0$ and $\gamma_F = 1.5$, respectively.

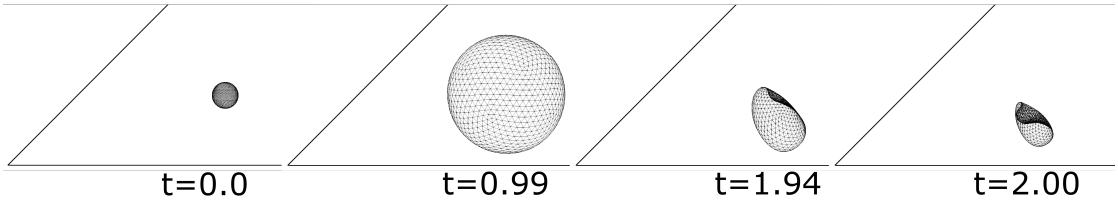


Figure 5.13: The evolution of a three-dimensional bubble near a corner of angle $\alpha = \pi/4$ in a Jeffrey fluid with viscosity ratio $\beta = 0.4$. The remaining parameters are the same as in Figure 5.2.

5.3.1 Evolution of a bubble near a corner in a Jeffrey fluid

We will now look at the bubble profile over expansion and collapse near a corner of angle $\alpha = \pi/4$. The evolution is shown in Figure 5.13. A spherical bubble is initiated near to the corner and time, $t = 0.0$, with stand-off distances towards the near and far wall given by $\gamma_N = 1.0$ and $\gamma_F = 1.5$, respectively. This is shown in the first frame of Figure 5.13. Due to the difference in pressure, the bubble then expands spherically until it reaches it's maximum radius at time, $t = 0.99$. Continuing on, the bubble begins to collapse with the collapse being restricted on the surfaces of the bubble closest to the boundaries. This leads to a jet forming after $t = 1.94$. The jet forms in the upper right-hand side of the bubble whilst the lower surface of the bubble is unable to migrate away from the boundary due to a strong Bjerknes attraction. Continuing into the final frame, the bubble becomes toroidal at $t = 2.00$ and the jet is angled more towards the far boundary whilst the bubble has migrated more towards the near boundary due to the respective initial stand-off distances.

5.3.2 Agreement with previous cases

As with the bubble in an infinite and semi-infinite fluid, we can once again consider the effect of the viscosity ratio, β, on the radius of the bubble near a corner. This is given in Figure 5.14. As before, the radius of the bubbles decreases as β increases from 0.85 to 0.83 for $\beta = 0.2$ and 0.8, respectively. Likewise, the oscillation period also decreases from 2.01 for $\beta = 0.2$ to 1.98 for $\beta = 0.8$.

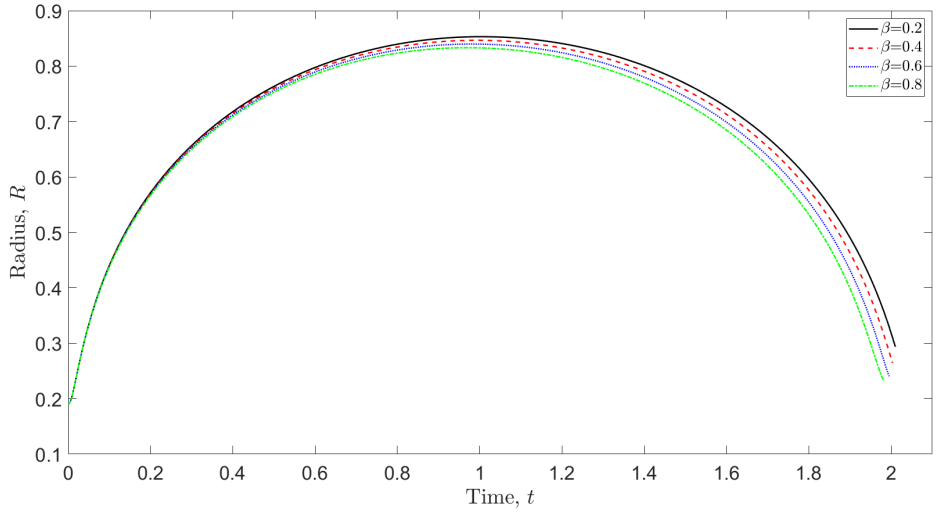


Figure 5.14: The influence of the viscosity ratio, β, on the radius history of a bubble near a corner with stand-off distances $\gamma_N = 1.0$ and $\gamma_F = 1.5$ in a Jeffrey fluid. The parameters of the surrounding liquid are the same as in Figure 5.2.

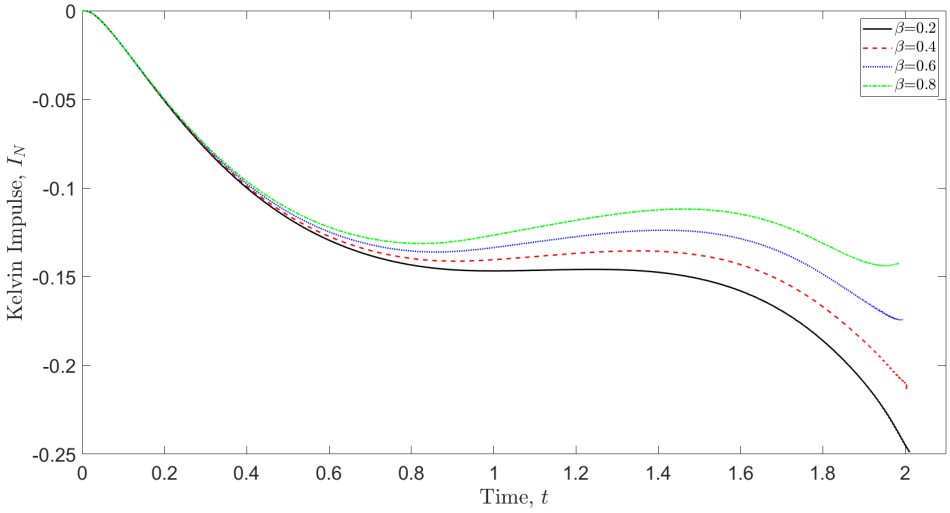


Figure 5.15: The influence of the viscosity ratio, β, on the Kelvin impulse towards the near wall of a bubble near a corner of angle, $\alpha = \pi/4$, with stand-off distances $\gamma_N = 1.0$ and $\gamma_F = 1.5$ in a Jeffrey fluid. The parameters of the surrounding liquid are the same as in Figure 5.2.

With the inclusion of two rigid boundaries to form the corner, we can analyse the effect of the viscosity ratio, β on the Kelvin impulse on the bubble towards both rigid boundaries. The Kelvin impulse towards the near wall is given in Figure 5.15 for $\beta = 0.2$, 0.4, 0.6 and 0.8. As with the case of a bubble near one rigid boundary, the absolute Kelvin impulse decreases as β increases from 0.25 to 0.15 for $\beta = 0.2$

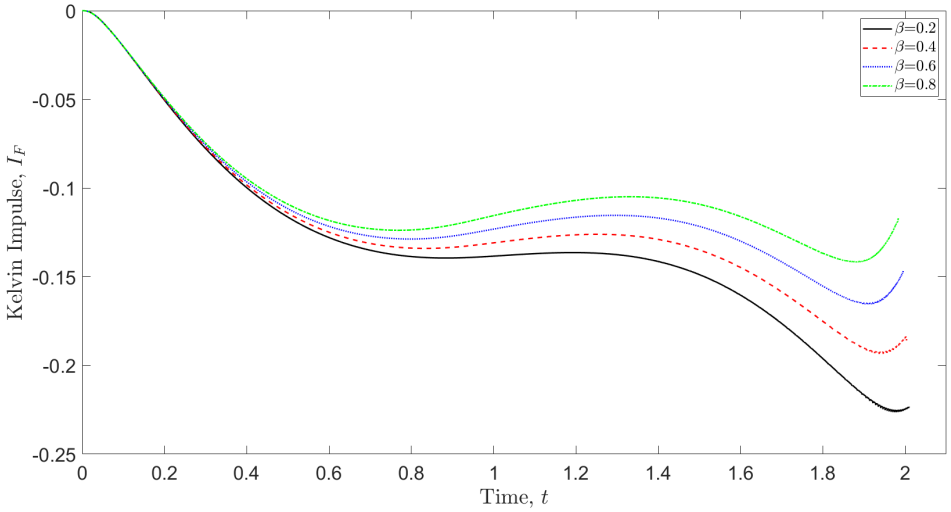


Figure 5.16: The influence of the viscosity ratio, β, on the Kelvin impulse towards the far wall of a bubble near a corner of angle, $\alpha = \pi/4$, with stand-off distances $\gamma_N = 1.0$ and $\gamma_F = 1.5$ in a Jeffrey fluid. The parameters of the surrounding liquid are the same as in Figure 5.2.

and 0.8, respectively, corresponding to a 40% decrease. Note that this is a greater decrease compared to just one rigid boundary. Furthermore, a similar analysis can be done on the Kelvin impulse on the bubble in the direction of the far wall. This is given in Figure 5.16. As with the near wall, an increase in β decreases the absolute Kelvin impulse from 0.22 for $\beta = 0.2$ to 0.11 for $\beta = 0.8$, corresponding to a 50% decrease. Note that the Kelvin impulse is smaller for the far wall because of the greater stand-off distance, as expected. However, the overall decrease in inertia is greater.

The decrease in Kelvin impulse for a bubble near a corner suggest a change in the bubble migration due to the viscosity ratio, β. As with the case with a bubble near a flat rigid boundary, we can analyse the bubble migration towards the near wall but we also have the bubble migration towards the far wall simultaneously. These are given in Figures 5.17 and 5.18, respectively. Once again the bubble migration decreases with an increase in the viscosity ratio, β in both directions meaning the boundary effects on the bubble decrease as β increases. Note that the decrease in bubble migration is greater towards the near wall compared to the far wall. This

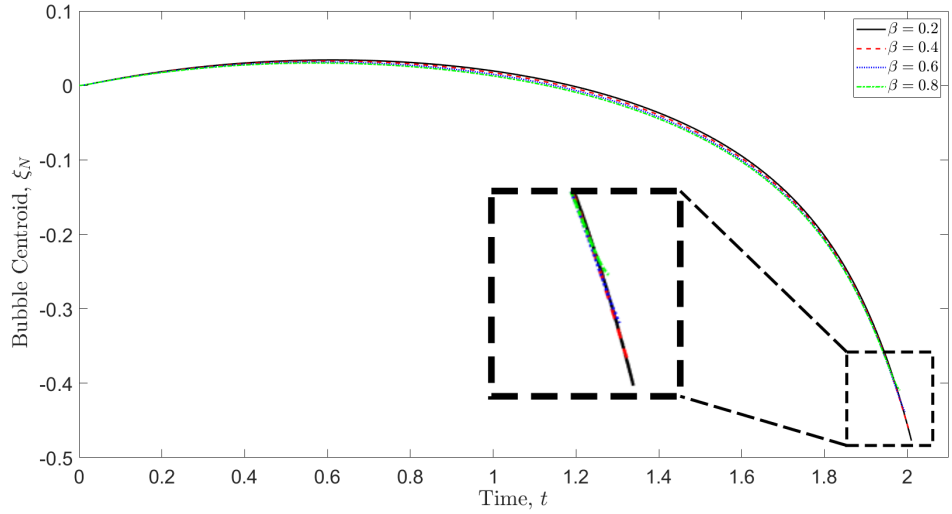


Figure 5.17: The influence of the viscosity ratio, β, on the migration towards the near wall of a bubble near a corner of angle, $\alpha = \pi/4$ in a Jeffrey fluid. The stand-off distance is given by $\gamma_N = 1.0$ and the location of the wall would correspond to the line $\xi_F = -1.0$. The parameters of the surrounding liquid are the same as in Figure 5.2.

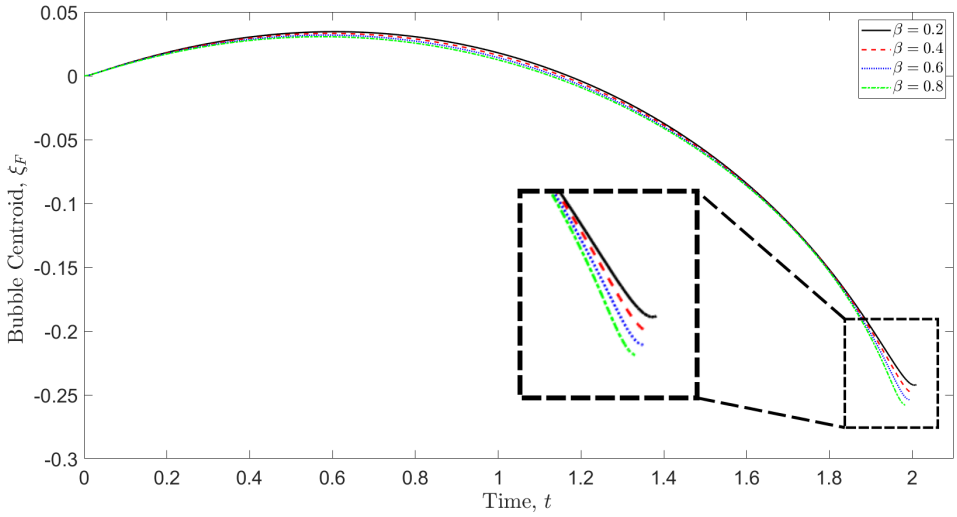


Figure 5.18: The influence of the viscosity ratio, β, on the migration towards the far wall of a bubble near a corner of angle, $\alpha = \pi/4$ in a Jeffrey fluid. The stand-off distance is given by $\gamma_F = 1.5$ and the location of the wall would correspond to the line $\xi_F = -1.5$. The parameters of the surrounding liquid are the same as in Figure 5.2.

is to be expected as the effects of the near boundary are greater on the bubble compared to the far boundary due to their respective stand-off distances.

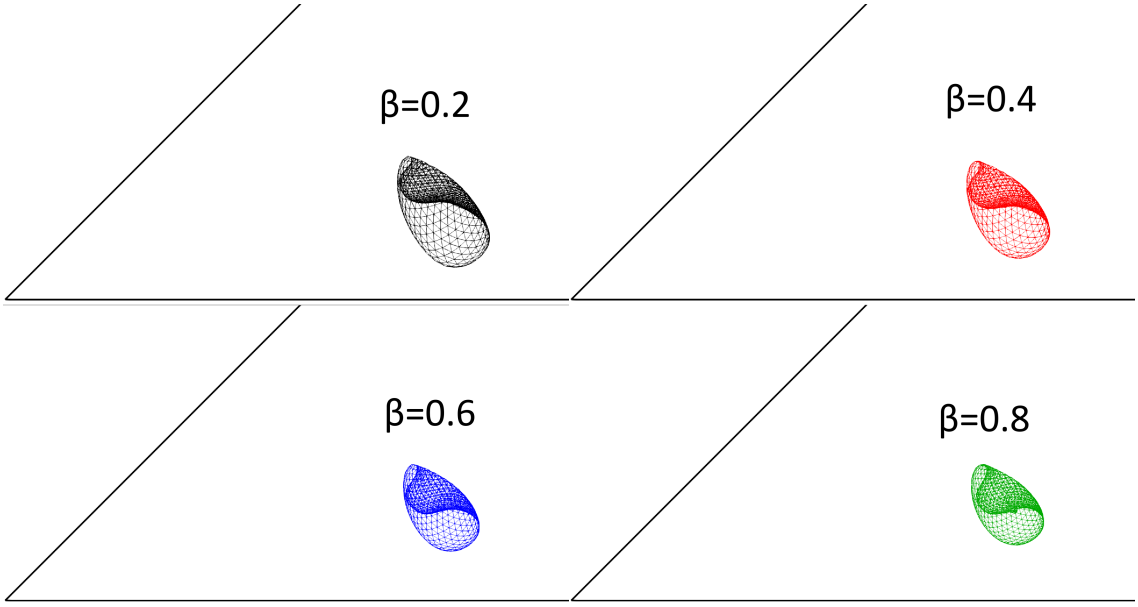


Figure 5.19: The influence of the viscosity ratio, β, on the jet shape of a bubble near a corner of angle, $\alpha = \pi/4$ with stand-off distances $\gamma_N = 1.0$ and $\gamma_F = 1.5$ in a Jeffrey fluid. The parameters of the surrounding liquid are the same as in Figure 5.2.

5.3.3 Results on jet shape and angle at collapse

Now we assess the effect of the viscosity ratio, β, on the jet shape and angle at collapse. The bubble profiles at collapse in various Jeffrey fluids with $\beta = 0.2$, 0.4, 0.6, and 0.8 are given in Figure 5.19. Note firstly, the overall size of the bubble decreases significantly as β increases, which further reiterates the conclusion found in Figure 5.14. Furthermore, as the solvent contribution increases and β increases, the bubble profile at collapse becomes more symmetric. This is clear by comparing the profile for $\beta = 0.2$ and 0.8. The jet once again becomes thinner as β increases which is in agreement with the bubble near one rigid boundary and the jet is angled more towards the near wall as β increases due to the decreased Kelvin impulse towards the far wall. Hence, all boundary effects are diminished as the solvent contribution of the fluid and β increases and the bubble approaches the Newtonian case.

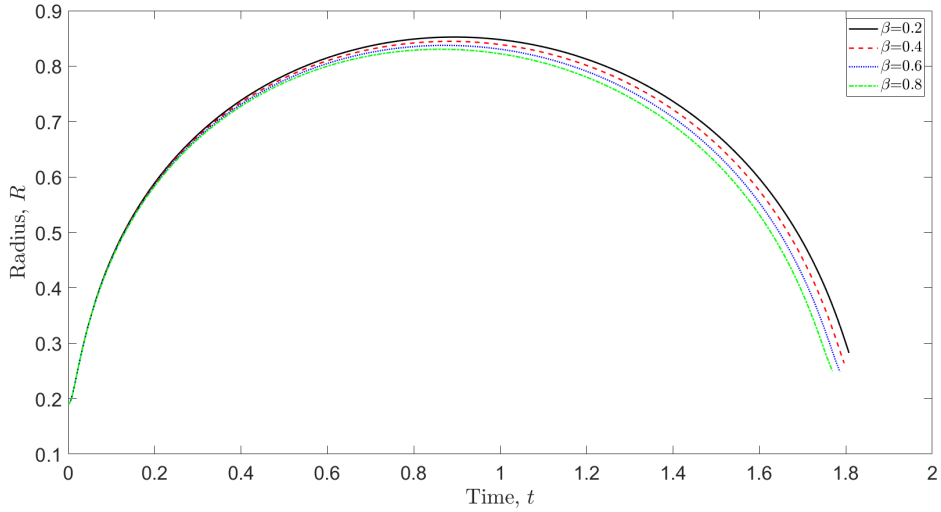


Figure 5.20: The influence of the viscosity ratio, β, on the radius history of a bubble near a corner of angle, $\alpha = \pi/2$ with stand-off distances $\gamma_N = 1.0$ and $\gamma_F = 1.5$ in a Jeffrey fluid. The parameters of the surrounding liquid are the same as in Figure 5.2.

5.3.4 Increased corner angle

We will now look at the bubble evolution over expansion and collapse near a corner of angle $\alpha = \pi/2$ in a Jeffrey fluid with viscosity ratios, $\beta = 0.2$, 0.4, 0.6, and 0.8. The stand-off distances are given by $\gamma_N = 1.0$ and $\gamma_F = 1.5$ for the near and far boundaries, respectively. All other parameters are the same as in Figure 5.1.

In a similar manner to a bubble near a corner of angle, $\alpha = \pi/4$, we can once again consider the effect of the viscosity ratio, β, on the radius of the bubble. This is given in Figure 5.20. As before, the radius of the bubbles decreases as β increases from 0.85 to 0.83 for $\beta = 0.2$ and 0.8 respectively. Likewise, the oscillation period also decreases from 2.01 for $\beta = 0.2$ to 1.98 for $\beta = 0.8$.

The Kelvin impulse on the bubble towards both walls can once again be analysed to see the influence of the viscosity ratio, β, on the apparent inertia between the bubble and the corner. The Kelvin impulse towards the near and far walls are given in Figures 5.21 and 5.22, respectively for $\beta = 0.2$, 0.4, 0.6 and 0.8. As before, the absolute Kelvin impulse towards the near wall decreases as β increases from 0.25 to 0.15 for $\beta = 0.2$ and 0.8 respectively, corresponding to a 40% decrease. Furthermore,

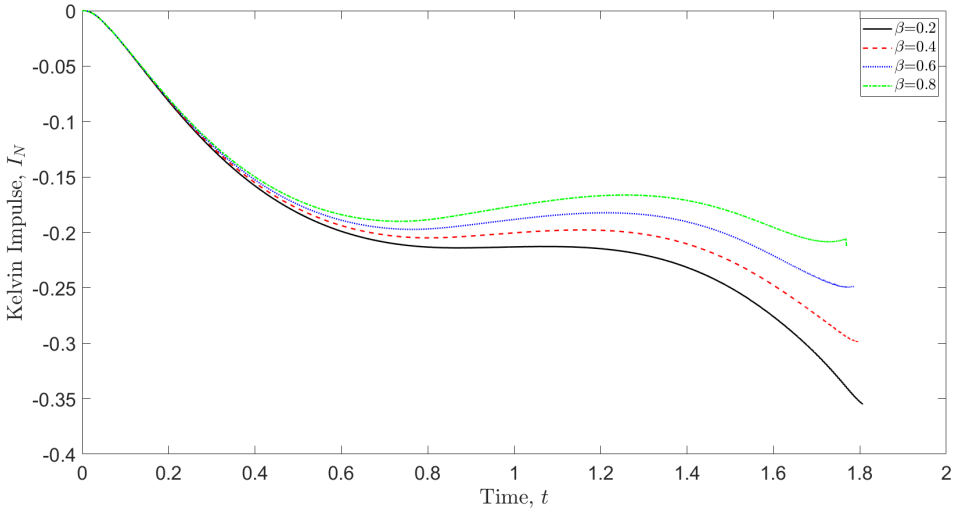


Figure 5.21: The influence of the viscosity ratio, β, on the Kelvin impulse towards the near wall of a bubble near a corner of angle, $\alpha = \pi/2$ with stand-off distances $\gamma_N = 1.0$ and $\gamma_F = 1.5$ in a Jeffrey fluid. The parameters of the surrounding liquid are the same as in Figure 5.2.

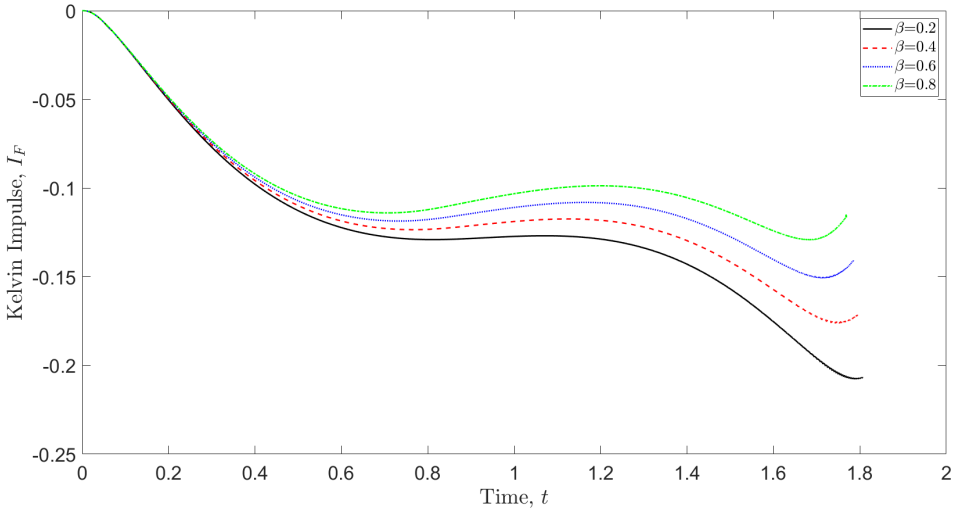


Figure 5.22: The influence of the viscosity ratio, β, on the Kelvin impulse towards the far of a bubble near a corner of angle, $\alpha = \pi/2$ with stand-off distances $\gamma_N = 1.0$ and $\gamma_F = 1.5$ in a Jeffrey fluid. The parameters of the surrounding liquid are the same as in Figure 5.2.

as with the near wall, an increase in β decreases the absolute Kelvin impulse from 0.22 for $\beta = 0.2$ to 0.12 for $\beta = 0.8$, corresponding to a 45% decrease. Note that the Kelvin impulse is smaller for the far wall as expected as the closest surface of the bubble is further away from the boundary compared to the near wall. However,

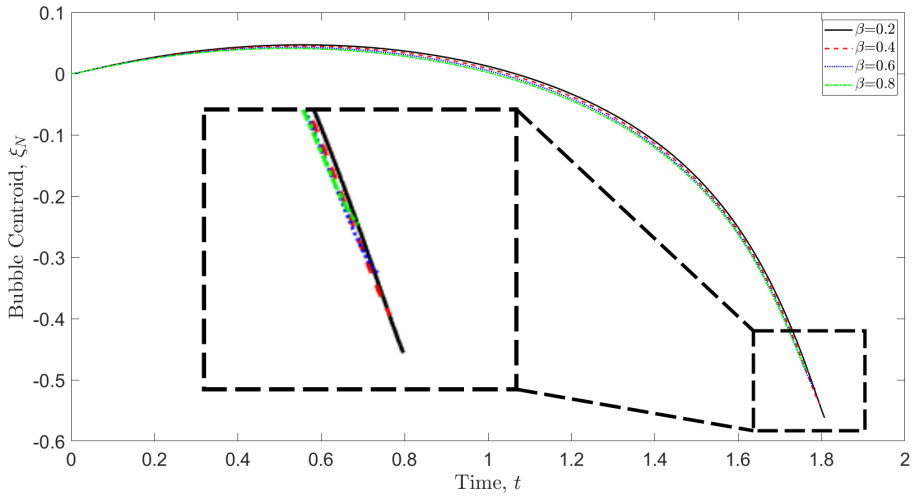


Figure 5.23: The influence of the viscosity ratio, β, on the migration towards the near wall of a bubble near a corner of angle, $\alpha = \pi/2$, in a Jeffrey fluid. The stand-off distance is given by $\gamma_N = 1.0$ and the location of the wall would correspond to the line $\xi_N = -1.0$. The parameters of the surrounding liquid are the same as in Figure 5.2.

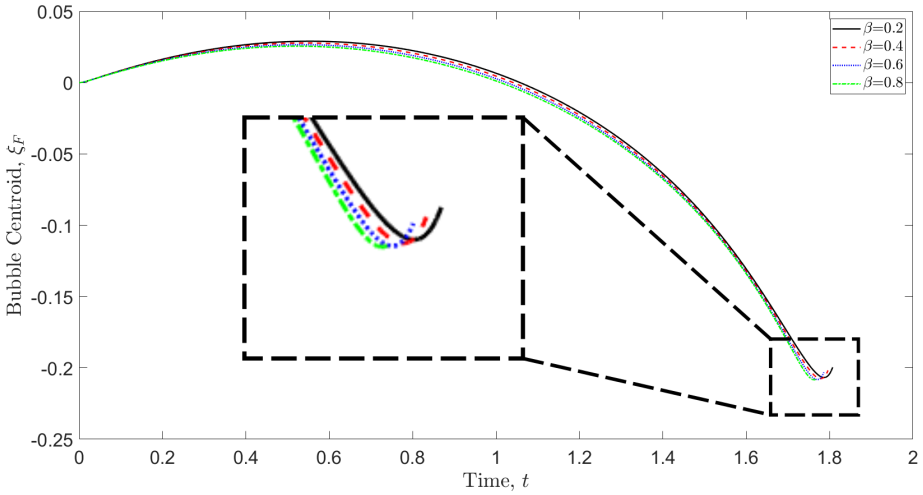


Figure 5.24: The influence of the viscosity ratio, β, on the migration towards the far wall of a bubble near a corner of angle, $\alpha = \pi/2$, in a Jeffrey fluid. The stand-off distance is given by $\gamma_F = 1.5$ and the location of the wall would correspond to the line $\xi_F = -1.5$. The parameters of the surrounding liquid are the same as in Figure 5.2.

the overall decrease in inertia is greater. This is consistent with the smaller corner angle of $\alpha = \pi/4$.

The results on the Kelvin impulse have a direct impact on the bubble migration.

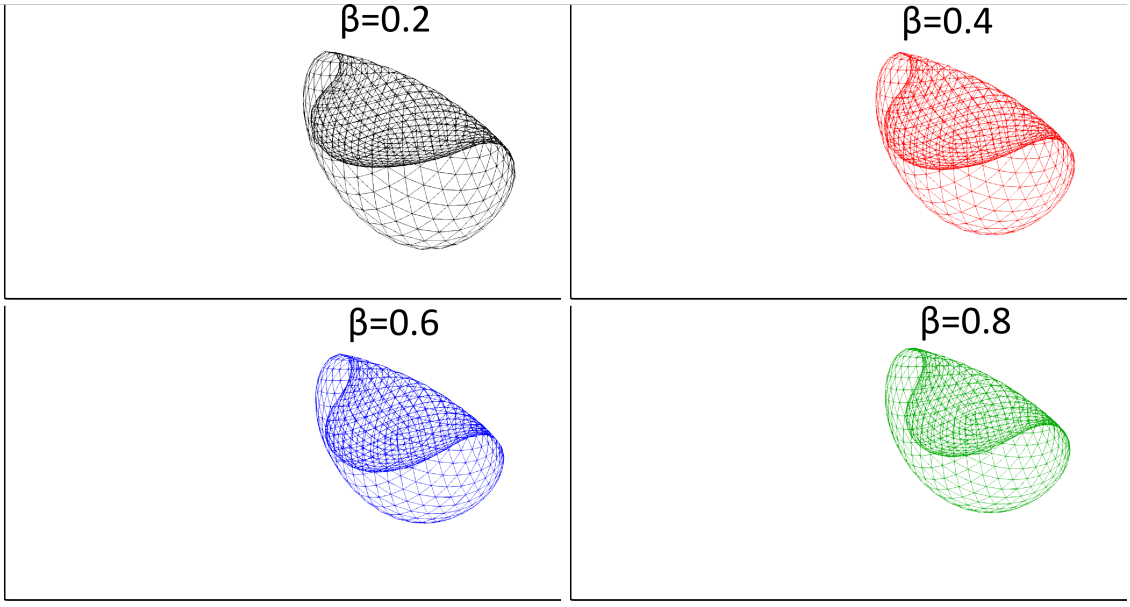


Figure 5.25: The influence of the viscosity ratio, β, on the jet shape of a bubble near a corner of angle, $\alpha = \pi/2$ in a Jeffrey fluid. The parameters of the surrounding liquid are the same as in Figure 5.2.

As with the case with a corner of angle, $\alpha = \pi/4$, we can analyse the bubble migration towards both the near and far walls. These are given in Figures 5.23 and 5.24, respectively. Once again the bubble migration decreases with an increase in the viscosity ratio, β, towards the near boundary meaning the boundary effects on the bubble decrease as β increases in this direction. However, there is little change in the direction of the far boundary for a corner of angle, $\alpha = \pi/2$, due to the increased stand-off distance and larger domain size.

As before we analyse the influence of the viscosity ratio, β, on the jet shape and angle at collapse. The bubble profiles at collapse near a corner of angle, $\alpha = \pi/2$, with $\beta = 0.2$, 0.4, 0.6, and 0.8 are given in Figure 5.25. Once again, the overall size of the bubble is significantly smaller as β increases, which is consistent with the results found in Figure 5.20. Furthermore, as β increases, the bubble profile at collapse becomes more symmetric, meaning that the effects of the far boundary appear to diminish as the solvent contribution of the fluid increases. This is clear by comparing the profile for $\beta = 0.2$ and 0.8. The jet once again becomes thinner as β increases and the jet is angled more towards the near wall as β increases due

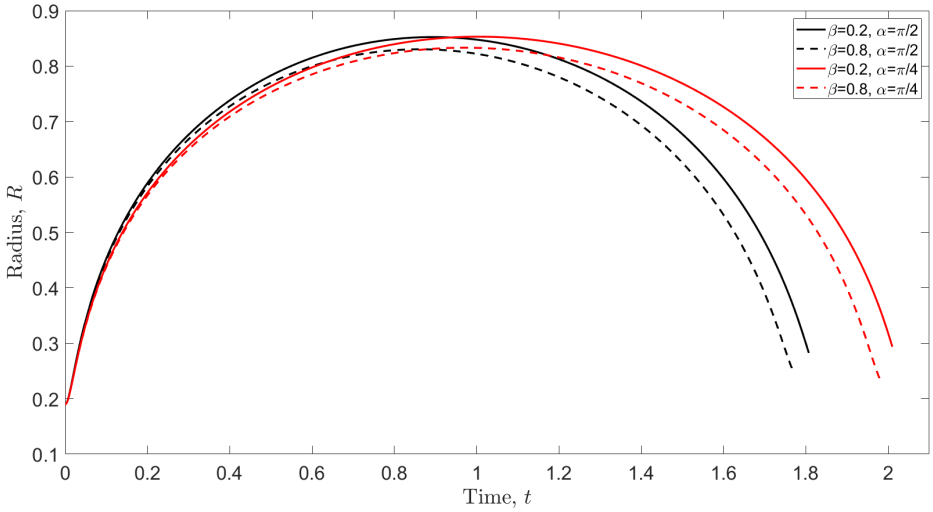


Figure 5.26: The influence of the domain size on the radius history of a bubble in a corner of various angles, α. The remaining parameters of the fluid are the same as in Figure 5.2.

to the decreased Kelvin impulse towards the far wall. This is in agreement with the previous corner study. Hence, all boundary effects are diminished as the solvent contribution of the fluid and β increases and the bubble approaches the Newtonian case. As is clear from the similarities between the results for corners of angles, $\alpha = \pi/4$, and $\alpha = \pi/2$, the domain size has no effect on the overall trends resulting from the influence of β on the bubbles evolution.

5.3.5 Effects on domain size of a bubble in a Jeffrey fluid

We now look at the change in radius history between a Jeffrey fluid of $\beta = 0.2$ and $\beta = 0.8$, for a bubble near a corner of angles $\alpha = \pi/4$ and $\pi/2$. This is shown in Figure 5.26 where the black lines represent $\alpha = \pi/2$ and the red lines represent $\alpha = \pi/4$. As shown, the maximum radius and oscillation period both once again decrease as the viscosity ratio, β, increases as discussed previously. However, restricting the domain size does not change the magnitude of this effect as the change in maximum radius and oscillation period is comparable for both corner angles. The oscillation period overall increases however, as the domain size is restricted (Wang

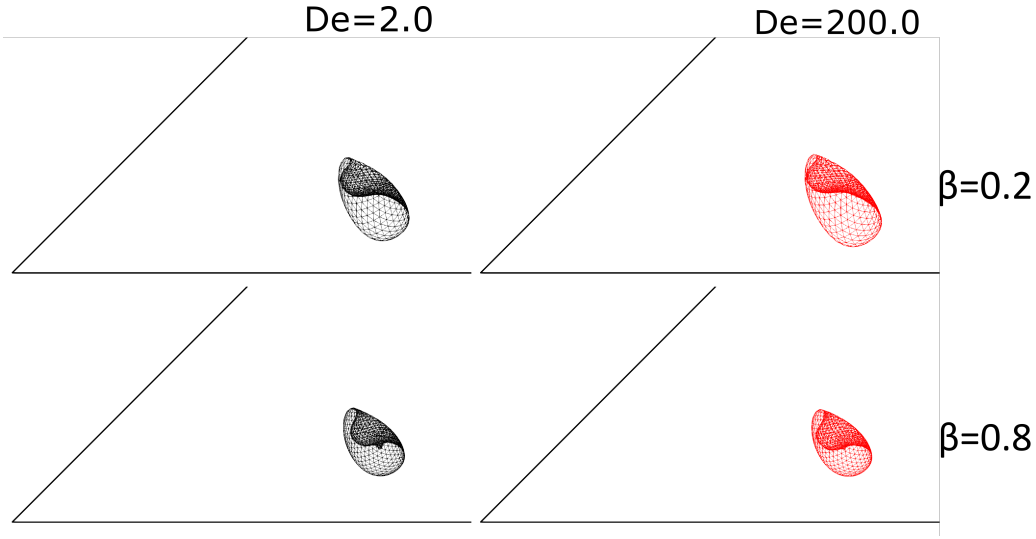


Figure 5.27: The large scale influence of the Deborah number on the jet profile of a bubble initiated in a Jeffrey fluid near a corner of angle $\alpha = \pi/4$. The remaining parameters are the same as in Figure 5.2.

et al. [2020]).

5.3.6 Convergence with Deborah number

We can now discuss the large scale effects of the Deborah number on the evolution of a bubble in a Jeffrey fluid. Figure 5.27 shows the jet shapes for bubbles at collapse in Jeffrey fluids of viscosity ratios, $\beta = 0.2$ and 0.8, with a Deborah number, $De = 2.0$ and 200.0. As shown in Chapter 4, an increase in the Deborah number results in a larger bubble at collapse. A point reiterated in Figure 5.27 for $\beta = 0.2$ which closer represents the pure polymeric fluids shown in Chapter 4. Note however, the comparable size of the bubble at collapse for the bubble in a Jeffrey fluid of viscosity parameter, $\beta = 0.8$. This is due to the fluid closer representing the purely solvent Newtonian fluid where the relaxation time effects become negligible. This means, for larger Deborah numbers, there is a greater change in the maximum bubble radius and wall effects as the polymeric contribution of the fluid increases.

This point is further shown in Figure 5.28 which shows the radius history for the bubbles initiated in differing Jeffrey fluids of Deborah number, $De = 2.0$ and 200.0.

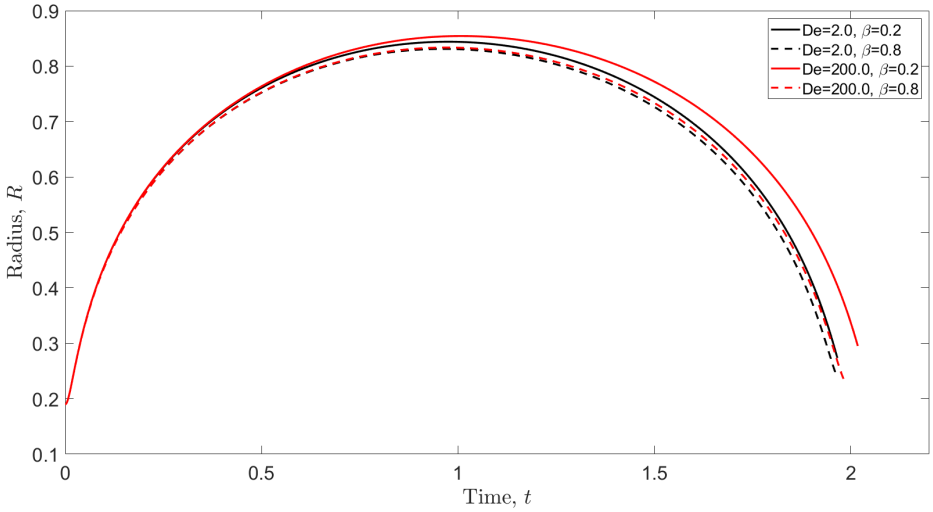


Figure 5.28: The large scale influence of the Deborah number on the radius of a bubble initiated in a Jeffrey fluid near a corner of angle $\alpha = \pi/4$. The remaining parameters are the same as in Figure 5.2.

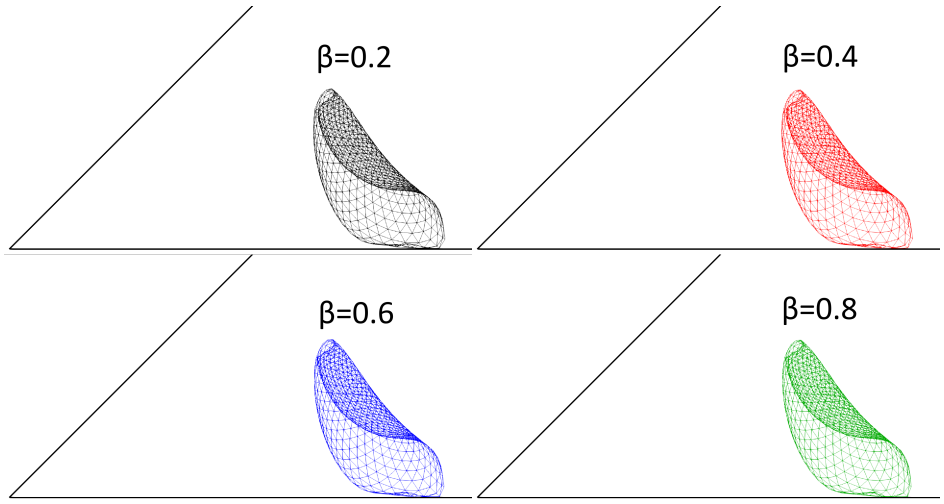


Figure 5.29: The large scale influence of the Reynolds number on the jet profile of a bubble initiated in a Jeffrey fluid near a corner of angle $\alpha = \pi/4$ with $Re = 450$ and initial radius, $R^* = 4.5 \times 10^{-5} m$. The remaining parameters are the same as in Figure 5.2.

As shown, for $De = 2.0$, there is a significantly smaller change in maximum bubble radius and oscillation period compared to the same bubble initiated in a Jeffrey fluid with $De = 200.0$.

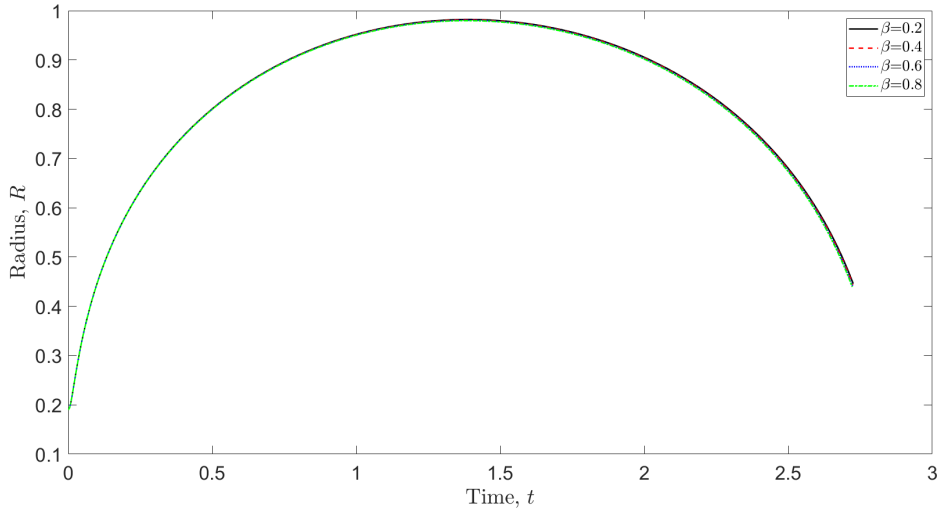


Figure 5.30: The large scale influence of the Reynolds number on the radius of a bubble initiated in a Jeffrey fluid near a corner of angle $\alpha = \pi/4$ with $Re = 450$ and initial radius, $R^* = 4.5 \times 10^{-5} m$. The remaining parameters are the same as in Figure 5.2.

5.3.7 Convergence with Reynolds number

We can now discuss the large scale influence of the Reynolds number on the evolution of a bubble near a rigid corner. Figure 5.29 shows the jet shapes at collapse for a bubble in a Jeffrey fluid of Reynolds number, $Re = 450$ for $\beta = 0.2$, 0.4, 0.6, and 0.8. As shown, at this level of viscosity, the change in polymeric contribution of the fluid makes little to no difference on the collapse of the bubble as all jet profiles are comparable. This is apparent from equations (2.5.23) and (2.5.24), as the viscous effects and viscoelastic effects become negligible as the Reynolds number increases.

This point is further reiterated by looking at the bubble radius in a Jeffrey fluid of Reynolds number $Re = 450$ for $\beta = 0.2$, 0.4, 0.6, and 0.8. This is given in Figure 5.30. As can be seen, and change in the polymeric contribution of the fluid results in little to no change on the bubble history or oscillation time. meaning the viscoelastic effects of the fluid only affect the evolution of a bubble in lower Reynolds number fluids.

5.4 Conclusion

Non-Newtonian fluids are highly beneficial for engineering and biomedical applications with solvent and polymeric contributions of a Jeffrey fluid determining the amount of energy stored or dissipated throughout the flow domain. In this Chapter, a numerical model is described based on the boundary integral method coupled with the Jeffrey constitutive equation. A moderate to high Reynolds number is assumed in the flow domain and thus is irrotational in the bulk with the viscoelastic effects only being applicable in a thin viscous layer at the bubble surface, and approximated only through the normal stress balance at the bubble surface. A backwards Euler method is implemented to iteratively solve the Jeffrey equation for the normal stress tensor. Computations are carried out for a bubble in an infinite fluid, near a flat rigid boundary, and near a corner for various corner angles using the Green's function for the Laplace equation and a method of images for all boundaries.

The numerical model has been validated and excellent agreement with predictions obtained using the corresponding Rayleigh-Plesset equation for spherical bubbles in a non-Newtonian liquid is demonstrated. Viscoelastic effects are studied in terms of the viscosity ratio, β, which is the ratio of solvent viscosity to the total combined solvent and polymeric viscosity. Simulations were performed for $\beta = 0.2$, 0.4, 0.6, and 0.8.

The following new phenomena/features were observed:

1. The maximum radius and oscillation period decrease with the viscosity ratio β. This is due to more elastic energy being stored and released in the viscoelastic fluid for a smaller β and less energy being lost due to viscosity as a smaller β corresponds to a more viscoelastic fluid.

2. The wall effects due to the corner are diminished with a larger β as a result of a decrease in the maximum radius. Bubble migration, Kelvin impulse and oscillation amplitude decrease with β.

3. The bubble jet shape is broader and flatter for a bubble near a rigid boundary or in a corner as β decreases. The bubble jet is inclined to the further boundary when it is in a corner as β decreases.

4. Results converge as the Deborah number decreases as the difference in elastic effects become less dominant compared with the viscous damping effects of the fluid as β is varied.

5. Results converge as the Reynolds number increases as the viscosity of the fluid becomes negligible.

In conclusion, a decreased β greatly enhances the effects of the surrounding boundaries on bubble collapse and provides a broader, flatter jet. This implies that a smaller value of β in the fluid, which corresponds to a greater polymeric contribution to the fluid, will enhance the interactions between a bubble and boundaries or other bubbles. This also suggest that, with certain parameter ranges, elasticity and non-Newtonian fluids may benefit ultrasonic cleaning, therapy and drug delivery. However, as with the Maxwell fluid, certain viscoelastic ranges would result in greater cavitation damage to machinery meaning that a Jeffrey fluid may be favourable over a Maxwell fluid as energy is allowed to dissipate with the inclusion of solvents in the fluid.

CHAPTER 6

CONCLUSION AND DISCUSSION

6.1 Summary

In this thesis, we described the physical and mathematical model for a microbubble near rigid boundaries in various viscoelastic fluids. Potential flow theory was introduced from first principles assuming an irrotational and incompressible flow field. Green's second identity was implemented to provide a solution for the velocity potential, ϕ, on the bubble surface and it's normal derivative, $\partial\phi/\partial n$ on the rigid boundaries, with a Green's function and method of images being used to simulate the image points. Bernoulli's equation was introduced to develop a first order ODE to model the change in velocity potential with time with a kinematic boundary condition updating the bubble surface with time.

The non-Newtonian properties of the fluid were included using both Maxwell's constitutive equation and Jeffrey's constitutive equation which is approximated only through the normal stress balance. Assuming there is a moderate to high Reynolds number, the viscoelastic effects are negligible in the bulk. The viscoelastic effects are not negligible in a thin layer at the bubble surface. In doing so, the effects of the relaxation time, λ_1, and polymeric contribution, β, on the bubble are modelled.

A boundary integral method was then used to implement the above model. The above techniques were implemented using a surface interpolation scheme to com-

pute the bubble surface and potential distribution. A moving least squares method provided the tangential velocity and surface curvature at each node. At each time-step, Lagrangian interpolation updated the normal stress tensor and the velocity potential was computed using a fourth order Runge-Kutte scheme.

The boundary integral method was then validated with experimental data on the bubble profiles for a bubble near a corner with the non-Newtonian Rayleigh-Plesset equations providing validation for the radius history of the bubble.

6.2 Conclusions

Bubble in a Maxwell fluid

The bubble was initiated in an infinite Maxwell fluid, near a rigid boundary and near a corner of angles, $\alpha = \pi/2$ and $\pi/4$, with Deborah numbers, $De = 0.0$, 0.2, 2.0 and 20.0. A pressure difference of $\varepsilon = 100$ was implemented to allow the bubble to expand and then subsequently collapse and induce jet formation. In doing so, the influence of the relaxation time of the fluid on the bubbles evolution was investigated and conclusions were drawn on the effect of viscoelastic fluids in ultrasonic cleaning, drug delivery, and therapy.

We observed that the maximum radius and oscillation period increased with the Deborah number. This was due to more elastic energy being stored and released in the viscoelastic fluid for a larger Deborah number and less energy being lost due to viscosity. As a direct result, the wall effects from the corner were enhanced with a larger De due to the increase in the maximum radius and the bubble migration and oscillation amplitude also increased with the Deborah number. Furthermore, the bubble jet shape was broader and flatter for a bubble near a rigid boundary or in a corner as De increased. The bubble jet was inclined to the further boundary when it was in a corner as De increased. Results converged as Deborah number increased as the elastic effects become dominant compared with the viscous damping effects

of the fluid. Likewise, result converged as the Reynolds number increased as the viscous damping effects became negligible.

Bubble in a Jeffrey fluid

Similarly to the Maxwell model, the bubble was initiated in an infinite Jeffrey fluid, near a rigid boundary and near a corner of angles, $\alpha = \pi/2$ and $\pi/4$. This time, the effect of the total polymeric viscosity of the fluid was investigated, and all simulations were repeated for $\beta = 0.2$, 0.4, 0.6, and 0.8. A pressure difference of $\varepsilon = 100$ was implemented to allow the bubble the expand and then subsequently collapse and induce jet formation. In doing so, the influence of the polymeric viscosity of the fluid on the bubbles evolution was investigated and conclusions were drawn on the effect of viscoelastic fluids in ultrasonic cleaning, drug delivery, and therapy.

We observed that the maximum radius and oscillation period decreased with the viscosity ratio β. This is due to more elastic energy being stored and released in the viscoelastic fluid for a smaller β and less energy being lost due to viscosity as a smaller β corresponds to a more elastic fluid. The wall effects from the corner were diminished with a larger β due to the decrease in the maximum radius and the bubble migration, Kelvin impulse and oscillation amplitude also decreased with β. The bubble jet shape was broader and flatter for a bubble near a rigid boundary or in a corner as β decreased. The bubble jet was inclined to the further boundary when it is in a corner as β decreased. Results converged as the Deborah number decreased as the difference in elastic effects become less dominant compared with the viscous damping effects of the fluid as β was varied. Finally, the results converged as the Reynolds number increased as the viscosity of the fluid became negligible.

In conclusion, an increased Deborah number or decreased viscosity ratio, β, greatly enhances the effects of the surrounding boundaries on bubble collapse and provides a broader, flatter jet. This implies that a higher value of De or a lower value of β in the fluid will enhance the interactions between a bubble and boundaries

or other bubbles. This also suggests that, with certain parameter ranges, elasticity and non-Newtonian fluids may benefit ultrasonic cleaning, therapy and drug delivery. Therefore, by situating the bubbles in viscoelastic fluids rather than Newtonian fluids, better microscopic cleaning and targeted drug delivery can be achieved by changing the polymeric contribution and the relaxation time of the fluid. However, damage to the surrounding surfaces is likely to increase once the rheological properties of the fluid are altered.

6.3 Future work

In general, we can not find a function, ψ, for constitutive equations that satisfies $\nabla \cdot \boldsymbol{T} = \nabla\psi$ for general irrotational flows. However, in other situations we have that $\nabla \times \nabla \cdot \boldsymbol{T} \neq 0$ even though $\nabla \times \boldsymbol{u} = 0$. This means there is an incompatibility in the theory of viscoelastic potential flow. We cannot always find a function ψ satisfying the above equation so that not all fluids will satisfy a Bernoulli equation. For Maxwell's and Jeffrey's constitutive equation, ψ is found to be zero. The admissibility condition can be satisfied in an approximate sense for moderate to large Reynolds numbers since $\nabla \cdot \boldsymbol{T}$ becomes small compared to inertial terms in the momentum equation in the bulk of the flow. Thus, more general models can be employed that provide a more accurate description of viscoelastic effects and also satisfy frame invariance. The restriction to moderate and high Reynolds number flows limits the method to modelling dilute polymer solutions.

6.3.1 Upper-convected Maxwell model

The linear Maxwell model is the simplest model which still provides substantial viscoelastic effects. However, more advanced models exists to analyse the effect of the rheological properties of the fluid on the evolution of a bubble. Investigations have been carried out in an upper-convected Maxwell fluid showing the highly oscillatory

behaviours for moderate to high Deborah numbers (Kim [1994]). Numerical studies have also been conducted on spherical bubbles using a modified Rayleigh-Plesset equation (Naude and Mendez [2008]). The bubbles seem to expand faster but collapse at lower speeds meaning the influence of an upper-convected Maxwell fluid can reduce the chance of catastrophic collapse and reduce cavitation damage. However, certain Deborah parameter ranges can lead to clear chaotic behaviour. Upon further investigation, it can also be shown that upper-convective Maxwell fluids provide more damping effects and reduces jet velocities at collapse (Lind [2010]). This becomes apparent when considering the following model, which includes an additional viscous term.

For the upper-convected Maxwell model, the normal stress tensor is computed using

$$\boldsymbol{T}^* + \lambda_1 \overset{\nabla}{\boldsymbol{T}}^* = 2\mu_L \dot{\boldsymbol{\gamma}}^*, \tag{6.3.1}$$

where the upper time derivative, $\overset{\nabla}{\boldsymbol{T}}^*$, is given by

$$\overset{\nabla}{\boldsymbol{T}}^* = \frac{D\boldsymbol{T}^*}{Dt^*} - \nabla^* \boldsymbol{u}^* \cdot \boldsymbol{T}^* - \boldsymbol{T}^* \cdot \nabla^* \boldsymbol{u}^*. \tag{6.3.2}$$

When nondimensionalising and evaluating in the normal direction, Maxwell's upper-convected constitutive equation is given by

$$De\Big(\frac{DT_{nn}}{Dt} - 2T_{nn}\frac{\partial^2 \phi}{\partial n^2}\Big) + T_{nn} = \frac{2}{Re}\frac{\partial^2 \phi}{\partial n^2}, \tag{6.3.3}$$

a model for which the three-dimensional effects on the bubble have not been readily investigated. However, the issue with the inclusion of the additional viscous term, $2T_{nn}\partial^2\phi/\partial n^2$, is that the numerical scheme used to solve it, be it backwards Euler method or Runge-Kutta scheme, will generate an additional matrix equation at each time-step. This will drastically increase the running time compared to the linear Maxwell model. An additional issue arises due to the 'tail-like' cusps created in rising

bubbles in upper-convected Maxwell fluids (Lind [2010]). This is because the sharp meshing required to accurately predict this unique bubble shape is highly unstable for three-dimensional meshing, but is very achievable for axisymmetric modelling.

6.3.2 Oldroyd-B model

In a similar manner to the Maxwell and Jeffrey model, there is an extension to the upper-convected Maxwell model where the fluid is once again divided into it's solvent and polymeric contributions. This model is called the Oldroyd-B model. The Oldroyd-B model has been seen to provide accurate predictions for the flow of Boger fluids, which have a constant viscosity for a range of shear rates (Owens and Phillips [2002]). Like the upper-convected Maxwell model, many spherical viscoelastic studies have been conducted on the Oldroyd B model (Fogler and Goddard [1971], Allen and Roy [2000]) and for Rayleigh-Taylor instabilities in viscoelastic drops (Joseph et al. [2002]). Numerical solutions to the Oldroyd-B model have been studied using a finite element method for rising axisymmetric bubbles with a three-dimensional mesh (Pillapakkam et al. [2007]). They observed the aforementioned cusp and negative wake in the flow field.

The normal stress tensor for the Oldroyd-B model is given by

$$T_{nn} = \frac{2\beta}{Re}\frac{\partial^2 \phi}{\partial n^2} + \tau_{nn}, \tag{6.3.4}$$

with

$$De\Big(\frac{D\tau_{nn}}{Dt} - 2\tau_{nn}\frac{\partial^2 \phi}{\partial n^2}\Big) + \tau_{nn} = \frac{2(1-\beta)}{Re}\frac{\partial^2 \phi}{\partial n^2}, \tag{6.3.5}$$

where once again, the three-dimensional effects on the bubble have not been thoroughly investigated. Note that the problems faced with numerically modelling the upper-convected Maxwell model with a three-dimensional mesh are also apparent when modelling the Oldroyd-B viscoelastic fluid, i.e, the increased running time and mesh smoothing issues around the cusp.

6.3.3 Surfactants and shear stress

Recent work has been conducted on the effect of surfactants on the shear stress experienced by surrounding rigid boundaries (Corbett [2023]). The studies show that the inclusion of surfactants in the surrounding fluid, greatly increases the shear stress generated on the rigid boundaries. Hence, the properties of the fluid can lead to more efficient ultrasonic cleaning (Awad and Awad [2022]). This is because, the presence of a surfactant at the bubble surface can alter the effects of surface tension (Chang and Franses [1995]). The change in surface tension can lead to a higher surface velocity and increased wall effects.

The governing equation for a surfactant at a free-surface is given by the Frumkin equation of state and modelled through the surface tension term (Frumkin [1925], Taylor et al. [2003]). This is given by,

$$\sigma = \sigma_0 + \Gamma_\infty R_g T \log\left(\frac{\Gamma_\infty - \Gamma}{\Gamma_\infty}\right) + B\Gamma^2, \tag{6.3.6}$$

where σ_0 is the surface tension in the absence of a surfactant, Γ_0 is the maximum packing concentration of surfactant, R_g is the universal gas constant, T is the temperature, Γ is the concentration of the surfactant at the bubble surface, and B is the parameter of molecular interaction.

Equation (6.3.6) can be easily implemented into the three-dimensional BIM model. However, the issue arises when maintaining a sufficiently smooth mesh whilst the bubble oscillates with it's corresponding shape mode. A phenomenon that has only been achieved for axisymmetric bubbles due to the need to simulate multiple cycles of oscillation. Furthermore, a field grid will have to be implemented to model the tangential velocity on the rigid boundaries and the pressure in the field. A technique that has already been readily established for the 3D BIM code (Mahmud [2017]), but drastically increases the running time of the code. The inclusion of an acoustic wave to induce shape mode oscillations with viscoelastic effects

being present could also lead to numerical instabilities and would require delicate mesh smoothing to maintain an accurate bubble profile over the entire oscillation period.

However, this work could provide insightful research into the non-symmetric shear stresses that can occur at more complex rigid boundaries when the bubble no longer remains spherical or axisymmetric. Furthermore, the inclusion of viscoelastic effects could enhance the shear stress on the wall as we have already shown that an increased relaxation time greatly increases wall effects. Hence, the research could provide great analysis on improving ultrasonic cleaning.

LIST OF REFERENCES

A A Ali and R Makhloufi. Linear and nonlinear rheology of an aqueous concentrated system of cethyltrimethylammonium chloride and sodium salicylate. *Physical Review E*, 56(4):4474, 1997.

J S Allen and R A Roy. Dynamics of gas bubbles in viscoelastic fluids. i. linear viscoelasticity. *The Journal of the Acoustical Society of America*, 107(6):3167–3178, 2000.

T Annable, R Buscall, R Ettelaie, P Shepherd, and D Whittlestone. Influence of surfactants on the rheology of associating polymers in solution. *Langmuir*, 10(4): 1060–1070, 1994.

S B Awad and N F Awad. The role of surfactants in ultrasonic cleaning: Nanoparticle removal and other challenging applications. In *Surfactants in Precision Cleaning*, pages 227–271. Elsevier, 2022.

George Keith Batchelor. *An introduction to fluid dynamics*. Cambridge university press, 1967.

T B Benjamin and A T Ellis. The collapse of cavitation bubbles and the pressures thereby produced against solid boundaries. *Philosophical Transactions for the Royal Society of London. Series A, Mathematical and Physical Sciences*, pages 221–240, 1966.

J Best and J Blake. An estimate of the Kelvin impulse of a transient cavity. *Journal of Fluid Mechanics*, 261:75–93, 1994.

J Best and A Kucera. A numerical investigation of non-spherical rebounding bubbles. *Journal of Fluid Mechanics*, 245:137–154, 1992.

R Bird, R Armstrong, and O Hassager. Dynamics of polymeric liquids. vol. 1: Fluid mechanics. *Journal of non-Newtonian fluid mechanics*, 30, 1987.

J Blake. The Kelvin impulse: Application to cavitation bubble dynamics. *The ANZIAM Journal*, 30(2):127–146, 1988.

J Blake and D Gibson. Cavitation bubbles near boundaries. *Annual review of fluid mechanics*, 19(1):99–123, 1987.

J Blake, G Keen, R Tong, and M Wilson. Acoustic cavitation: the fluid dynamics of non–spherical bubbles. *Philosophical Transactions of the Royal Society of London. Series A: Mathematical, Physical and Engineering Sciences*, 357(1751):251–267, 1999.

JM Boulton-Stone and JR Blake. Gas bubbles bursting at a free surface. *Journal of Fluid Mechanics*, 254:437–466, 1993.

E Brujan, A Al-Hussany, R Williams, and P Williams. Cavitation erosion in polymer aqueous solutions. *Wear*, 264(11-12):1035–1042, 2008.

E Brujan, T Noda, A Ishigami, T Ogasawara, and H Takahira. Dynamics of laser-induced cavitation bubbles near two perpendicular rigid walls. *Journal of Fluid Mechanics*, 841:28–49, 2018.

E-A Brujan. Shock wave emission and cavitation bubble dynamics by femtosecond optical breakdown in polymer solutions. *Ultrasonics Sonochemistry*, 58:104694, 2019.

E A Brujan, G S Keen, A Vogel, and J R Blake. The final stage of the collapse of a cavitation bubble close to a rigid boundary. *Physics of fluids*, 14(1):85–92, 2002.

H Buckland, I Masters, J Orme, and T Baker. Cavitation inception and simulation in blade element momentum theory for modelling tidal stream turbines. *Proceedings of the Institution of Mechanical Engineers, Part A: Journal of Power and Energy*, 227(4):479–485, 2013.

T J Bulat. Macrosonics in industry: 3. ultrasonic cleaning. *Ultrasonics*, 12(2):59–68, 1974.

A Carson, C McTiernan, L Lavery, A Hodnick, M Grata, X Leng, J Wang, X Chen, R Modzelewski, and F Villanueva. Gene therapy of carcinoma using ultrasound-targeted microbubble destruction. *Ultrasound in medicine & biology*, 37(3):393–402, 2011.

M E Cates. Flow behaviour of entangled surfactant micelles. *Journal of Physics: Condensed Matter*, 8(47):9167, 1996.

G Chahine, A Kapahi, J Choi, and C Hsiao. Modeling of surface cleaning by cavitation bubble dynamics and collapse. *Ultrasonics sonochemistry*, 29:528–549, 2016.

C H Chang and E I Franses. Adsorption dynamics of surfactants at the air/water interface: a critical review of mathematical models, data, and mechanisms. *Colloids and Surfaces A: Physicochemical and Engineering Aspects*, 100:1–45, 1995.

H Chmiel and E Walitza. On the rheology of human blood and synovial fluids. *Research Studies, Chicester*, 1980.

C Corbett. *A numerical study of the shape mode oscillation of microbubbles in a viscous compressible liquid*. PhD thesis, University of Birmingham, 2023.

C Coussios and R Roy. Applications of acoustics and cavitation to noninvasive therapy and drug delivery. *Annu. Rev. Fluid Mech.*, 40:395–420, 2008.

J Cui, Z P Chen, Q Wang, T R Zhou, and C Corbett. Experimental studies of bubble dynamics inside a corner. *Ultrasonics Sonochemistry*, 64:104951, 2020.

A Ellis. Some effects of macromolecules on cavitation inception and noise. Technical report, California Inst of Tech Pasadena Div of Engineering and Applied Science, 1967.

P Fischer and H Rehage. Rheological master curves of viscoelastic surfactant solutions by varying the solvent viscosity and temperature. *Langmuir*, 13(26):7012–7020, 1997.

H S Fogler and J D Goddard. Oscillations of a gas bubble in viscoelastic liquids subject to acoustic and impulsive pressure variations. *Journal of Applied Physics*, 42(1):259–263, 1971.

M I Fomitchev-Zamilov. Cavitation-induced fusion: Proof of concept. *19th Natural Philosophy Alliance Proceedings*, page 167, 2012.

S Fong, E Klaseboer, and B Khoo. Interaction of microbubbles with high intensity pulsed ultrasound. *The Journal of the Acoustical Society of America*, 123(3): 1784–1793, 2008.

D Fraggedakis, M Pavlidis, Y Dimakopoulos, and J Tsamopoulos. On the velocity discontinuity at a critical volume of a bubble rising in a viscoelastic fluid. *Journal of Fluid Mechanics*, 789:310–346, 2016.

X Frank, J Charpentier, F Canneviere, N Midoux, and H Li. Bubbles in non-Newtonian fluids: A multiscale modeling. *Oil & Gas Science and Technology–Revue d'IFP Energies nouvelles*, 68(6):1059–1072, 2013.

A N Frumkin. Surface tension curves of higher fatty acids and the equation of condition of the surface layer. *Z. phys. Chem*, 116:466–484, 1925.

R Gaudron, M Warnez, and E Johnsen. Bubble dynamics in a viscoelastic medium with nonlinear elasticity. *Journal of Fluid Mechanics*, 766:54–75, 2015.

S Gonzalez-Avila, A van Blokland, Q Zeng, and C Ohl. Jetting and shear stress enhancement from cavitation bubbles collapsing in a narrow gap. *Journal of Fluid Mechanics*, 884, 2020.

R Han, S Li, AM Zhang, and QX Wang. Modelling for three dimensional coalescence of two bubbles. *Physics of Fluids*, 28(6):062104, 2016.

M Holt. Underwater explosions. *Annual review of fluid mechanics*, 9(1):187–214, 1977.

C F Hung and J J Hwangfu. Experimental study of the behaviour of mini-charge underwater explosion bubbles near different boundaries. *Journal of Fluid Mechanics*, 651:55–80, 2010.

D Joseph and T Liao. Potential flows of viscous and viscoelastic fluids. *Journal of Fluid Mechanics*, 265:1–23, 1994.

D D Joseph, G S Beavers, and T Funada. Rayleigh–taylor instability of viscoelastic drops at high weber numbers. *Journal of Fluid Mechanics*, 453:109–132, 2002.

S Kaul. Microbubbles and ultrasound: a bird's eye view. *Transactions of the American Clinical and Climatological Association*, 115:137, 2004.

J Kennedy. High-intensity focused ultrasound in the treatment of solid tumours. *Nature reviews cancer*, 5(4):321–327, 2005.

C Kim. Collapse of spherical bubbles in maxwell fluids. *Journal of non-newtonian fluid mechanics*, 55(1):37–58, 1994.

E Klaseboer, B Khoo, and K Hung. Dynamics of an oscillating bubble near a floating structure. *Journal of Fluids and Structures*, 21(4):395–412, 2005.

K Kooiman, M Böhmer, M Emmer, H Vos, C Chlon, W Shi, C Hall, S de Winter, K Schroën, M Versluis, et al. Oil-filled polymer microcapsules for ultrasound-mediated delivery of lipophilic drugs. *Journal of controlled release*, 133(2):109–118, 2009.

H Lamb. *Hydrodynamics*. University Press, 1924.

W Lauterborn and H Bolle. Experimental investigations of cavitation-bubble collapse in the neighbourhood of a solid boundary. *Journal of Fluid Mechanics*, 72 (2):391–399, 1975.

W Lauterborn and T Kurz. Physics of bubble oscillations. *Reports on progress in physics*, 73(10):106501, 2010.

M Lee, E Klaseboer, and B Khoo. On the boundary integral method for the rebounding bubble. *Journal of Fluid Mechanics*, 570:407–429, 2007.

T Leslie and J Kennedy. High intensity focused ultrasound in the treatment of abdominal and gynaecological diseases. *International Journal of Hyperthermia*, 23(2):173–182, 2007.

Z Li, L Sun, Z Zong, and J Dong. A boundary element method for the simulation of non-spherical bubbles and their interactions near a free surface. *Acta Mechanica Sinica*, 28(1):51–65, 2012a.

Z Li, L Sun, Z Zong, and J Dong. Some dynamical characteristics of a non-spherical bubble in proximity to a free surface. *Acta Mechanica*, 223(11):2331–2355, 2012b.

S Lind. *A numerical study of the effect of viscoelasticity on cavitation and bubble dynamics*. PhD thesis, Cardiff University, 2010.

S Lind and T Phillips. The effect of viscoelasticity on a rising gas bubble. *Journal of non-Newtonian fluid mechanics*, 165(15-16):852–865, 2010a.

S Lind and T Phillips. Spherical bubble collapse in viscoelastic fluids. *Journal of non-Newtonian fluid mechanics*, 165(1-2):56–64, 2010b.

S Lind and T Phillips. The effect of viscoelasticity on the dynamics of gas bubbles near free surfaces. *Physics of Fluids*, 25(2):022104, 2013.

O Lindau and W Lauterborn. Cinematographic observation of the collapse and rebound of a laser-produced cavitation bubble near a wall. *Journal of Fluid Mechanics*, 479:327–348, 2003.

J Liu, C Zhu, T Fu, Y Ma, and H Li. Numerical simulation of the interactions between three equal-interval parallel bubbles rising in non-Newtonian fluids. *Chemical engineering science*, 93:55–66, 2013.

Y Liu, Q Wang, S Wang, and A Zhang. The motion of a 3d toroidal bubble and its interaction with a free surface near an inclined boundary. *Physics of Fluids*, 28 (12):122101, 2016.

F Lugli and F Zerbetto. An introduction to bubble dynamics. *Physical Chemistry Chemical Physics*, 9(20):2447–2456, 2007.

M Mahmud. *Three dimensional modelling of interaction of a bubble and a particle*. PhD thesis, University of Birmingham, 2017.

K Manmi and Q Wang. Acoustic microbubble dynamics with viscous effects. *Ultrasonics sonochemistry*, 36:427–436, 2017.

J Naude and F Mendez. Periodic and chaotic acoustic oscillations of a bubble gas immersed in an upper convective maxwell fluid. *Journal of non-newtonian fluid mechanics*, 155(1-2):30–38, 2008.

C Ohl, M Arora, R Ikink, N De Jong, M Versluis, M Delius, and D Lohse. Sonoporation from jetting cavitation bubbles. *Biophysical journal*, 91(11):4285–4295, 2006a.

C D Ohl, M Arora, R Dijkink, V Janve, and D Lohse. Surface cleaning from laser-induced cavitation bubbles. *Applied physics letters*, 89(7):074102, 2006b.

S-W Ohl, E Klaseboer, B C Khoo, et al. Spark bubble interaction with a suspended particle. In *Journal of Physics: Conference Series*, volume 656, page 012033. IOP Publishing, 2015.

R Owens and T Phillips. *Computational rheology*, volume 14. Imperial college press London, 2002.

A Philipp and W Lauterborn. Cavitation erosion by single laser-produced bubbles. *Journal of Fluid Mechanics*, 361:75–116, 1998.

S B Pillapakkam, P Singh, D Blackmore, and N Aubry. Transient and steady state of a rising bubble in a viscoelastic fluid. *Journal of Fluid Mechanics*, 589:215–252, 2007.

Y A Pishchalnikov, O A Sapozhnikov, M R Bailey, J Williams Jr, R Cleveland, T Colonius, L Crum, A Evan, and J McAteer. Cavitation bubble cluster activity in the breakage of kidney stones by lithotripter shockwaves. *Journal of endourology*, 17(7):435–446, 2003.

Lord Rayleigh. Viii. on the pressure developed in a liquid during the collapse of a spherical cavity. *The London, Edinburgh, and Dublin Philosophical Magazine and Journal of Science*, 34(200):94–98, 1917.

G Reisman, Y Wang, and C Brennen. Observations of shock waves in cloud cavitation. *Journal of Fluid Mechanics*, 355:255–283, 1998.

W Roberts, T Hall, K Ives, J Wolf, J Fowlkes, and C Cain. Pulsed cavitational ultrasound: a noninvasive technology for controlled tissue ablation (histotripsy) in the rabbit kidney. *The Journal of urology*, 175(2):734–738, 2006.

A Shima, T Tsujino, H Nanjo, and N Miura. Cavitation damage in polymer aqueous solutions. *Jounal of Fluids Engineering*, 1985.

W Song, M Hong, B Lukyanchuk, and T Chong. Laser-induced cavitation bubbles for cleaning of solid surfaces. *Journal of applied physics*, 95(6):2952–2956, 2004a.

WD Song, MH Hong, B Lukyanchuk, and TC Chong. Laser-induced cavitation bubbles for cleaning of solid surfaces. *Journal of applied physics*, 95(6):2952–2956, 2004b.

B K Sreedhar, S K Albert, and A B Pandit. Cavitation damage: Theory and measurements–a review. *Wear*, 372:177–196, 2017.

O Supponen, P Kobel, D Obreschkow, and M Farhat. The inner world of a collapsing bubble. *Physics of Fluids*, 27(9):091113, 2015.

C D Taylor, D S Valkovska, and C D Bain. A simple and rapid method for the determination of the surface equations of state and adsorption isotherms for efficient surfactants. *Physical Chemistry Chemical Physics*, 5(21):4885–4891, 2003.

G ter Haar and C Coussios. High intensity focused ultrasound: physical principles and devices. *International journal of hyperthermia*, 23(2):89–104, 2007.

T Tsujino. Cavitation damage and noise spectra in a polymer solution. *Ultrasonics*, 25(2):67–72, 1987.

T Tsujino, A Shima, and H Nanjo. Effects of various polymer additives on cavitation damage. *Proceedings of the Institution of Mechanical Engineers, Part C: Journal of Mechanical Engineering Science*, 200(4):231–235, 1986.

S van der Meer, B Dollet, M Voormolen, C Chin, A Bouakaz, N de Jong, M Versluis, and D Lohse. Microbubble spectroscopy of ultrasound contrast agents. *The Journal of the Acoustical Society of America*, 121(1):648–656, 2007.

A Wagner, L Giraud, and C Scott. Simulation of a cusped bubble rising in a viscoelastic fluid with a new numerical method. *arXiv preprint cond-mat/9904029*, 1999.

C Wang, B Khoo, and K Yeo. Elastic mesh technique for 3d bim simulation with an application to underwater explosion bubble dynamics. *Computers & fluids*, 32 (9):1195–1212, 2003.

Q Wang. The evolution of a gas bubble near an inclined wall. *Theoretical and computational fluid dynamics*, 12(1):29–51, 1998.

Q Wang. Unstructured mel modelling of nonlinear unsteady ship waves. *Journal of Computational Physics*, 210(1):368–385, 2005.

Q Wang and K Manmi. Three dimensional microbubble dynamics near a wall subject to high intensity ultrasound. *Physics of Fluids*, 26(3):032104, 2014.

Q Wang, K Yeo, B Khoo, and K Lam. Vortex ring modelling of toroidal bubbles. *Theoretical and Computational Fluid Dynamics*, 19(5):303–317, 2005.

Q Wang, M Mahmud, J Cui, W Smith, and A Walmsley. Numerical investigation of bubble dynamics at a corner. *Physics of Fluids*, 32(5):053306, 2020.

Q X Wang. Oscillation of a bubble in a liquid confined in an elastic solid. *Physics of Fluids*, 29(7), 2017.

S A Wilkerson. *A boundary integral approach to three-dimensional underwater explosion bubble dynamics*. The Johns Hopkins University, 1990.

M Wu and M Gharib. Experimental studies on the shape and path of small air bubbles rising in clean water. *Physics of fluids*, 14(7):L49–L52, 2002.

A M Zhang, P Cui, and Y Wang. Experiments on bubble dynamics between a free surface and a rigid wall. *Experiments in fluids*, 54:1–18, 2013.

Y L Zhang, K S Yeo, B C Khoo, and C Wang. 3d jet impact and toroidal bubbles. *Journal of Computational Physics*, 166(2):336–360, 2001.

APPENDIX A

BUBBLE IN A MAXWELL FLUID

A.1 Bubble in a Maxwell fluid

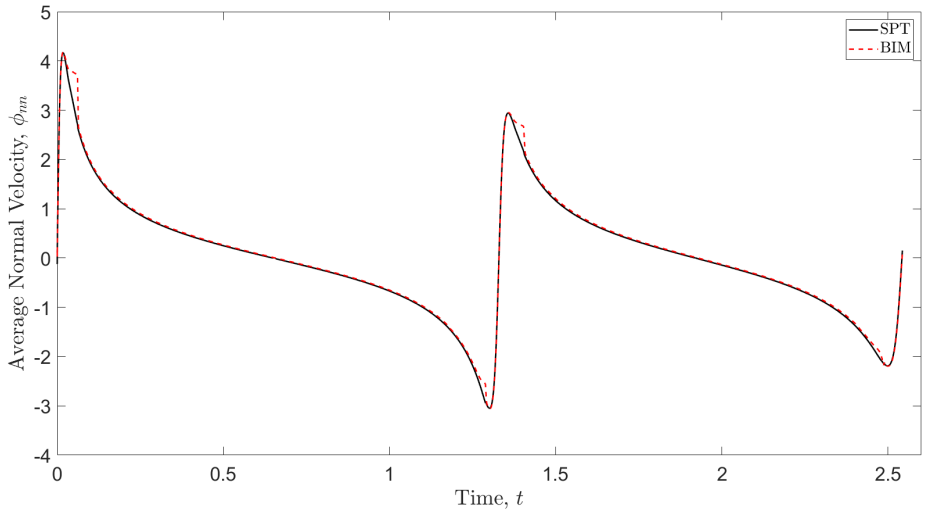


Figure A.1: The comparison of ϕ_{nn} for a spherical bubble in a Maxwell fluid with $De = 0.0$, between spherical bubble theory (2.2.17) and the BIM code with the remaining parameters being the same as in Figure 4.1.

To validate the calculation of ϕ_{nn}, we run the BIM code for a bubble in an infinite fluid using the same parameters as in section 4.1.1 and take an average value of ϕ_{nn} over the bubble surface to reduce the effect of errors. The results for $De = 0.0$, 0.2 and 20.0 are shown in Figures A.1, A.2, and A.3, respectively. In the Figures, the black solid line represents the potential history over the first two oscillations

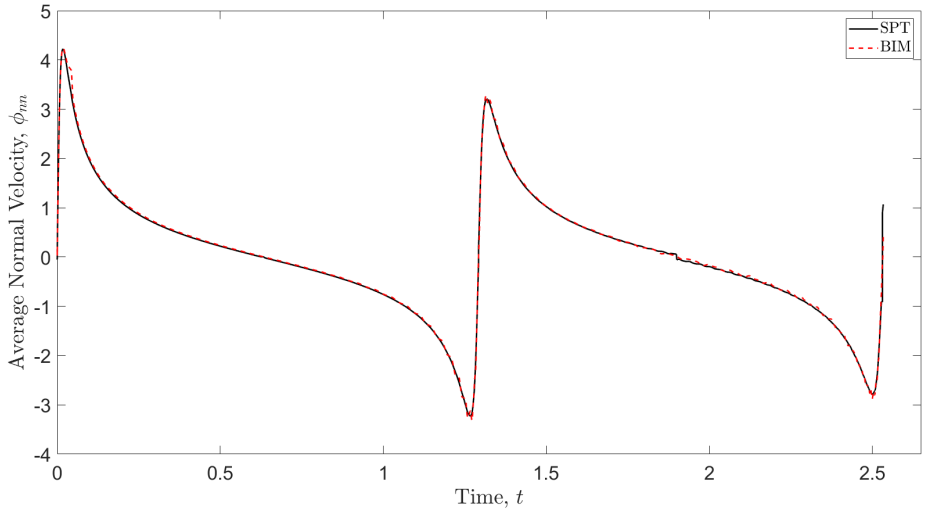


Figure A.2: The comparison of ϕ_{nn} for spherical bubble in a Maxwell fluid with $De = 0.2$, between a spherical bubble theory (2.2.17) and the BIM code with the remaining parameters being the same as in Figure 4.1.

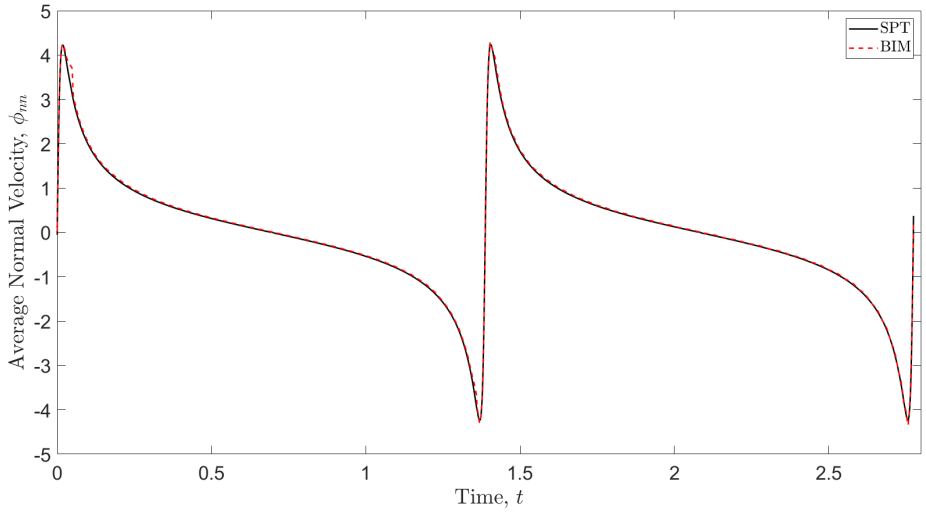


Figure A.3: The comparison of ϕ_{nn} for a spherical bubble in a Maxwell fluid with $De = 20.0$, between spherical bubble theory (2.2.17) and the BIM code with the remaining parameters being the same as in Figure 4.1.

as found analytically by equation (2.2.17), where the red dotted line represents the potential history as computed by the BIM code.

As shown, there is a strong agreement between the BIM code and the spherical bubble theoretical solution for ϕ_{nn} over the first two oscillations for all values of De. There is however, slight numerical error around the turning points for the lower

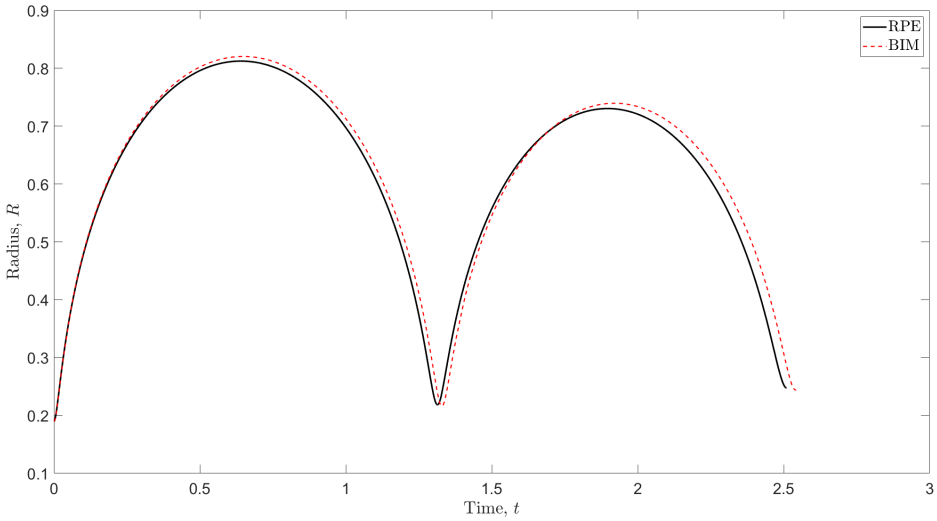


Figure A.4: The comparison of the radius history of a spherical bubble in a Maxwell fluid with $De = 0.0$, between the non-Newtonian Rayleigh-Plesset equation (2.3.6) and the BIM code with the remaining parameters being the same as in Figure 4.1.

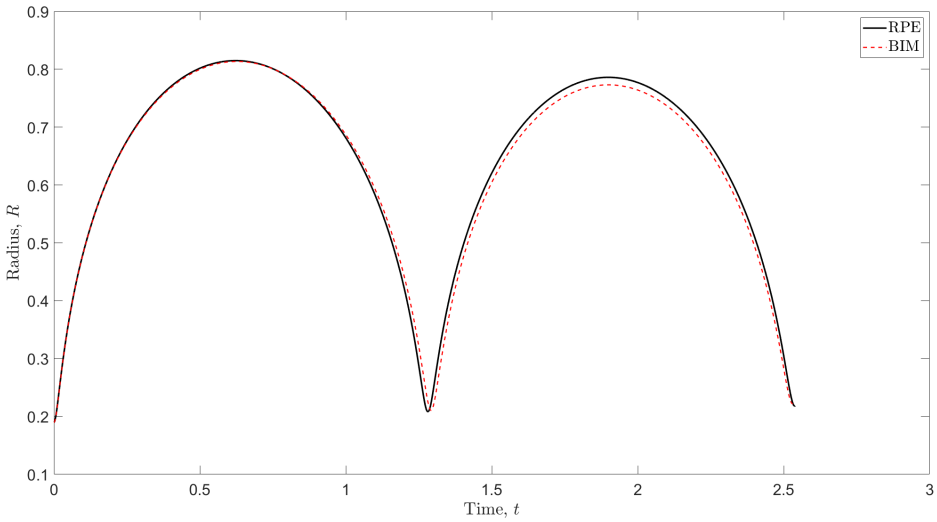


Figure A.5: The comparison of the radius history of a spherical bubble in a Maxwell fluid with $De = 0.2$, between the non-Newtonian Rayleigh-Plesset equation (2.3.6) and the BIM code with the remaining parameters being the same as in Figure 4.1.

values of De, but for only a very brief amount of time. Therefore, we can conclude that the viscous calculations made by the boundary integral method are adequate enough to accurately model the viscoelastic effects of a non-Newtonian fluid.

To validate the boundary integral method for the Maxwell model, we compare the radius history of the BIM code for a Maxwell fluid, to the radius history given

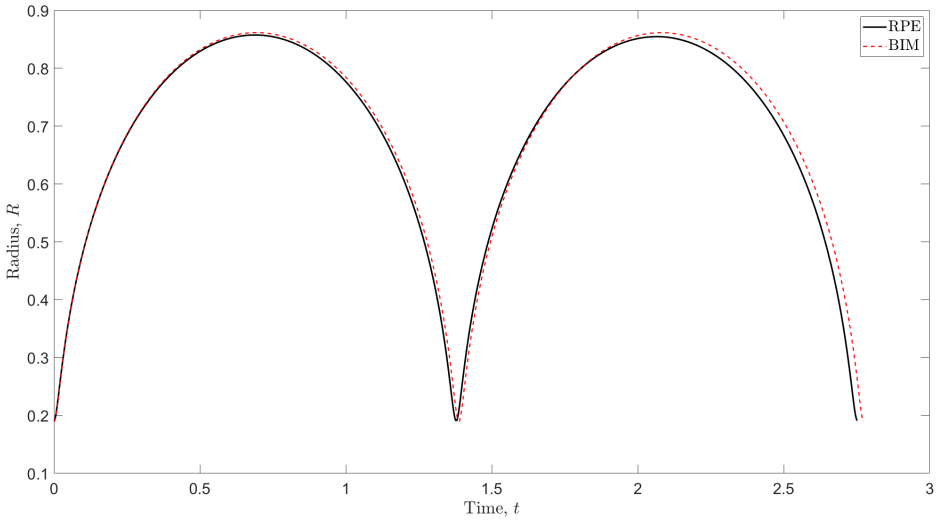


Figure A.6: The comparison of the radius history of a spherical bubble in a Maxwell fluid with $De = 20.0$, between the non-Newtonian Rayleigh-Plesset equation (2.3.6) and the BIM code with the remaining parameters being the same as in Figure 4.1.

by the non-Newtonian Rayleigh-Plesset equation (2.3.6). We initiate a bubble in an infinite fluid with an initial radius of $R_0^* = 4.5\mu m$.The parameters of the gas and liquid given by $\xi = 1.667$, $\sigma = 0.073 Nm^{-1}$, $P_0 = 101.3kPa$, $P_v = 0.023P_0$ and $\rho = 999 kgm^{-3}$. The pressure difference is set to $\varepsilon = 100$.

Figures A.4, A.5, and A.6 represent the radius history for a bubble in a fluid of Deborah numbers, $De = 0.0$, 0.2, and 20.0, respectively, as calculated both by the BIM three-dimensional code and the analytical solution to the Rayleigh-Plesset equation (2.3.6). In the simulation, the red dashed line represents the analytical solution for the bubble radius given by the dimensionless Maxwell Rayleigh-Plesset equation (2.3.6), and the black line represents the bubble radius as provided by the BIM code. As shown, both the analytical solution to the Rayleigh-Plesset equation and the numerical solution provided by the BIM code are in strong agreement with each other over the entirety of the first two oscillations for the Maxwell model.

APPENDIX B

BUBBLE IN A JEFFREY FLUID

B.1 Bubble in a infinite Jeffrey fluid

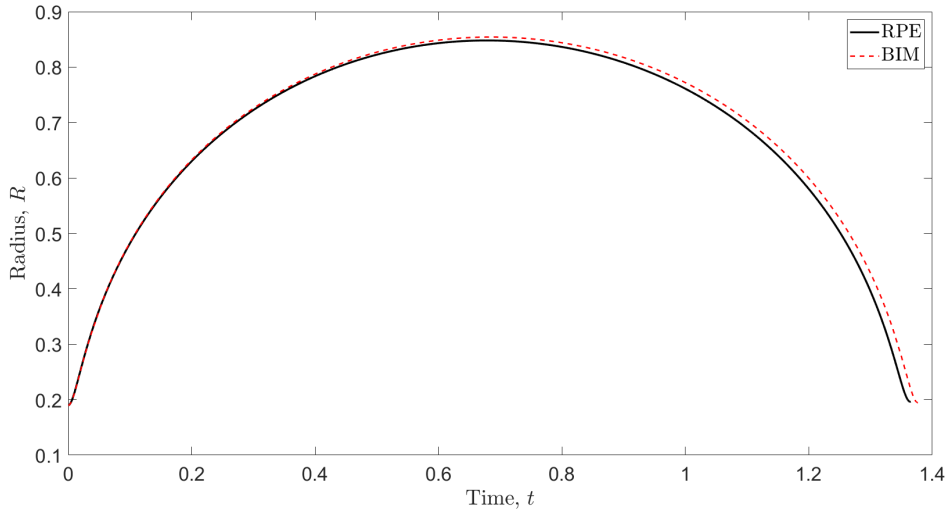


Figure B.1: The comparison of the radius history of a spherical bubble in a Jeffrey fluid with $\beta = 0.2$, between the non-Newtonian Rayleigh-Plesset equation (2.3.6) and the BIM code. The parameters of the surrounding liquid are the same as Figure 5.1.

To validate the boundary integral method for the Jeffrey model, we compare the radius history of the BIM code for a Jeffrey fluid, to the radius history given by the non-Newtonian Rayleigh-Plesset equation (2.3.6) with the normal stress tensor given by equation (2.5.23). We initiate a bubble in an infinite fluid with an initial radius of $R_0^* = 4.5\mu m$. The parameters of the gas and liquid are given by $\xi = 1.667$,

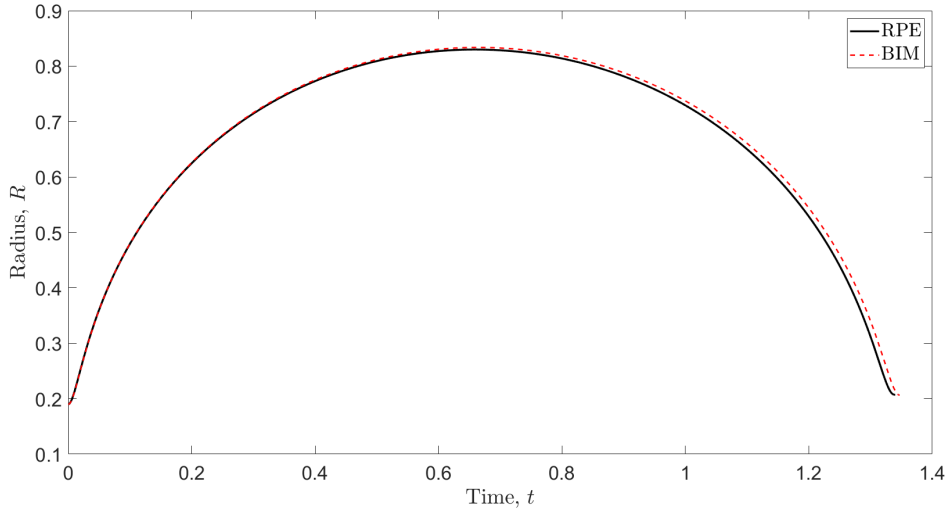


Figure B.2: The comparison of the radius history of a spherical bubble in a Jeffrey fluid with $\beta = 0.6$, between the non-Newtonian Rayleigh-Plesset equation (2.3.6) and the BIM code. The parameters of the surrounding liquid are the same as Figure 5.1.

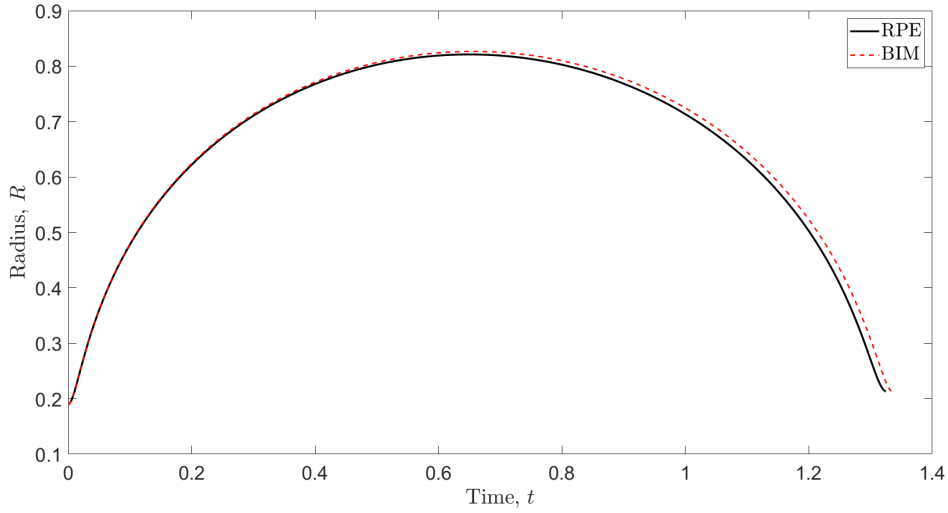


Figure B.3: The comparison of the radius history of a spherical bubble in a Jeffrey fluid with $\beta = 0.2$, between the non-Newtonian Rayleigh-Plesset equation (2.3.6) and the BIM code. The parameters of the surrounding liquid are the same as Figure 5.1.

$\sigma = 0.073 Nm^{-1}$, $P_0 = 101.3 kPa$, $P_v = 0.023 P_0$ and $\rho = 999 kgm^{-3}$. The pressure difference is set to $\varepsilon = 100$. The simulation is then repeated for a Jeffrey fluid with viscous ratios, $\beta = 0.2$, 0.4, 0.6 and 0.8. The results are found in Figures B.1, B.2, and B.3 for $\beta = 0.2$, 0.6, and 0.8 respectively.

Figures B.1, B.2, and B.3 represents the radius histories for a bubble in Jeffrey fluids of viscosity ratios, $\beta = 0.2$, $\beta = 0.6$, and $\beta = 0.8$, as calculated both by the BIM three-dimensional code (black lines) and the analytical solution the the Rayleigh-Plesset equation (2.3.6) (red lines). As shown, both the analytical solutions to the Rayleigh-Plesset equation and the numerical solutions provided by the BIM code are in strong agreement with each other over the entirety of the first oscillation for the Jeffrey model.

APPENDIX C

MATLAB CODE FOR NON-NEWTONIAN RAYLEIGH-PLESSET EQUATION

clear all

clear space;

clear plot;

clc;

$\gamma = 1.667$; % ratio of specific heats

$r_0 = 0.1898$; % initial dimensionless radius

$dr_0 = 4.5 * 10^{-6.0}$; % dimensional initial radius

$\rho = 999$; % density

$\sigma = 0.073$; % surface tension

$p_0 = 101300$; % ambient pressure

$p_v = 0.023 * p_0$; % vapour pressure of the bubble

$\mu = 0.001002$; % total viscosity

$\varepsilon = 100$;

$\beta = 0.8$; % viscosity ratio

$m\beta = 1.0 - \beta$;

$we = (dr_0 * (p_0 - p_v))/\sigma$; % webber number

$re = (dr_0 * sqrt((p_0 - p_v) * \rho))/\mu$; % reynolds number

$De = 2.0 * 10^{1};$ % Deborah number

$step = 4.0 * 10^{-4.0};$ %time-step

$totseconds = 1.326;$ %total run time

$totsteps = round(totseconds/step);$ %total steps

$T(1) = 0.0;$

$x(1) = 0.0;$

$R(1) = r_0;$

$jt_{nn}(1) = 0.0;$

for $n = 1$:totsteps

$a = \varepsilon * (r_0/R(n))^{3.0*\gamma};$

$nt_{nn} = (4 * \beta * x(n))/(re * R(n));$

$x(n+1) = x(n) + step * (a - 1.0 - 1.5 * x(n) * x(n) - 2.0/(we * R(n))$

$- nt_{nn} - jt_{nn}(n))/R(n);$

$R(n+1) = R(n) + step * x(n+1);$

$jt_{nn}(n+1) = (De * jt_{nn}(n))/(De + step) + (4.0 * step * x(n+1) * m\beta)/((De + step) *$

$re * R(n+1));$

$T(n+1) = T(n) + step;$

end

hold on; box on

$p_1 = \text{plot}(T(:),\ R(:),\ \text{'k'},\ \text{'lineWidth'},\ 2.0);$

xlabel('Time, t', 'Interpreter', 'latex', 'Fontsize', 25)

ylabel('Radius, R', 'Interpreter', 'latex', 'Fontsize', 25)